Polyethylene Glycol as an Electrolyte Additive for Rechargeable Hybrid Aqueous Batteries

by

Aly Mitha

A thesis
presented to the University of Waterloo
in fulfillment of the
thesis requirement for the degree of
Master of Applied Science
in
Chemical Engineering

Waterloo, Ontario, Canada, 2018

Author's Declaration

I hereby declare that I am the sole author of this thesis. This is a true copy of the thesis, including any required final revisions, as accepted by my examiners.

I understand that my thesis may be made electronically available to the public.

Abstract

Climatic and environmental challenges arising from excessive greenhouse gas production from human activities have necessitated a serious shift towards sustainable and renewable sources of power such as solar, wind and tidal. The bottleneck hindering the wide-scale adoption of these technologies is the intermittency of available power due to non-uniform climate and weather patterns over the course of the year. These variations prevent renewable energies from sustaining entire economies independently. Presently, secondary power generation must be run in parallel to sustain the base load while renewables are used to meet excess demand during peak load. Batteries are the strongest candidates for the improvement of these systems. They have been applied to enable load-levelling by storing excess power produced and supplying it to the grid during high demand periods.

Aqueous metal ion batteries are a strong contender for energy storage from renewable power sources due to their excellent safety, low cost, and environmental friendliness. In 2012, our research team developed the Rechargeable Hybrid Aqueous Battery (ReHAB) which featured a lithiated manganese oxide cathode and a zinc foil anode. While this battery generally performs well, it is compromised by parasitic processes at the anode which decrease its performance and operational lifespan. The main failure modes of this system are runaway dendrite formation from non-uniform electrodeposition and a high degree of corrosion caused by the acidic environment.

In this research, polyethylene glycol is integrated into the ReHAB system. The hypothesis is that PEG can be used to inhibit corrosion and dendritic growth. Low molecular weights (less than 500 $g \cdot mol^{-1}$) are used due to their greater solubility in the sulfate-based electrolyte. In the first project, 1 vol.% PEG200 is able to improve the discharge capacity of ReHAB cells compared to the control electrolyte after 300 cycles. This is accomplished via minimizing corrosion and dendrite growth at the anode. Furthermore, when dendrites are pre-grown on the anode prior to battery testing, the 1 vol.% PEG200 cells are able to consistently improve cycling life by more than five times.

In the second project a novel gel electrolyte is developed for the ReHAB system to improve cycling performance, reliability and reduce leakage of electrolyte during processing. Fumed silica is used as the thixotropic gelling agent and forms an interconnected network to support aqueous media in the electrolyte. PEG300 is used as the corrosion inhibitor and dendrite suppressant. The developed PEG-FS gel decreases corrosion by up to 40% and dendrite growth rate by 78%. In the absence of the PEG-FS gel electrolyte the zinc anode was severely consumed by corrosion reactions. Additionally, the PEG-FS-gel increases the capacity retention of ReHAB cells by approximately 40% after 1000 cycles in the large battery system.

The mechanism of interaction between PEG polymers and the zinc anode are also examined in depth using various electrochemical, spectroscopic and microscopic techniques. PEG adsorbs to the anode surface during charging and subsequently desorbs during discharge. PEG polymers were found to specifically adsorb to preferential nucleation sites on the zinc electrode, leading to several beneficial effects. Firstly, the surface diffusion of zinc ions is decreased, and they are forced to deposit on less favored sites on the electrode surface, leading to controlled electrodeposition. Secondly, the PEG polymers obstruct the adsorption of hydrogen ions during the charging process, thus decreasing corrosion and hydrogen evolution reactions. The adsorption-desorption mechanism allows the PEG to be recycled during battery operation and remain effective for very long periods.

Overall, highly compelling improvements are made to the ReHAB system with the addition of PEG to the aqueous electrolyte. By subduing corrosion and dendrite formation, the utilization of lithium is improved more than five-fold. This is a serious contribution as it allows for a much more efficient use of increasingly rare resources. The merits of PEG combined with its ease of integration into current aqueous battery systems highlights how they can be made into viable alternatives to lead-acid and organic lithium ion batteries for large scale energy storage applications.

Acknowledgements

I would like to express special gratitude to my supervisor, Prof. Pu Chen, for the wonderful opportunity to pursue my graduate studies and for his continuous guidance and support during this period. This research would not have been possible without his input.

Next, I would like to thank my colleagues Dr. Tuan K. A. Hoang, Dr. Alireza Zehtab Yazdi, Moin Ahmed, Dr. Jian Zhi for their time, words of advice, and assistance. Their friendship has made my graduate studies more fulfilling.

I would also like to acknowledge my reading committee members Prof. Jeff Gostick and Prof. Yuning Li for their time and constructive feedback towards the completion of this thesis.

Lastly, I would like to thank my parents, Nina and Salim, and my sister, Ruhee, for their unwavering love and support. They are my inspiration.

Table of Contents

Author's Declaration i

Abstract ii

Acknowledgements v

List of Figures viii

List of Tables xii

1.0 Introduction 1

1.1 The Rechargeable Hybrid Aqueous Battery (ReHAB) 5
1.2 Principles of Electrodeposition 7
1.3 Nucleation and Growth 13
1.4 Principles of Dendrite Formation 15
1.5 Controlling Electrodeposition using Organic Molecules 17

2.0 Electrochemical and Structural Characterization Techniques 24

2.1 Corrosion *24*

2.2 Chronoamperometry *25*

2.3 Electrochemical Impedance Spectroscopy (EIS) *27*

2.4 X-Ray Diffraction (XRD) *28*

2.5 Fourier Transform Infra-red Spectroscopy (FTIR) *31*

2.6 X-Ray Photoelectron Spectroscopy (XPS) *33*

2.7 Scanning Electron Microscopy (SEM) *34*

2.8 Transmission Electron Microscopy (TEM) *36*

3.0 Surface Adsorption of Polyethylene Glycol to Suppress Dendrite Formation on Zinc Anodes in Rechargeable Aqueous Batteries 39

3.1 Introduction 39

3.2 Results and Discussion 41

3.2.1 Electrochemical Characterization 41
3.2.2 Battery Performance 45
3.2.3 PEG Adsorption 52
3.2.4 Surface Composition, Morphology and Crystal Structure 56
3.2.5 Proposed Interaction Model 62

3.3 Section Conclusions 66

4.0 Polyethylene Glycol Additive in Thixotropic Gel Electrolyte for the ReHAB System 68

4.1 Introduction 68

4.2 Results and Discussion 70

4.2.1 Electrochemical Characterization 70
4.2.2 Battery Performance 75

4.3 Section Conclusions 79

5.0 Summary and Conclusions 81

6.0 Recommendations for Future Work 83

References 84

Appendices 98

List of Figures

Figure 1: Total annual anthropogenic GHG emission by gases 1970-2010 [8]..............................1

Figure 2: Solar and wind power generation in Germany in the months of June (left) and December (right) in 2012 [10]..2

Figure 3: Mechanism of the ReHAB system [24] 7

Figure 4: The correlation between free energy (ΔG) and the radius of a nucleus [66]..................14

Figure 5: Models of surface nuclei: (a) Cylindrical, (b) Hemispherical, (c) Conical, and (d) Pyramidal [70]..15

Figure 6: Model of Zinc dendrite formation [74]...17

Figure 7: SEM Images of zinc anode after charging to 1.5V in (a) Control electrolyte, and (b) 15 ppm $PbCl_2$, (c) 2 ppb of SDS, and (d) 0.01% Triton X-100 in the electrolyte, respectively [80]......19

Figure 8: XRD profiles of copper electrodeposits in varying concentrations of citric acid in the electrolyte [81]..20

Figure 9: SEM images of zinc electrodeposits in (A) Control, and (B) Tartaric acid additive electrolytes..21

Figure 10: Optical microscopy images of zinc electrodeposition on electrode surface in (a) 0 ppm, (b) 10 ppm, (c) 50 ppm, and (d) 100 ppm of PEI in the electrolyte [74]...............................22

Figure 11: SEM micrographs of zinc electrodeposited under galvanostatic conditions in (a) Control, and (b) 100 ppm PEI electrolytes [74]...23

Figure 12: Tafel fitting of a dynamic corrosion linear polarization plot [84]................................25

Figure 13: Different stages of chronoamperometry and their corresponding chronoamperograms [85]..26

Figure 14: Typical Nyquist plot. Inset: simple Randles equivalent circuit for fitting EIS spectrum for an electrochemical cell [86]*..28*

Figure 15: Schematic showing the interaction between x-rays and a typical crystalline sample [88] *..29*

Figure 16: Top: XRD spectrum of palladium metal. Bottom: corresponding database card [89]*...30*

Figure 17: Working principle of an FTIR interferometer [92] *..32*

Figure 18: (a) A sample XPS survey and (b) de-convoluted spectrum [93] *..................................33*

Figure 19: Components and principle of operation of an SEM [94]*..35*

Figure 20: Basic principle of a TEM [95]*...37*

Figure 21: Linear polarization experiments to measure corrosion of zinc foil in various electrolytes containing PEG additive..42

Figure 22: 1 h chronoamperograms of zinc foil in various PEG-based electrolytes at -135 mV overpotential vs. OCV. Inset: early chronoamperograms 44

Figure 23: Specific discharge capacities and coulombic efficiencies of small cells at 1 C rate made with different concentrations (left), and different molecular weights (right), of PEG additive in the electrolyte 46

Figure 24: Cycling performance of small cells at 4 C...47

Figure 25: Cycling performance of small cells at 4 C after pre-exposure to chronoamperometry for 3 hours at -135 mV overpotential vs. OCV 48

Figure 26:Cycling test of 7 mAh cells under 1 C current density 49

Figure 27: Rate capability of small cells containing different concentrations and molecular weights of PEG in the electrolyte...50

Figure 28: 24- and 72-hour float capacity loss of small cells with different concentrations and molecular weights of PEG in the electrolyte *51*

Figure 29: Self-discharge of small cells with different concentrations and molecular weights of PEG in the electrolyte *52*

Figure 30: Nyquist plots of EIS measurements conducted on 1 vol.% PEG200 and control symmetric zinc small cells before cycling (left) and after 50 charge-discharge cycles (right)..... *53*

Figure 31: FTIR of zinc electrodes after exposure to charge-discharge simulation using CV (left), and chronoamperometry at different overpotentials (right) 1 vol.% PEG200 electrolyte .. *55*

Figure 32: FTIR of zinc anodes after charge-discharge cycles: 1 cycle (left), and 50 cycles (right) *56*

Figure 33: Full XPS on zinc electrode after CA. Insets: high resolution Zn 2p (3/2) on zinc electrode after 1 h CA in control (left) and 1 vol.% PEG200 (right) electrolytes *57*

Figure 34: SEM of zinc electrodes after exposure to 1 h CA at -135 mV overpotential vs. OCV for: 0.17 s in (a) control electrolyte and (b) 1 vol.% PEG200 electrolyte, 9 s in (c) control electrolyte and (d) 1 vol.% PEG200 electrolyte, 30 s in (e) control electrolyte and (f) 1 vol.% PEG200 electrolyte, 100 s in (g) control electrolyte and (h) 1 vol.% PEG200 electrolyte, 500 s in (i) control electrolyte and (j) 1 vol.% PEG200 electrolyte, and 3600 s in (k) control electrolyte and (l) 1 vol.% PEG200 electrolyte *58*

Figure 35: Left: HRTEM micrograph of zinc dendrite grown in 1 vol.% PEG200 electrolyte for 1 h. Right: STEM EELS elemental mapping of (I) Zn (red) and (II) O (green) on a dendrite grown in control electrolyte, and of (III) Zn (red) and (IV) O (green) of a dendrite grown in 1 vol.% PEG200 electrolyte *60*

Figure 36: XRD (left) and GIXRD (right) of zinc electrodes after exposure to CA in 1 vol.% PEG200 and control electrolytes........61

Figure 37: Schematics of step-by-step zinc ion reduction on the surface of the anode in the control (upper), and 1 vol.% PEG200 (lower) electrolytes........63

Figure 38: Linear polarization of zinc electrodes in the different electrolytes........71

Figure 39: SEM micrographs and digital images of zinc anodes from large batteries post cycling in (a, c) Control, and (b, d) 4% FS + 1% PEG300 electrolytes........72

Figure 40: 1-hour chronoamperometry of zinc electrodes in the different electrolytes........73

Figure 41: SEM images of zinc electrodes after chronoamperometry in (a) Control, (b) 5% FS, (c) 4% FS + 1% PEG300, and (d) 3% FS + 2% PEG300 electrolytes........74

Figure 42: Cycling performance of ReHAB Swagelok cells containing different electrolytes........75

Figure 43: Cycling performance of ReHAB large battery system........76

Figure 44: Charge-discharge curves of ReHAB large batteries containing control (left) and 4% FS + 1% PEG300 (right) electrolytes........77

Figure 45: SEM micrographs of large battery anodes from (a) Control, and (b) 4% FS + 1% PEG300 electrolytes, and cathodes from (c) Control, and (d) 4% FS + 1% PEG300 electrolytes........78

List of Tables

Table 1: Summary of corrosion potentials and currents from linear polarization experiments…42

Table 2: Corrosion performance of zinc anodes in different electrolyte formulations 71

1.0 Introduction

Climate change is one of modern society's biggest challenges. Excessive carbon dioxide emissions from human activities have put the planet at risk of rising temperatures, warming oceans, shrinkage of ice sheets, retreating of glaciers and ice deposits, rising of average sea levels, and increasing occurrence of extreme weather events, among many others.[1–7] Among the chief sources of CO_2 emissions are the use of fossil fuels to power the global economy. Sourced from the Greenhouse Gas emission report, Figure 1 shows the total emissions for the period 1970-2010 in which CO_2 emissions from fossil fuel burning and industrial processes are responsible for 78% of the increase in emissions in the 40-year period.[8]

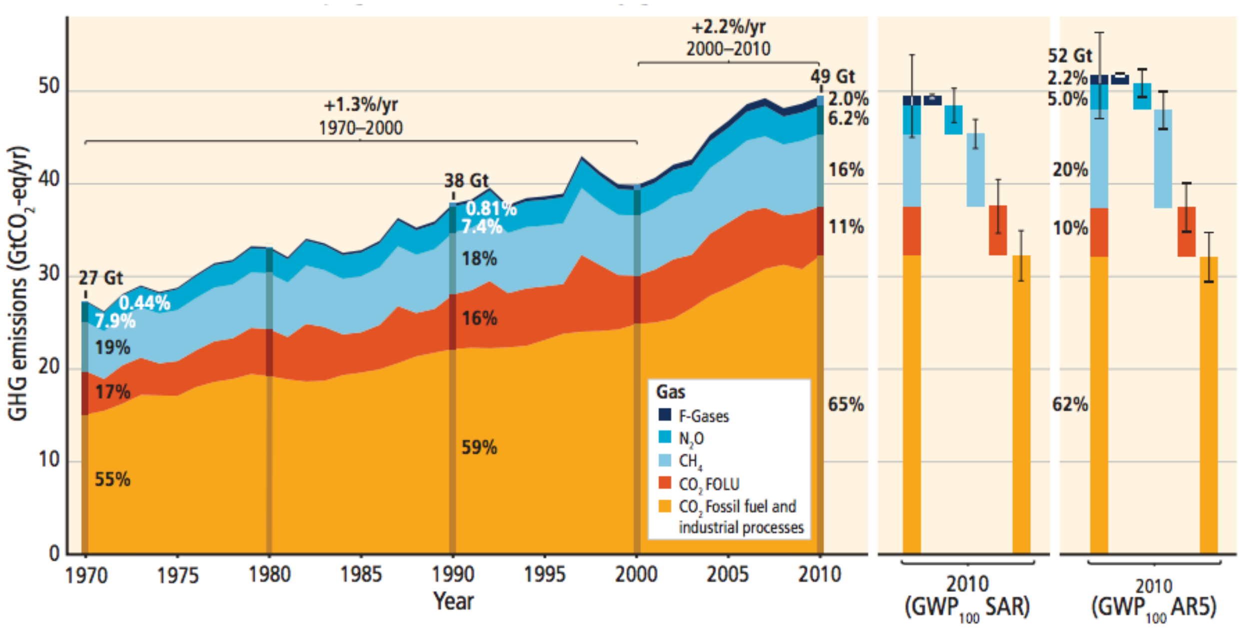

Figure 1: Total annual anthropogenic GHG emission by gases 1970-2010 [8]

Mitigating the consequences of climate change has necessitated shifting energy policies towards environmentally friendly, sustainable, and renewable sources such as solar, wind, tidal, and geothermal power.[9] However, the main obstacle preventing their wide-scale adoption is the intermittent nature of power generation. Depending on the local weather and climate patterns, seasons of the year and even times of the day, the amount of power generated can vary to quite a large degree. For example, Figure 2 shows the measured solar and wind power generation in Germany in 2012, and solar power may vary as much as 25 GW over the course of a day, while wind power significantly increases in output during the winter compared to the summer.[10] In an industrialized economy with a high demand for consistent power supply, these renewable power sources cannot be implemented on their own in their current state. Energy storage devices are one of the solutions being pursued to advance renewable energies. The main intention for their use is simple – to act as buffers in the power generation process. They are designed to store excess energy from the grid produced during low demand periods and supply this energy back into the grid during high demand periods. This is intended to normalize and improve the reliability with which power can be supplied.

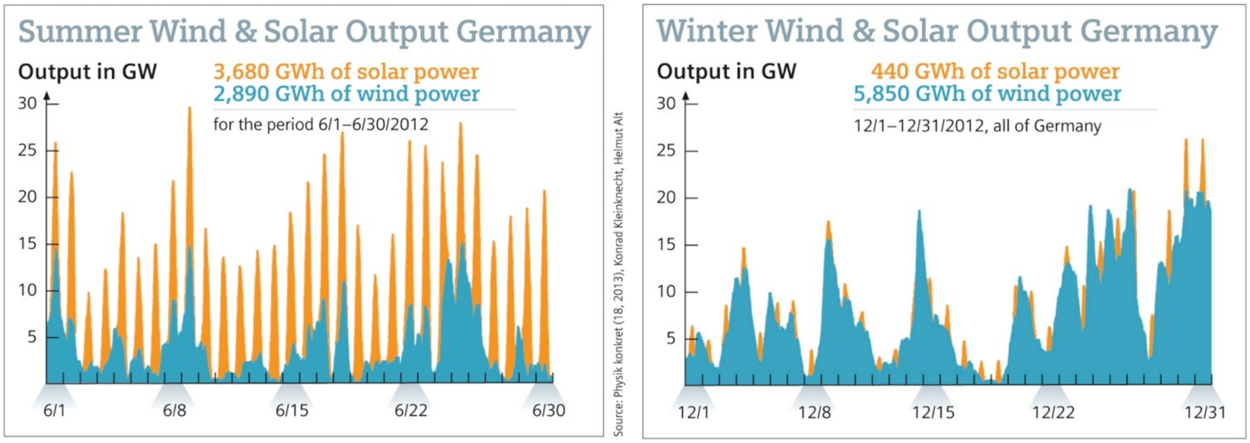

Source: Physik konkret (18, 2013), Konrad Kleinknecht, Helmut Alt

Figure 2: Solar and wind power generation in Germany in the months of June (left) and December (right) in 2012 [10]

The battery, a collection of electrochemical cells, is one of the most popular energy storage devices. Invented by Volta in the year 1800, batteries are devices that store electrical energy through reversible chemical reactions.[11] Typically, a battery will consist of a cathode, an anode, electrolyte solution, and an electrically insulating separator. The cathode and anode represent the positive and negative electrodes, respectively, and are the media on which chemical reactions take place to store energy. Traditionally, transition metals were used as electrodes, but modern batteries can feature more complicated materials such as metal oxides, semiconductors, and even alkali metals.[12–14] The electrolyte is a solution which allows ions to flow between the electrodes. The battery uses a difference in the electrochemical potentials of the two electrodes to force electrons to move (current flow) through an external circuit. Batteries fall into two general categories: primary batteries can release energy as soon as they are assembled but may only be used once (i.e. cannot be recharged), while secondary batteries can be charged and discharged (i.e. cycled). It is the second group that have drawn strong research interest for over two centuries. In the present day, batteries can be found in all manner of devices ranging from home appliances to spacecraft.[15]

The current industry standard is the organic lithium ion battery (LIB). Lithiated compounds are used to make the cathode and fall into three general categories: layered $LiMO_2$ (M = Mn, Co, or Ni), spinel $LiMn_2O_4$, and olivine $LiFePO_4$.[16] The selection between these materials is dependent on desired properties such as storage capacity, structural and chemical stability. The anode is a porous 3D structure (typically graphite) that can be used to store lithium, while organic electrolytes such as $LiPF_6$ are used. Modern organic LIBs can operate at potentials up to 4 V which allows them to have very high energy and power densities. Additionally, LIBs have a long shelf life, low self-discharge, no memory effect, and the ability to be cycled at high currents. The overall redox reaction that takes place in the organic LIB is shown in Equation 1:

$$LiCoO_{2_{(s)}} + 6C_{(s)} \leftrightarrow Li_{1-x}CoO_{2_{(s)}} + xLiC_{6_{(s)}} \quad \mathbf{(1)}$$

Rechargeable aqueous metal ion batteries have recently gained a lot of research interest because of several benefits they offer over organic batteries. Firstly, aqueous electrolytes are typically much less toxic than organic ones which enable batteries to be much safer during the manufacturing process and in consumer use.[17] Secondly, since the main component of aqueous electrolytes is water, the risk of fire is greatly reduced, especially when compared to organic lithium ion batteries which have been commonly noted to ignite and burn.[18,19] Thirdly, aqueous electrolytes are more facile and cost-effective to synthesize since their chemical reagents are readily available, and this significantly lowers the overall cost of production and storage. Lastly, aqueous electrolytes can facilitate ionic mobilities more than a hundred times higher than organic electrolytes.[17] This facilitates quicker cycling time and increases power density of the battery. The main limitation of aqueous electrolytes is a narrow electrochemical window in which they can operate due to the breakdown of water in the electrolyte.[20] This decreased upper voltage limit restricts the amount of power density an aqueous cell can have compared to organic cells.

For example, the Daniell cell is one of the first invented battery systems based on aqueous electrolytes. It uses copper and zinc half cells separated by a salt-bridge. Each of the half cells contains sulfate salts of its respective electrode, and during cycling copper and zinc ions are oxidized and reduced.[21] Equation 2 summarizes the overall reaction of a Daniell cell:

$$Cu^{2+}_{(aq)} + Zn_{(s)} \leftrightarrow Cu_{(s)} + Zn^{2+}_{(aq)} \quad \mathbf{(2)}$$

Zinc is a popular metal to use as an anode since it can achieve a discharge capacity of up to 820 $mAh \cdot g^{-1}$, can be used in combination with a large variety of cathode materials, and has a high electrochemical potential of -0.763 V vs. SHE – a necessity for high energy and power densities.[22,23] Furthermore, zinc has a high overvoltage for hydrogen evolution (less susceptible to excessive hydrogen production).[24] Similar to the Daniell cell (Zn||Cu), there are a few other examples of battery systems which use Zinc anodes: nickel zinc batteries (Zn||NiOOH), zinc ion batteries (Zn||MnO_2 or V_2O_5), and zinc air batteries (Zn||O_2).[18,23,25]

The nickel-zinc battery was first proposed in 1901 in a patent by Michaelowski.[26] It was developed as an alternative to the nickel-cadmium battery was roughly based on the silver-zinc battery that was already available.[27] It later received significant interest in the 1970s as a possible candidate for electric vehicle batteries.[28–30] The main benefits of this battery system are a high specific energy of 55-75 Wh·kg^{-1} (higher than lead-acid and nickel-iron batteries), excellent low temperature performance, long cycling life, and a light and compact battery design.[31–33] The battery is made of a nickel hydroxide cathode, a zinc oxide anode and saturated potassium hydroxide solution as the electrolyte. The overall cell reaction is expressed in Equation 3:

$$2Ni(OH)_{2_{(s)}} + ZnO_{(s)} \leftrightarrow 2NiOOH_{(s)} + Zn_{(s)} + H_2O_{(l)} \quad \mathbf{(3)}$$

Zinc-air batteries are used quite commonly in modern applications and can be found in small devices such hearing aids and navigation lights.[34] While they have a theoretical energy density of 1370 Wh·kg^{-1}, approximately only 200 Wh·kg^{-1} is practically available in secondary batteries due to poor cycling.[35] Zinc-air batteries offer far better safety, environmental friendliness, and cost of manufacturing compared to flow redox cells, LIBs, and other metal-air batteries.[36,37] They use a catalyst as the cathode to promote the reversible conversion of O_2 to O^{2-} while the anode is made of a blend of zinc and zinc oxide powders, organic binder, and other additives.[34,38,39] The cathode produces hydroxyl ions which react with the porous zinc anode to form zincate ($Zn(OH)_4^{2-}$). The main research focus on zinc-air batteries is in improving cycling performance by reducing corrosion, passivation, dendrite formation, and improving electrical conductivity, and the performance of the air electrode.[30,34,40–43] The overall reaction of a zinc-air battery is shown in Equation 4:

$$2Zn_{(s)} + O_{2_{(g)}} \leftrightarrow 2ZnO_{(s)} \quad \mathbf{(4)}$$

1.1 The Rechargeable Hybrid Aqueous Battery (ReHAB)

In 2012, our research group discovered the ReHAB system which combines an intercalating metal oxide ($LiMn_2O_4$) cathode and a first order zinc foil anode.[24] This system was completed by a mildly acidic electrolyte containing Li^+ and Zn^{2+} ions in the form of LiCl and $ZnCl_2$, respectively, however, we have since transitioned to sulfate salts of the same metals (Li_2SO_4 and $ZnSO_4$). There are several constraints on the concentration and pH of the electrolyte: firstly, the pH must be high enough (> 3) to prevent electrode reactions with H^+ ions but low enough (< 6.8) to prevent hydrolysis of the zinc ions in the electrolyte. Secondly, a sufficiently high amount of zinc be dissolved in the electrolyte to ensure good ionic conductivity. The electrolyte pH should be kept low enough (< 5.5) to dissolve the required amount of zinc. In view of these conditions, a pH of 4 was chosen for the ReHAB system.

ReHAB was created to overcome poor cycling performance of zinc-ion batteries (Zn||MnO_2) which feature only one type of active ions (Zn^{2+}) shuttling between the electrodes. The battery has a mid-point voltage of 1.8 V, and is capable of an energy density of 50-80 $Wh\cdot kg^{-1}$.[24] In the interim period since the invention of the ReHAB system several studies have been conducted addressing various aspects of the battery.[44–46]

Figure 3 shows the mode of operation of the ReHAB system. During the charging cycle Li atoms in the cathode are oxidized to Li^+ ions, and deintercalate from the cathode into the electrolyte. At the same time, Zn^{2+} ions from the electrolyte and reduced and deposit on the anode. During discharge the reverse reactions occur. The respective cathodic, anodic and overall reactions are presented in Equations 5-7:

$$\boldsymbol{Cathode}\text{:}\;\; LiMn_2O_{4(s)} \leftrightarrow Li_{1-x}Mn_2O_{4(s)} + xLi^+_{(aq)} + xe^- \quad \textbf{(5)}$$

$$\boldsymbol{Anode}\text{:}\;\; Zn^{2+}_{(aq)} + 2e^- \leftrightarrow Zn_{(s)} \quad \textbf{(6)}$$

$$\boldsymbol{Overall}\text{:}\;\; 2LiMn_2O_{4(s)} + Zn^{2+}_{(aq)} \leftrightarrow 2Li_{1-x}Mn_2O_{4(s)} + 2xLi^+_{(aq)} + Zn_{(s)} \quad \textbf{(7)}$$

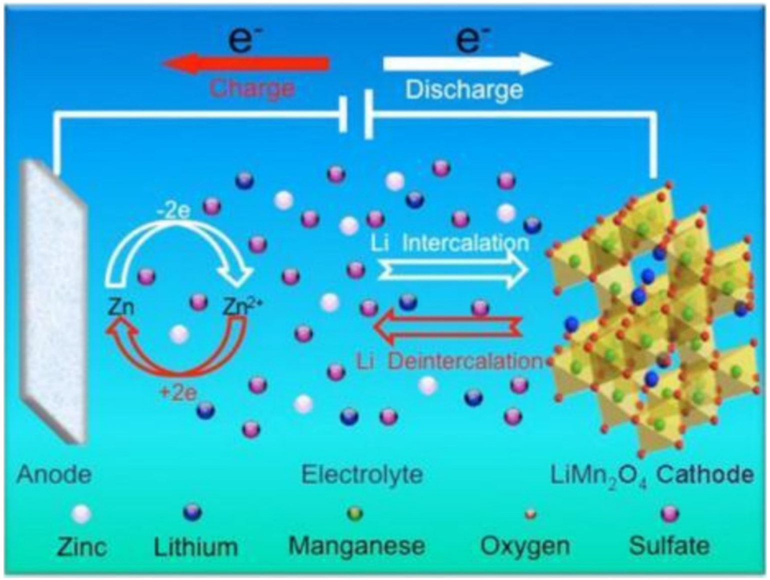

Figure 3: Mechanism of the ReHAB system [24]

Zinc anodes suffer from undesired parasitic reactions such as corrosion and dendrite growth which cause capacity fading and degraded performance.[47–49] Corrosion is a process whereby the metallic anode undergoes an irreversible chemical reaction and becomes converted to a non-useful form. In this particular case, corrosion forms a passivation oxide layer on anode surface. This process is disadvantageous because electrochemically active area is consumed and battery capacity is lost.[48] Dendrites are formed on the electrode when ions do not deposit evenly across the surface during the reduction process. The factors affecting electrodeposition and dendrite formation are discussed in the following sections.

1.2 Principles of Electrodeposition

Every ion has an equilibrium potential whereby its oxidation and reduction reactions are balanced kinetically. By applying a more negative potential than the equilibrium potential, a cation is forced to accept electrons and decrease its oxidation number, a process known as reduction. Electrodeposition is a process in which a metal is reduced from ionic state in an electrolyte to solid state on top of an electrically conductive surface (i.e. a metal) by applying a potential difference.

In the early 1800s, the electrodeposition process was driven by the potential difference between the anode and cathode electrodes placed in an electrolytic bath. For example, a protective coating of zinc is obtained by placing another metal in an electrolyte containing zinc salt and connecting it to the zinc anode. The differences in electrochemical potentials between the new metal and zinc create a driving force for the plating reaction.[50] In modern electrochemistry however, an external potential source is applied to further increase the rate of plating such that even micron thicknesses of coatings can be achieved in reasonable time frames. The electrodeposition process is extremely reliable since the amount of coating formed can be accurately measured and controlled by the supplied charge. Furthermore, it is a viable alternative to other coating methods because of its low cost, ability to perform well at low temperature and pressure, ability to coat large areas, and its ability to prepare a wide variety of structures on the surface whether in the nano- or micro-scale.[51]

The quality and properties of the coating depend on various parameters of the reaction. Organic additives may be used to either improve the performance of the plating reaction (anodic depolarization, current efficiency, and throwing power) or the quality and aesthetics (grain size, brightness, and deposit stress) of the coating itself.[52] Scientists began experimenting with such additives as early as the 1900s where formaldehyde was used in the electrolyte to alter grain sizes of a zinc electrodeposit.[53] The various functional groups present on organic compounds interact either with free ions in the aqueous solution to affect their mobility or with the electrode surface itself to affect local overpotentials.

Electrodeposition is a process mainly driven by the difference in the standard electrode potentials of metallic half cells. For example, the reduction of zinc from aqueous to solid state is described by the following reaction:

$$Zn^{2+} + 2e^{-} \rightarrow Zn \quad (-0.763\ V\ vs. SHE) \quad (\mathbf{8})$$

For metal A to deposit on metal B, the reduction potential A must be more negative than reduction potential B. In this case, metal A would form the anode (where oxidation occurs) and metal B would form the cathode (where reduction occurs). If there is not enough difference in electrode potentials, or a reverse plating is desired, an external power source may be connected to the electrochemical cell to drive the reaction. For example, zinc can be plated on zinc by applying a potential more negative than -0.763 V between the electrodes.

This relatively simple process is affected by several factors such as pH, temperature, current density, time, concentration, agitation and hydrogen evolution.[54] They are discussed in detail below.

1.2.1 Effect of pH

The electrolyte pH will affect the rate of deposition of metals. While in simple experiments this will only influence the duration of the reaction, in alloying reactions pH can have a vast impact on the ratio of the alloy formed. For example, Wu et al. reported that during electrodeposition of a Re-Ir-Ni alloy, increasing the pH from 2.0 to 2.5 resulted in significant mass gain since Re content was maximal while Ni was minimized.[55]

The pH will also influence the evolution of hydrogen gas which inhibits the desired reaction from progressing. Furthermore, as hydrogen is evolved, the pH of the solution will not remain at a fixed value, and this will have implications of the type and quality of electrodeposit achieved.

1.2.2 Effect of Temperature

Temperature has a few main effects on the electrodeposition process. Firstly, it affects the grain size and quality of the electrodeposit. Higher temperatures relieve internal stress in the electrodeposit hence allowing for larger crystalline grains to grow.[56] The improved crystallinity has knock-on effects for conductivity and dendrite formation (due to differences in the size and number of grain boundaries and dislocations). Secondly, higher temperatures have been found to increase current efficiency of the hydrogen evolution reaction, resulting in more gas released from the electrolyte.[57] Thirdly, higher temperatures lower the surface tension of the electrolyte allowing hydrogen gas bubbles to exit the surface at a smaller size.[58] This frees up more room for plating reactions and results in a smoother surface. Lastly, elevated temperatures also decrease the viscosity of the electrolyte.[59] Lower viscosity decreases the concentration polarization and improves ionic diffusion at the electrode-electrolyte interface. It also allows hydrogen bubbles to be transported through channels formed inside the electrodeposit.[57]

1.2.3 Effect of Current Density

The flow of current at the electrode facilitates the charge transfer that permits ions to reduce from the solution. Current density must be controlled well to form good quality coatings. If the current is too low, impurities will be co-deposited along with the desired metal. However, if the current is too high, parasitic side reactions such as hydrogen evolution will take place leading to the formation of metal hydroxides in the deposit, and also decreasing its crystallinity.[54] In general, increasing current density at the electrode results in higher deposition yields. For example, increasing the current density from 2 $mA \cdot dm^{-2}$ to 12 $mA \cdot dm^{-2}$ resulted in a four-fold increase in the thickness of nickel deposit in a Ni-CNT composite.[60]

Distribution of current density is not uniform at the electrode surface due to defects in crystal structure, grain boundaries, and changes in the surface morphology. Areas on the electrode with higher current density will promote reduction, and eventually this will lead to further disparity of the surface.

1.2.4 Effect of Time

The thickness of an electrodeposited coating is proportional to the duration of applied current. The total amount of charge transferred, Q, is given by the following relationship:

$$Q = I \times t \quad \mathbf{(9)}$$

Where I and t represent current and time, respectively. Increasing time leads to more charge transfer at the electrode-electrolyte interface, resulting in more reduction of ions from solution. In their work with nanocrystalline permalloy foils, Fazli et al. found that increasing the coating duration from 3 hours to 8 hours to 24 hours to 48 hours increased the coating thickness from 100 μm to 261 μm to 410.4 μm to 864.4 μm, respectively.[61] In a separate study, increasing deposition time from 10 minutes to 30 minutes increased coating thickness of deposited nickel on low carbon steel from 4.68 μm to 9.36 μm, and an increase in the deposition weight from 0.04 g to 0.08 g.[62]

1.2.5 Effect of Salt Concentration in the Electrolyte

The electrolytic bath supplies the ions necessary for the electrodeposition process, and a higher concentration of salt would mean more ions are available to reduce. However, the rate of deposition is only affected by the current density and the duration of the experiment. Increasing the concentration of the electrolyte will only be beneficial for longer plating durations or larger plating areas so that there is enough supply of ions available for reaction. Oloruntoba et al. found that during the deposition of nickel, increasing the concentration of the bath from 0.27 $g \cdot cm^{-3}$ to 0.35 $g \cdot cm^{-3}$ had no effect on the mass of the electrodeposit, indicating no correlation between the electrodeposition process and concentration.[62]

1.2.6 Effect of Agitation

Agitation increases the mass transport of ions in the electrolyte solution and replenishes ions at the electrode-electrolyte interface during reaction. This results in the decrease in thickness of the diffusion layer around the electrode, allowing for a higher rate of electroplating. For example, in a neutral phosphate bath, increasing the agitation by using a paddle decreased the thickness of the diffusion layer from 0.0294 cm to 0.0128 cm. Moving to an air-agitated system further reduced the thickness to 0.0066 cm.[63] During copper electroplating in a forced-flow cell, Engelmaier et al. noticed a vast reduction in the resistance of the plated-through hole as the agitation rate of the solution was increased. The decrease was observed until the mass-transport limit of the system was surpassed, after which the resistance maintained a constant value with increased agitation.[64] Since the resistance they measured is inversely proportional to the thickness of the metal deposit, a lower resistance would indicate a more substantial coating.

A secondary effect is that physical motion of the liquid around the interface dislodges gas bubbles that are formed from the hydrogen evolution reaction. By nature, since the gas bubbles are hydrophobic, they prevent electrolyte from reaching the surface and thus prevent electrodeposition in those locations. This leads to pitting of the deposit.[54]

1.2.7 Hydrogen Evolution

Coevolution of hydrogen gas in theory should occur at any potential below 0 V (since this is the hydrogen reduction potential). Theoretically this would render electroplating of any metal with a negative reduction potential null since hydrogen evolution would be the primary reaction. However, the reduction of hydrogen is extremely dependent on the type of metal electrode and the amount of current at the metal-electrolyte interface. On the surface of most metals the hydrogen evolution reaction will require an overvoltage to proceed, for example -0.2 V on the surface of polished platinum and -0.7 V on lead.[65] This principle allows even metals with significantly negative reduction potentials to be electrodeposited successfully.

During electroplating, the reduction of H^+ ions from solution to H_2 gas is an unwanted parasitic side-reaction. It will consume the supplied galvanic charge and reduce the rate of electroplating of the desired metal. Additionally, gas bubbles at the interface will inhibit reduction because of the inability of the electrolyte to be in contact with the surface at the locations of the bubbles. Lastly, evolution of hydrogen from the electrolyte will lead to an increase in pH. This will have other implications on the deposition process if left unmonitored.

1.3 Nucleation and Growth

Nucleation is a process during which a dust particle or seed crystal adheres to a surface to begin a crystallization process.[66] Nucleation occurs during phase transition – a process whereby a new phase starts to grow on an already existing phase of a material.[67] This process is governed by interfacial energy: this is the difference in free energy between the surface and the bulk, and occurs as a result of surface atoms having fewer bonds than their bulk counterparts.[68] This energy will resist the formation of a nucleus since the nucleus will increase the overall free energy of the system. Therefore, during initial stages, it is more energetically favorable for nuclei to dissolve back into solution rather than to continue to grow.[69] The Gibbs free energy of cohesion of a nucleus is proportional to its volume (bulk free energy), while that of dissociation is proportional to the surface area (surface energy). There exists a critical size at which the two free energies are equal. For a nucleus to survive it must be at this critical size, after which any increase in size will increase its stability on the surface.[66] This is illustrated further in Figure 4.

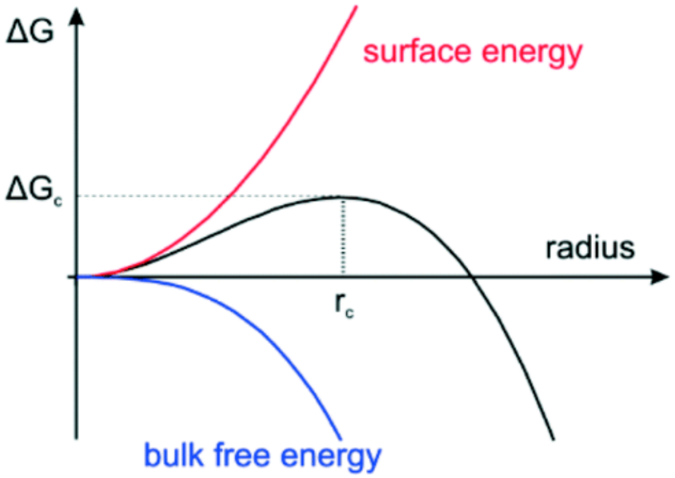

Figure 4: The correlation between free energy (ΔG) and the radius of a nucleus [66]

Heterogenous nucleation (where the nucleating species is different from the bulk species) further increases the complexity of the electrodeposition process. For nucleation to proceed, bonding between the nucleating species and the atoms at the surface of the substrate must be energetically more favorable than bonding between the surface atoms and the solvated species. This is dependent on the crystal structures of the nuclei and the bulk matter. A large mismatch between the two will result in a high amount of strain at the interface, and the bonding will be poor. On the other hand, well-matched crystal structures will promote much stronger bonding since interfacial energy will be minimized.

During the initial stages of growth, nuclei are separated widely enough such that they grow independent of each other. This growth may be laterally along the surface (2D growth) or in all directions (3D growth). The rate of growth of nuclei is proportional to number of electrons, rate constant, and molecular weight, while it is inversely proportional to the density of the deposit. Figure 5 shows the different types of nuclei that can form on a surface.

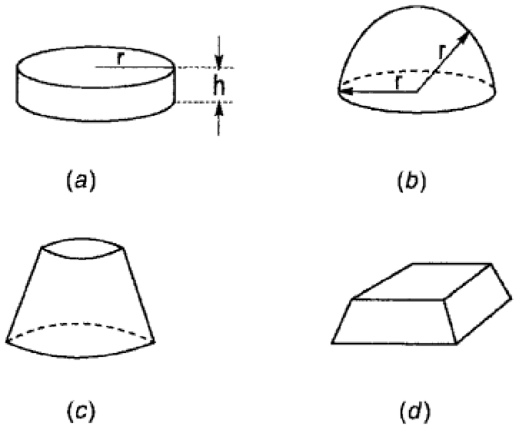

Figure 5: Models of surface nuclei: (a) Cylindrical, (b) Hemispherical, (c) Conical, and (d) Pyramidal [70]

As the growth of nuclei progresses, they will begin to come into contact with each other since both 2D and 3D growth models have a component of growth along the plane of the surface. The interaction between nuclei will lead to significant changes in the overpotential and concentration distribution around the nuclei. Growth of the nuclei in certain directions will be limited since they will overlap with other nuclei. Overlapping areas have lower concentrations and nucleation rates. Once two (or more) nuclei come in contact with each other, they will not be able to grow into each other, and thus growth in the overlapping region will halt. The ratio of 2D growth rate to 3D growth rate will determine the overall morphology of the formed surface: 2D growth will promote layered growth and result in flatter and smoother surfaces, while dominating 3D growth in the perpendicular direction will result in the formation of features, and a bumpy and rough surface.

1.4 Principles of Dendrite Formation

Dendrites refer to features which grow on the surface of a cathode under the charge-transfer-controlled regime while the rest of the electrode surface experiences electrodeposition under the diffusion-controlled regime.[71] Dendrites have highly-ordered and crystalline structures, and their growth directions are well-defined.[51] Dendrite formation begins with a non-uniform electrode surface (any relevant practical surface will have some degree of roughness). Some locations on the electrode surface are raised at the leading edges of screw dislocations and have a higher exposure to the electrolyte, thus resulting in them experiencing a higher amount of 3D diffusion of ions from solution compared to recessed areas.[72,73] The increased access to ions results in preferential growth at the tip of the elevated area than in the surroundings, eventually leading to the formation of high aspect-ratio features on the surface.

The growth of dendrites is governed by the overpotential applied at the tip. In a simplified model, the total overpotential of the tip has been shown to be equal to the activation overpotential.[74] This condition is met by assuming that the increased 3D diffusion afforded to the elevated position on the surface moves the system from being diffusion-controlled to being activation-controlled. The tip overpotential is thus defined as follows:

$$\eta_{tip} = \eta_a = -\frac{RT}{\alpha_c F}\ln\left(\frac{|i_{tip}|}{i_0}\right) \quad \mathbf{(10)}$$

Where α_c is the cathodic transfer coefficient, i_{tip} is the current at the tip and i_0 is the exchange current density.

The entire surface is exposed to the same potential, and the overpotential of the flat surface is equal to the overpotential at the tip.[75] The expanded expression is shown in Equation 11 and simplified in Equation 12:

$$-\frac{RT}{\alpha_c F}\ln\left(\frac{|i_{flat}|}{i_0}\right) + \eta_{c,flat} = -\frac{RT}{\alpha_c F}\ln\left(\frac{|i_{tip}|}{i_0}\right) \quad \mathbf{(11)}$$

$$\frac{i_{tip}}{i_{flat}} = exp\left[(-\eta_{c,flat})\frac{\alpha_c F}{RT}\right] \quad \mathbf{(12)}$$

Since the concentration overpotential of the flat surface is negative, the current at the tip will always be larger than the current on the rest of the flat surface.[74] A larger value of $\eta_{c,flat}$ will promote dendritic growth even more.

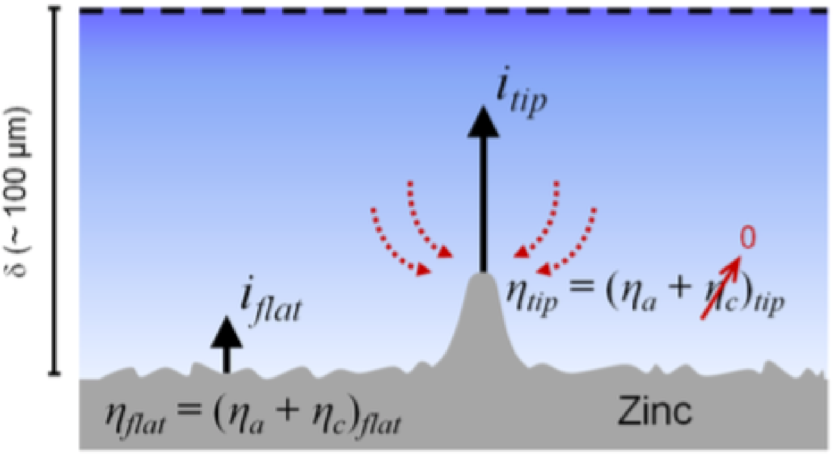

Figure 6: Model of Zinc dendrite formation [74]

Figure 6 illustrates the mechanism of dendrite formation of zinc during the electrodeposition process. Due to its protrusion into the electrolyte, the tip experiences a much higher 3D diffusion of ions (as indicated by the dotted red arrows) compared to the rest of the surface. Due to this, the current experienced at the tip is higher, and results in a higher rate of growth. Generally, more roughness on a surface creates more favorable conditions for dendritic growth than for layer growth.

1.5 Controlling Electrodeposition using Organic Molecules

There exists a myriad of ways to control the structure and morphology of the surface during electrodeposition. These range from optimizing the pulse of current supplied to the electrode (pulsed electrodeposition), zinc alloys with other metals to suppress hydrogen evolution, tuning the particle size of zinc to improve performance, and organic additives such as surfactants, acids and polymers to achieve better control of the electrodeposit.[76,77]

1.5.1 Surfactants

'Surfactant' is a moniker given to a family of organic molecules that are classified as Surface Active Agents. These molecules are generally composed of two main parts, one hydrophilic and the other hydrophobic. Since they can change the surface tension of liquids, their primary use is to allow two immiscible liquid phases to coexist together as an emulsion.[78] They are also used extensively in industry as foaming and wetting agents. Common examples of surfactants are sodium dodecyl sulphate (SDS) which is used in soaps and detergents, and Triton X-100 (Polyoxyethylene glycol octylphenol ether) which is a wetting agent used for coatings. In the context of electrodeposition, surfactants may be added to the electrolyte to improve the quality of the electrodeposit.

The first example is the use of sodium dodecyl benzene sulfonate (SDBS) on a zinc anode in a zinc-air battery.[79] In this case, the surfactant was added in quantities up to 2% to KOH electrolyte. The authors found that the discharge capacity of the batteries improved by as much as 36%. This was due to the SDBS surfactant modifying the type of passivation layer from dense and compact to loose and porous by forming small needle-like structures of the electrodeposit. This led to more efficient transport of the solution and the product through the passivation layer.

A second study investigated the effects of sodium dodecyl sulphate and Triton X-100 on dendrite formation in zinc-polyaniline batteries.[80] The study found that by using the surfactants, they could improve the cycling performance significantly, with the 80%-retention occurring at 38 cycles in SDS and 79 cycles in Triton X-100 compared to just 23 cycles in the control electrolyte.

Both surfactants increased the dispersion and polarization of the solution, leading to a smaller particle size of zinc deposit during the charging cycle. This is illustrated in the SEM micrographs in Figure 7 below.

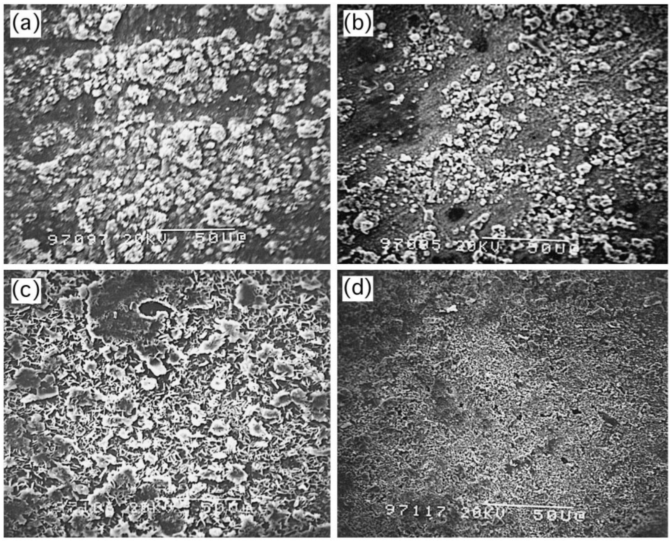

Figure 7: SEM Images of zinc anode after charging to 1.5V in (a) Control electrolyte, and (b) 15 ppm $PbCl_2$*, (c) 2 ppb of SDS, and (d) 0.01% Triton X-100 in the electrolyte, respectively* [80]

1.5.2 Organic Acids

Organic acids contain at least one hydrophilic -COOH group at a terminal. This promotes hydrogen bonding with water along the Helmholtz layer formed on the electrode surface in aqueous electrolytes. Bonding allows these adsorbed organic molecules to effectively block areas on the electrode surface from ion transport from the solution, and can thus inhibit growth in these regions. If a solid surface is completely covered with adsorbed organic molecules, it becomes fully passivated meaning that no electrodeposition will be allowed to occur.

Citric acid was investigated as a complex-former and inhibitor in the electrodeposition of nanocrystalline copper.[81] The control sample (copper deposition in the absence of inhibitor in the electrolyte) forms a crystalline structure with an average grain size of approximately 50 nm. In order to decrease the size of the crystalline grain, the authors found that they needed to increase the nucleation and decrease growth of the copper deposits. Citric acid was found to have multiple possible effects on the system. Firstly, it formed complexes with Cu^{2+} ions in solution hence decreasing their mobility and thus their 3D diffusion properties. Secondly, citric acid adsorbed to active sites on the surface and hinder growth at these locations. Cu^{2+} ions would then be forced to deposit in less favored locations leading to a more uniform surface profile. The crystallite size was also found to be proportional to the concentration of citric acid in the electrolyte, as shown in Figure 8. As the concentration of the inhibitor increases, the crystallite size (denoted by D_V) decreases.

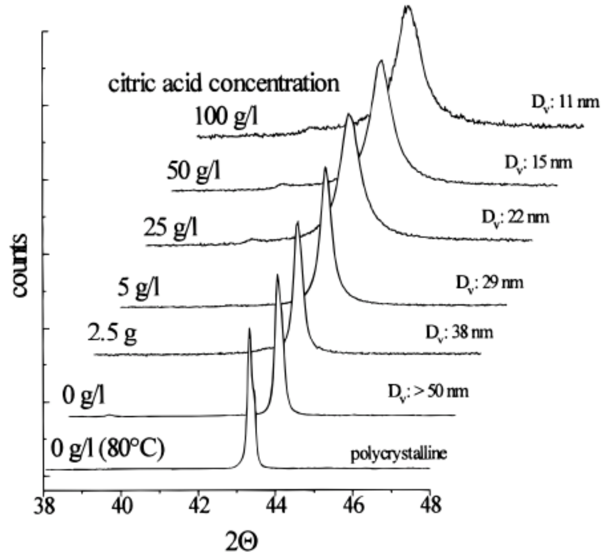

Figure 8: XRD profiles of copper electrodeposits in varying concentrations of citric acid in the electrolyte [81]

In a separate study, the effect of benzoic acid during the electrodeposition of zinc on iron was investigated.[82] By measuring the cyclic voltammetry of the system, the researchers were able to show that in the control sample (without any additive in the electrolyte) the deposition reaction on the electrode is diffusion-controlled. After the addition of benzoic acid, the reaction changed to being activation-controlled. This proved that benzoic acid acts as a surface barrier to the reduction of ions. This result was further confirmed by potentiodynamic polarization experiments which show the electrodeposited zinc surface becoming much smoother when even tiny amounts of benzoic acid are added to the electrolyte. The acid adsorbed to preferential sites on the electrode surface and forced Zn^{2+} ions from solution to reduce other locations.

Tartaric acid has also been studied for its effect in zinc electrodeposition from a sulfate electrolyte.[76] By conducting XRD on electrodeposited samples of zinc with and without tartaric acid the researchers were able to show that the additive significantly changed the crystalline structure of zinc. While the overall diffraction angle of the peaks did not change, their intensities were significantly different than the control sample. This shows that tartaric acid promotes the growth of certain crystalline planes such as (101), (110) and (112) while retarding the growth of the (002) and (103) planes. Overall, this resulted in smoother deposits with some refining of the grain size as shown in the SEM micrographs in Figure 9.

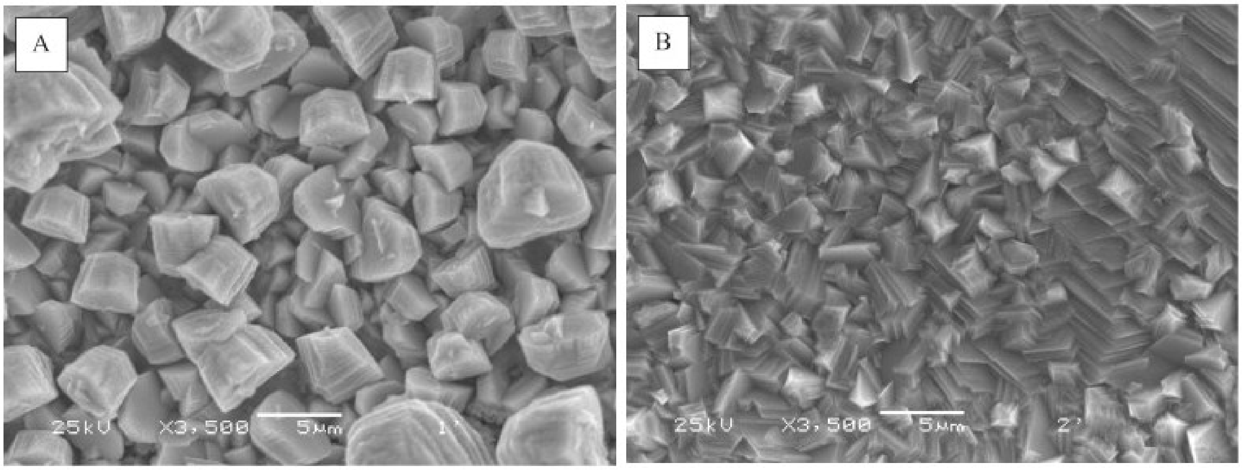

Figure 9: SEM images of zinc electrodeposits in (A) Control, and (B) Tartaric acid additive electrolytes

1.5.3 Polymeric Species

Polymers are arguably the most common form of organic molecules and can be found with a wide variety of functional groups. The functional groups are responsible for interactions between the polymers and other species they are exposed to. In electrochemistry, polymers act in a similar manner to that described previously for organic acids – they have affinity for the surface and/or form complexes with metal ions in solution thus changing their diffusion properties.

The first example is a study investigating zinc electrodeposition in KOH electrolyte containing polyethyleneimine (PEI) additive.[74] PEI was shown to reduce the activation overpotential of the electrode, thereby suppressing the roughness evolution of the electrodeposit. Figure 10 shows optical microscope images of the zinc electrodeposition. As the concentration of the additive is increased the electrode shows less and less dendrite growth such that at 100 ppm there is no evidence of dendrites. Figure 11 shows SEM micrographs of samples after electrodeposition, where the sample exposed to the PEI additive has a remarkably uniform surface at concentrations as low as 100 ppm while the control sample exhibits large dendritic features.

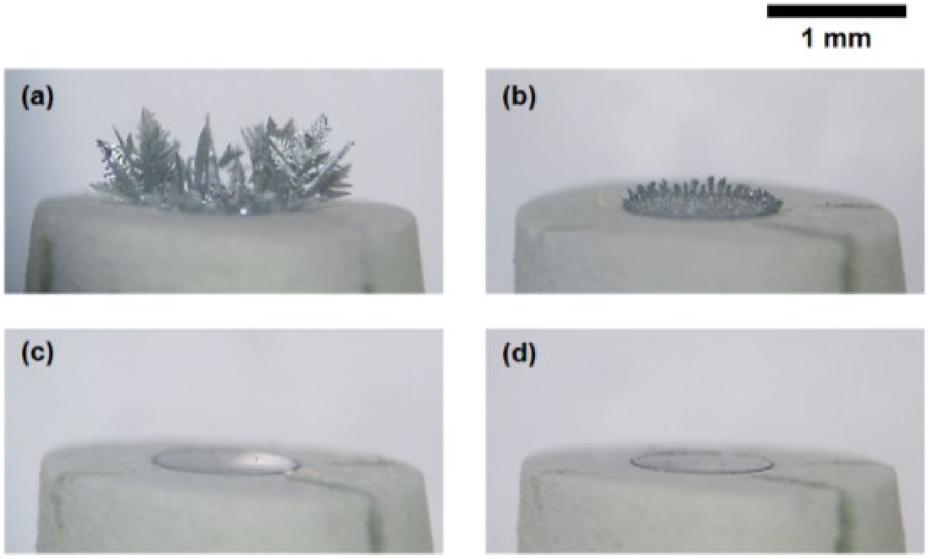

Figure 10: Optical microscopy images of zinc electrodeposition on electrode surface in (a) 0 ppm, (b) 10 ppm, (c) 50 ppm, and (d) 100 ppm of PEI in the electrolyte [74]

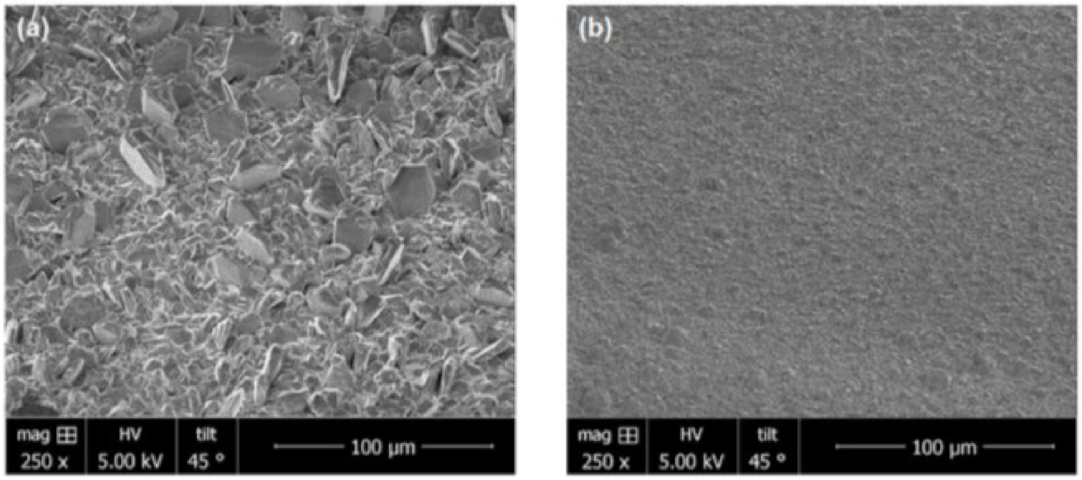

Figure 11: SEM micrographs of zinc electrodeposited under galvanostatic conditions in (a) Control, and (b) 100 ppm PEI electrolytes [74]

The role of polyethylene glycol (PEG) was also investigated in the co-deposition of zinc-chromium alloys from sulphate baths.[83] In the study, with no PEG in the electrolyte the deposition of zinc was preferred to chromium since it has a more positive reduction potential. However, as the molecular weight of PEG was increased, the polarization of the electrode was shifted in a more negative direction, hence allowing chromium ions to be co-deposited with zinc to form an alloy on the surface. This is because higher molecular weight PEG polymers have a longer chain length resulting in more active sites on the electrode surface being occupied by the additive. This makes it more difficult for zinc to reduce at its native equilibrium potential (hence the increase in polarization).

2.0 Electrochemical and Structural Characterization Techniques

This section will explain expand on the characterization techniques that will be used to explore various electrochemical and structural properties over the course of experimentation.

2.1 Corrosion

Corrosion is a chemical process whereby a pure metal is converted to a more stable version. The most common forms of corrosion involve an oxidation reaction whereby an oxidizing agent such as oxygen or sulfur forms a chemical bond with the metal. The process of corrosion is undesired in energy storage applications because it results in the passivation of an electrochemically active metallic surface. This results in reduced activity at the electrode-electrolyte interface and will lead to poorer capacity.

Dynamic corrosion can be quantified by means of three-electrode linear polarization experiments. The electrode of interest is used as the working electrode while a neutral metal is inserted as the counter electrode. A reference electrode of choice may be used as well. Potential is swept at a constant linear rate, and the response of the system is measured in the form of current. The potential is then plotted versus the logarithm of the current and a Tafel extrapolation is conducted, as shown in Figure 12. As part of the extrapolation, the linear portions of the graph are fitted with tangent lines, and the intersection point denotes the corrosion potential (E_{corr}) and corrosion current (i_{corr}). The corrosion current may be further divided by the exposed area of the electrode to normalize for area.

The tangent on the more negative potential values characterizes the cathodic reaction, which in this case is the evolution of hydrogen gas from hydrogen ions in solution. The other tangent represents the anodic reaction – the dissolution of a solid metal to its aqueous state.

$$Cathodic\ Reaction: 2H^{+}{}_{(aq)} + 2e^{-} \leftrightarrow H_{2\,(g)} \qquad \mathbf{(13)}$$

$$Anodic\ Reaction: M_{(s)} \leftrightarrow M^{n+}{}_{(aq)} + ne^- \quad \mathbf{(14)}$$

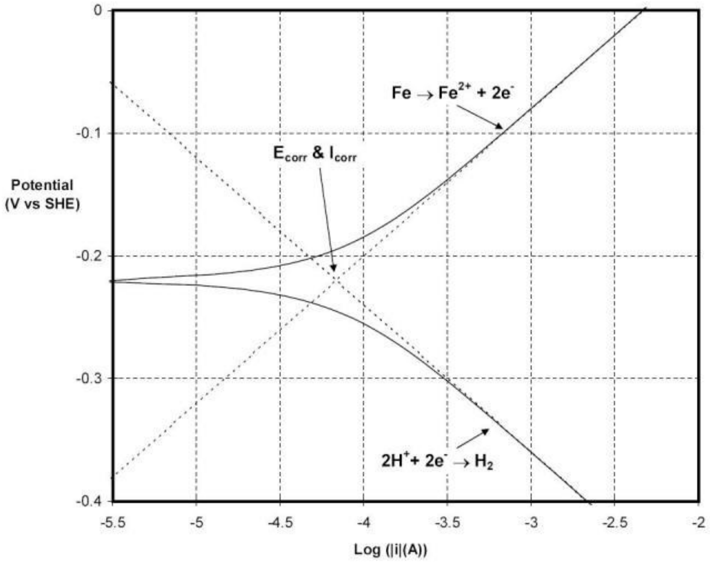

Figure 12: Tafel fitting of a dynamic corrosion linear polarization plot [84]

In this study corrosion was conducted on a CHI 760D potentiostat using zinc foil as both the working and counter electrodes. The scan rate was set to 1 mV·s^{-1} for project 1, but this was later changed to 0.01 mV·s^{-1} for project 2 for higher sensitivity.

2.2 Chronoamperometry

Chronoamperometry is a study of the kinetic response of an electrochemical system to an applied potential. The imposed potential biases one of the redox reactions of an equilibrated system and entails a flow of electrons. This can be measured as a current and be used to calculate the rate of reaction. Over the course of this research, chronoamperometry is used to assess the amount of dendritic growth in different electrolytes. Specifically, it can shed light on the nucleation and growth processes that are entailed in the reduction of metallic ions from aqueous solution. While there are several other techniques that can examine the composition, crystal structure, and morphology of dendrite growth, chronoamperometry remains the only tool to numerically quantify this process. It will be used to evaluate the efficacy of different electrolytes in suppressing dendrite growth.

Figure 13 describes these processes during reduction.[85] At the initial stage, the system is at equilibrium and the oxidation and reduction reactions at the electrode are equal and thus there is no net transfer of electrons. As a potential is applied in Stage II, the electroreduction reaction begins. This represents the nucleation step. Once the nuclei are formed, the growth phase commences represented by Stage III. An understanding of the types and magnitudes of nucleation and growth reactions can be gained by analyzing chronoamperograms from different systems.

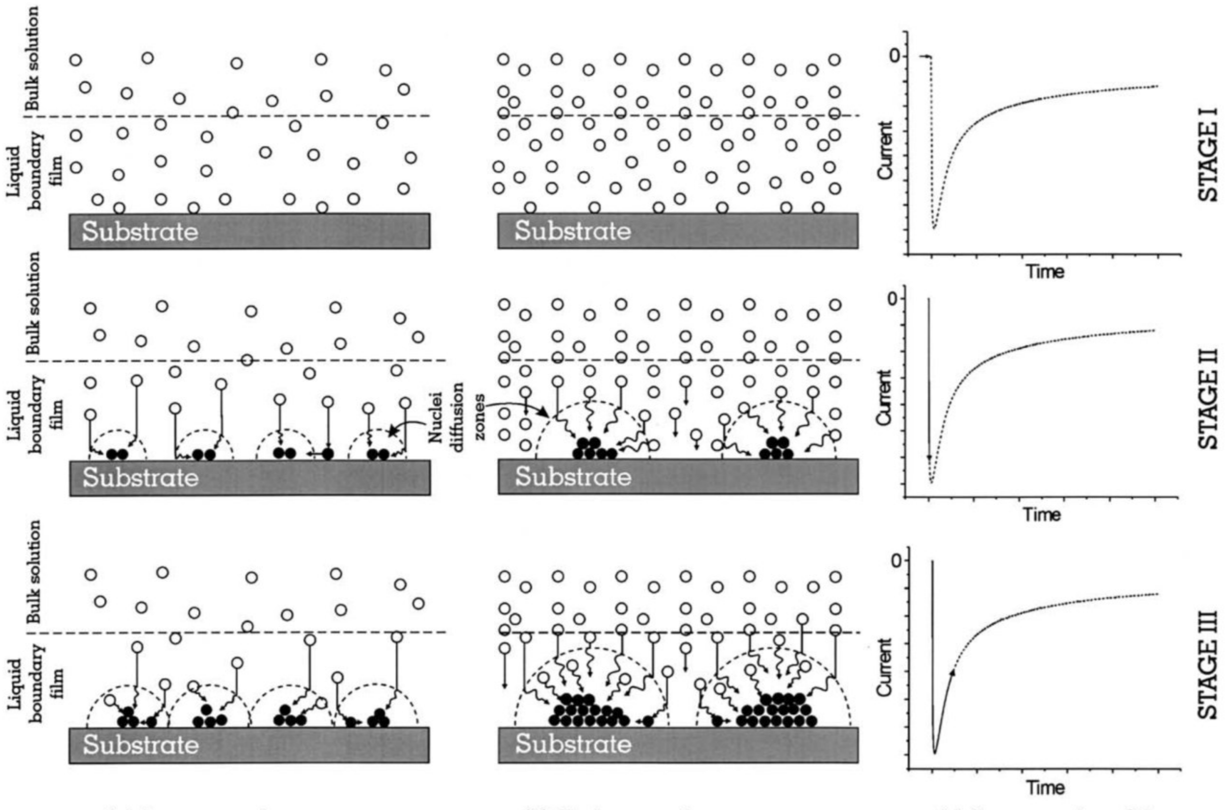

Figure 13: Different stages of chronoamperometry and their corresponding chronoamperograms [85]

Chronoamperometry was measured using a Bio-Logic VMP3 electrochemical workstation. Zinc foil was used as both the working and counter electrodes. Applied overpotential was set to either -135 mV (project 1) or -120 mV (project 2), both versus equilibrium potential of zinc. Chronoamperometry was conducted for different durations depending on the investigation.

2.3 Electrochemical Impedance Spectroscopy (EIS)

Electrochemical Impedance Spectroscopy (EIS) is a technique used to probe the response of a system to an electrical perturbation with varying frequency. Over a wide range of frequencies (i.e. 1 Hz to 1 MHz) various inductive and capacitive effects can be observed in a system. The electrochemical cell is exposed to a load at each frequency, the corresponding current flowing through the cell is measured, and software is used to deduce this value to its real and imaginary impedance components. There are two principal equations which describe the real and imaginary impedance components of EIS, shown in Equations 15 and 16, respectively, below:

$$Z' = R_s + \frac{R_{ct}}{1 + \omega^2 R_{ct}^2 C_{dl}^2} \qquad \mathbf{(15)}$$

$$Z'' = \frac{R_{ct}^2 C_{dl} \omega}{1 + \omega^2 R_{ct}^2 C_{dl}^2} \qquad \mathbf{(16)}$$

where Z' and Z'' are the real and imaginary components of impedance, R_s is the resistance of the electrolyte, R_{ct} is the charge transfer resistance, ω is the applied frequency, and C_{dl} is the capacitance of the double layer.

Figure 14 shows a typical Nyquist plot, which can be further broken down to its two main components: the activation-controlled region (represented by the semicircle) and the diffusion-controlled region (represented by the linear tail).[86] Solution and charge transfer resistances are frequency independent and thus are both real quantities.[87] Ion diffusivity is measured in the diffusion-controlled region, and is observed at low frequencies. The inset in Figure 14 shows a simplified circuit used to model the experimental data.

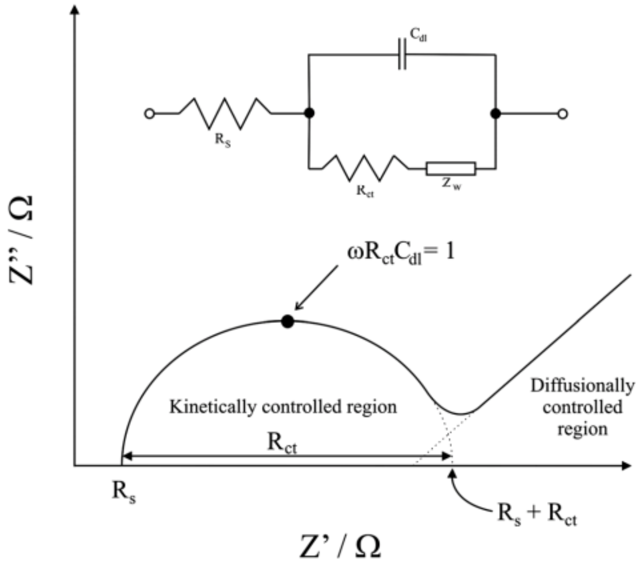

Figure 14: Typical Nyquist plot. Inset: simple Randles equivalent circuit for fitting EIS spectrum for an electrochemical cell [86]

In this project EIS measurements were conducted on a Bio-Logic VMP3 electrochemical workstation. Symmetric coin cells using zinc as both the working and counter electrodes, and an absorbed glass mat (AGM) separator were constructed for the testing. Firstly, a 10 mV DC square wave was applied, followed by scanning of AC frequencies from 100 MHz to 10 mHz.

2.4 X-Ray Diffraction (XRD)

X-ray diffraction is a crystal structural characterization tool and is predominantly used to determine atomic arrangement in crystalline materials. In principle, it features a source and a detector. In the source, a high voltage filament is used to accelerate electrons toward a target (e.g. copper). The incident electrons excite core electrons from atoms in the target, which during relaxation emit X-rays of characteristic wavelength (e.g. Cu-Kα X-rays have a wavelength of approximately 1.54 Å). The X-rays are then fired at the sample of interest in which they are diffracted by the different crystalline planes and finally detected by the detector. Since different crystalline planes interact with X-rays in specific geometries, the scanning is carried out over a range incidence angles. Figure 15 below shows a schematic of the interaction between X-rays and a typical sample.

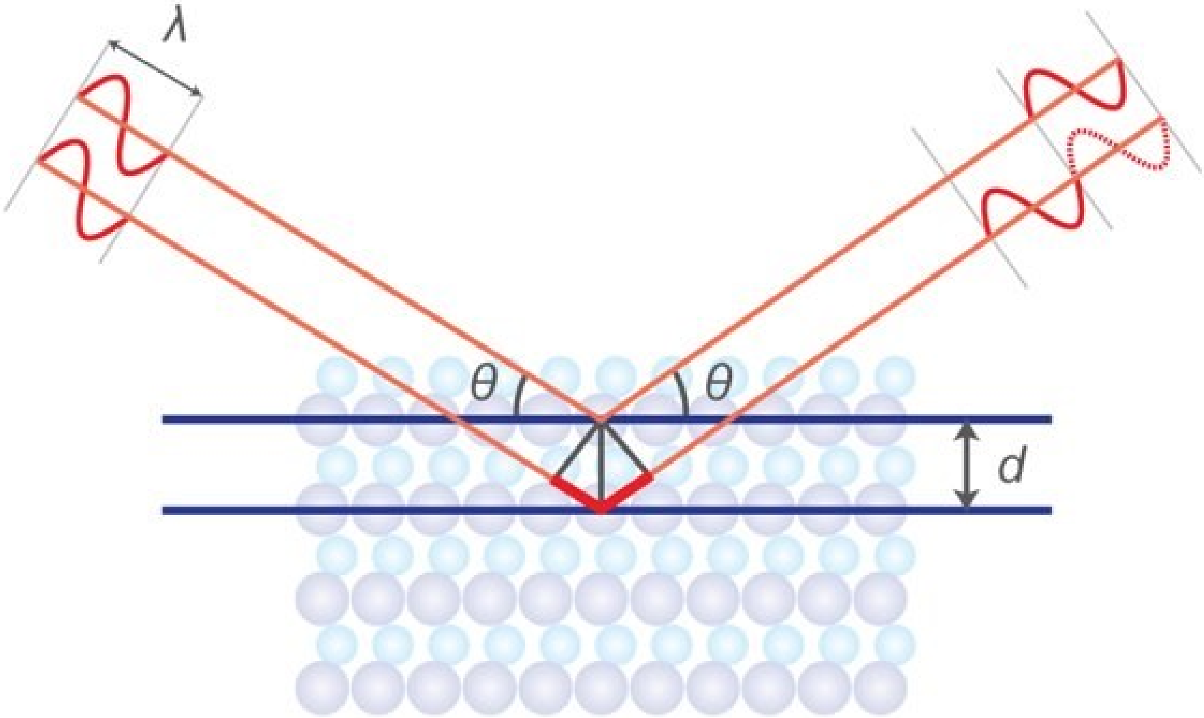

Figure 15: Schematic showing the interaction between x-rays and a typical crystalline sample [88]

After the measurement is completed a plot can be obtained showing the detected X-ray intensity at each incidence angle, as shown in the top of Figure 16. The spectrum can be compared to databases to compare to other materials and polymorphs, seen at the bottom of Figure 16.

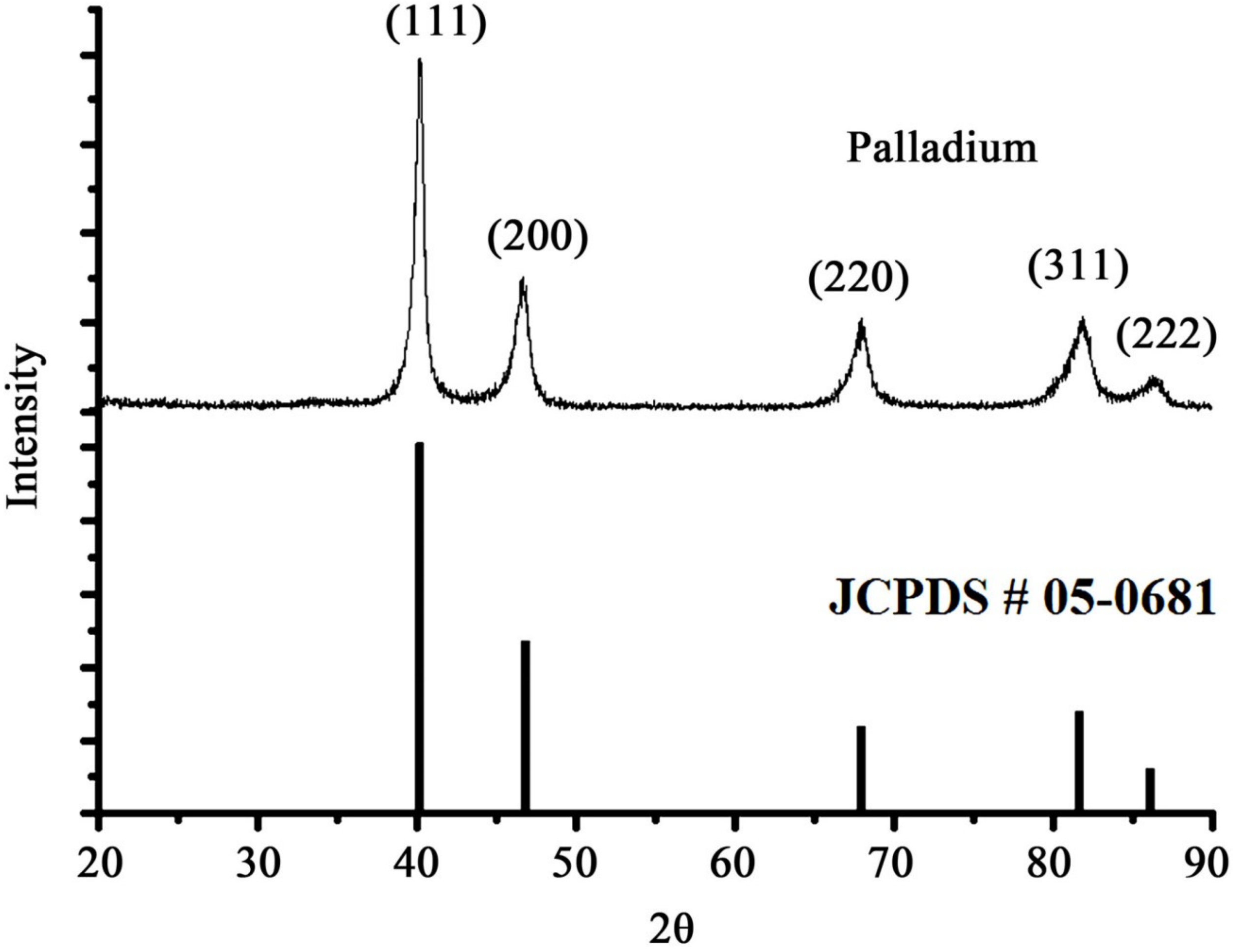

Figure 16: Top: XRD spectrum of palladium metal. Bottom: corresponding database card [89]

In-phase incident rays are diffracted differently depending on the plane they interact with leading to a phase difference between the rays. Diffracted rays will only be detected if they interfere constructively, i.e. if the Bragg condition is met, shown in Equation 17 below:

$$n\lambda = 2d_{hkl}\sin\theta \qquad \mathbf{(17)}$$

where n is an integer number, d_{hkl} is the spacing between two planes, and θ is the incidence angle. This method can be used to identify the crystalline planes present in a material.

The sizes of the crystal planes can also vary depending on the synthesis and processing conditions of a sample. A crystalline material can further be described as a single crystal (in which the entire sample is made of an unbroken crystal with no grain boundaries) or a polycrystal (in which the sample is made up of a number of individual crystals of different size and orientation). The size of a crystal can be obtained from the XRD spectrum by applying the Scherrer method, shown in Equation 18:

$$d = \frac{K\lambda}{(FWHM)\cos\theta} \qquad (\mathbf{18})$$

Where d is the size of the crystal, K is the Scherrer shape constant, $\boldsymbol{\lambda}$ is the wavelength of the X-rays, FWHM is the full width at half maximum of the corresponding peak in the XRD spectrum, and θ is the incidence angle. Some common K values from literature are 0.94 for spherical crystals, 1.00 for nanorods, and 0.89 for platelets.[90]

In this project XRD characterization was carried out on a Bruker D8 Discover X-ray diffractometer using a copper target and a wavelength of 0.154 nm (Cu Kα). The measurement range was 10°-90° at a scan rate of 0.2 degrees per second. Glancing Incidence XRD was performed on a PANalytical MRD X'pert Pro diffractometer, Cu Kα source and a 0.3° incidence angle above selected 2θ with a parallel X-ray beam setup.

2.5 Fourier Transform Infra-red Spectroscopy (FTIR)

Molecules have different light absorption properties depending on the bonds they are constituted of. FTIR spectroscopy is used to probe the absorbance of infra-red light in different materials. As infra-red light passes through a molecule, certain wavelengths will be absorbed by the molecule and be converted to physical motion. With exposure to infra-red radiation, molecules experience a change in their dipole moments leading to a change in the energy state.[91] This excitation can be manifest in stretching, twisting, scissoring, bending or translation of a molecule.

The transmitted light can be captured by a detector and analysed to determine the types of bonds present in the sample.

An FTIR spectrophotometer operates by firing a broad-band beam of infra-red radiation through a partially reflective mirror leading to beam splitting. The split beams are directed to one fully reflective stationary mirror, and a fully reflective moving mirror. The split beams reflect off these mirrors, interact with the sample and are then collected at the detector. The moving mirror is used to add phase difference to the incident rays. During constructive interference (no path difference between infra-red rays from the moving and stationary mirrors) maximum signal reaches the detector after passing through the sample. In contrast, when the interference is destructive, no signal is expected at the detector. The measurement is carried out at a variety of phase angles producing an interferogram at the detector. This is then converted to a frequency spectrum using a Fourier transform. The spectrum can be compared to databases to identify specific bonds responsible for absorption of light, and through this, the entire molecular landscape can be identified. Figure 17 below illustrates the operation of an FTIR device.

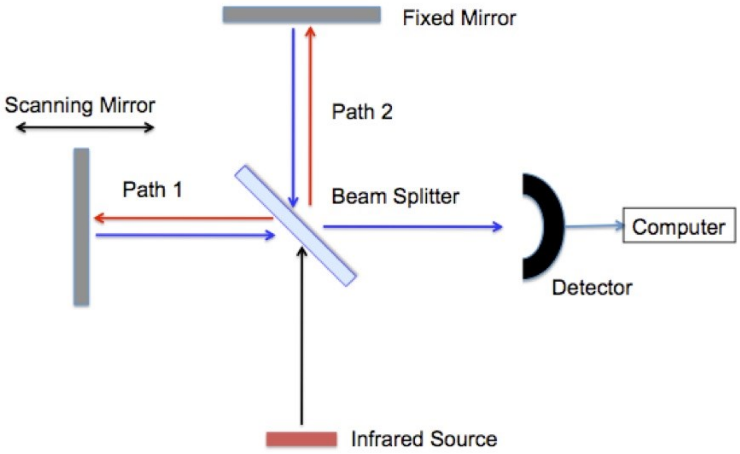

Figure 17: Working principle of an FTIR interferometer [92]

FTIR spectroscopy was performed on a Bruker Optics Vertex 70 Spectrometer in the wavenumber range of 400 cm^{-1} to 4000 cm^{-1} with a repetition of 20 scans.

2.6 X-Ray Photoelectron Spectroscopy (XPS)

X-ray photoelectron spectroscopy is an extremely surface sensitive (~ 30 nm) characterization technique. The spectrometer uses a filament and anodic targets to generate characteristic x-rays which are then fired at a sample. Due to their high energy, the x-rays are able to dislodge core electrons from a sample by providing them enough energy to escape the attraction of the nucleus. The ejected electrons are then detected and counted over a range of energies to give a unique 'fingerprint' of the material. The XPS survey spectrum can then be de-convoluted to identify individual electrons that are ejected and the energy levels and orbitals they originate from. This information is used to piece together the composition of the sample material. Figure 18 displays a sample XPS survey, and the deconvolution on a specific peak to determine specific orbitals involved in scattering.

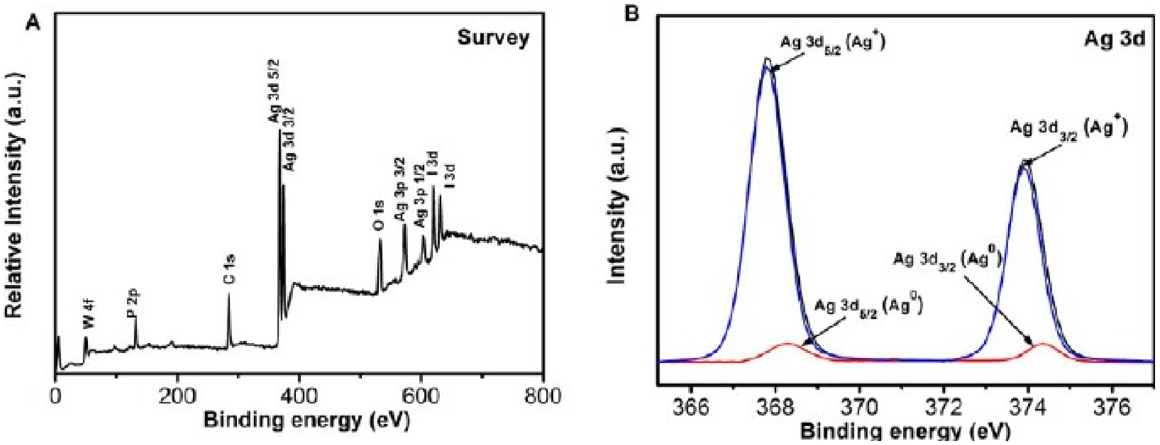

Figure 18: (a) A sample XPS survey and (b) de-convoluted spectrum [93]

A Thermo-VG Scientific ESCALab 250 microprobe was used to record XPS spectra. The spectra were taken at 1486.6 eV and 49.3 W, using a 200.0 μm beam size. Reported binding energies were normalized against the C1s peak at 284.8 eV. The chamber pressure was maintained at 2.0 nPa during testing. A wide survey (0-1350 eV) was conducted for each sample to determine the surface elemental composition of the samples. This was followed by scanning over a narrower energy window to obtain high energy resolution spectra of the elements.

2.7 Scanning Electron Microscopy (SEM)

Electron microscopy is used to image materials at the nanoscale by measuring their interaction with an incident stream of electrons. Scanning electron microscopy operates in several modes which either detect incident electrons bouncing back off the sample (backscattered electrons) or electrons that are given off by the sample in response to being excited by the incident beam (secondary electrons). Secondary electrons have very low interaction volume in the sample since they typically have much lower energy than backscattered electrons. Due to this, they give great topographical contrast and can be used to image surface morphology. The process of backscattering is highly dependent on atomic number, and can thus be used to determine the composition of a sample. Samples may also give off characteristic x-rays as core electrons are excited by the incident beam. These x-rays can be collected in the Energy Dispersive X-ray Spectroscopy (EDS) mode and be used to measure the composition of the material. Since these x-rays have a high interaction volume, this mode gives a well-averaged count.

The first component of an SEM apparatus is an electron source. Electrons may either be generated thermionically or by electric field. Thermionic emission involves using thermal energy to overcome the work function of a metal. Electrons in a filament are heated to free them from host atoms. For example, a tungsten (W) filament has a work function of 4.5 eV and would thus require heating to 2800 K to free electrons. Field emission uses a high electric field to overcome the work function, with electrons being freed by quantum mechanical tunneling. Field emission offers the benefit of lower emission temperatures and higher beam brightness, but need much higher vacuum to operate.

In both cases, a secondary electric field is used to focus extracted electrons into a coherent beam and directed towards the focusing system. Electrons from the source are directed through a series of electromagnetic lenses in order to be focused into a spot of approximately 1 nm (original beam has a spot size of ~ 5 nm). Sets of scan coils are then used to raster the electron beam across the surface of the sample. Electrons collected after interaction with the sample are passed through a detector and an amplifier to add gain to the signal before an image is projected onto a monitor. These components are illustrated in Figure 19 below.

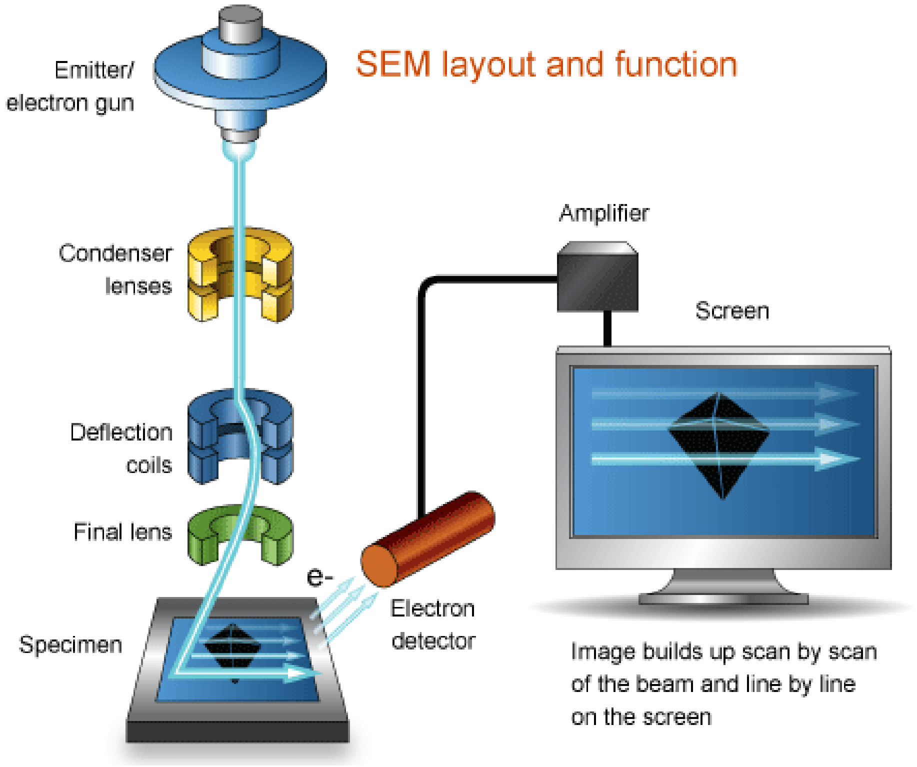

Figure 19: Components and principle of operation of an SEM [94]

SEM for all samples in this project was performed on a Zeiss LEO 1530 FESEM with an accelerating voltage of 5 kV.

2.8 Transmission Electron Microscopy (TEM)

Transmission electron microscopy is a complementary characterization technique to scanning electron microscopy, where incident electrons are fired at a sample and those transmitted through it are detected and counted. In this case, as incident electrons pass through the sample, they are scattered by nuclei, and thus require a set of lenses to focus them onto a detector screen. Since the scattering is proportional to atomic number, TEM can be used to create elemental distribution maps based on the electron scattering profile. Crystalline materials have regularly spaced planes and thus there are certain scattering directions which are preferred, and will hence be registered with higher intensity at the screen. Additionally, a TEM may also be used to measure electron diffraction through a crystalline sample, referred to as Selected Area and by rotating the sample over all directions, an averaged diffraction pattern can be obtained. Figure 20 below shows the basic setup of a TEM device.

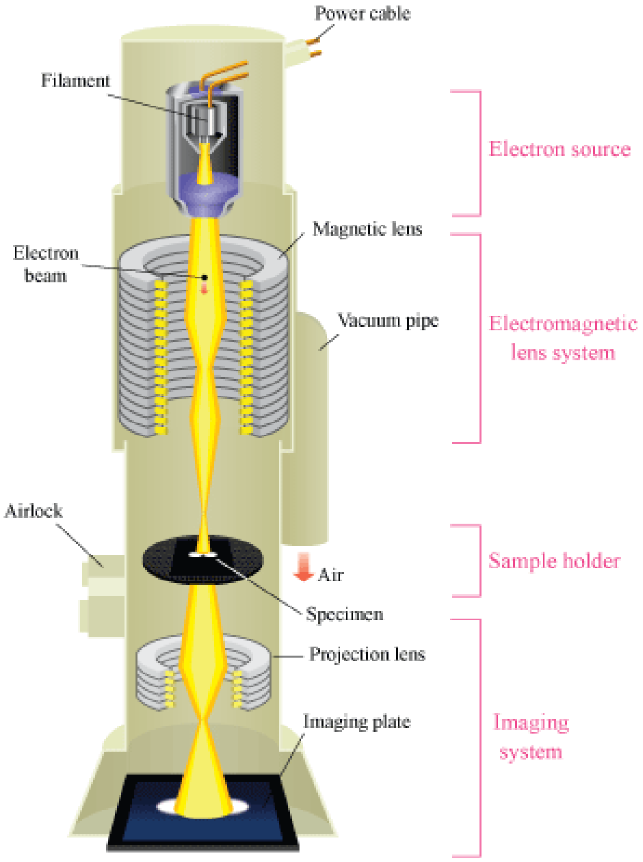

Figure 20: Basic principle of a TEM [95]

HRTEM of dendrite samples was performed on a Zeiss Libra 200MC TEM using a 200 kV acceleration voltage. Dendrite samples were directly drop-casted onto the copper grid in ethanol solvent. The elemental mapping was performed using the electron energy loss spectroscopy (EELS) method on the scanning mode of the TEM instrument (STEM) via electron.

2.9 Battery Testing

Cycle life for small (~ 1.13 cm^2 in 1.15 mAh cell) and large (~ 20.25 cm^2 in 7 mAh cell) cells was tested using the constant current constant voltage (CC-CV) protocol between 1.4 V and 2.1 V vs. Zn^{2+}/Zn. In this mode, the cell is first charged to 2.1 V using the desired current rate (i.e.

1 C or 4 C), and then maintaining 2.1 V using the constant voltage mode until the corresponding current decreases to 10% of the original value (i.e. 0.1 C or 0.4 C, respectively).

To measure rate capability, the cycling C-rate was varied to observe the effect of current density on discharge capacity. Measurements were conducted at 0.2 C – 0.5 C – 1 C – 2 C – 4 C – 0.2 C using a constant current (CC) charge-discharge protocol.

Float capacity was studied to quantify the impact of parasitic capacity losses that are commonly observed at high states of charge. In this case, the cells were first charged to 2.1 V at constant 0.2 C current, and then maintained at 2.1 V for 72 hours in the constant voltage mode.

Self-discharge of batteries was measured by first charging them to 2.1 V and then monitoring voltage decline over a 72-hour period.

Battery testing was conducted either in coin cells, Swagelok cells or a bespoke large battery (shown in Appendix 1). For the smaller cells, a minimum of 5 samples were tested for each condition with an error threshold of 10%. For larger cells, 3 samples of every condition were tested, also with a 10% error threshold.

The large battery was used to test the performance of the PEG additive in the ReHAB battery system at a size that is more representative of real world applications. It was used to see the effect of upscaling the ReHAB system and how it would behave in a larger setting. The main challenge of this expansion, as with any other system, was that the probability of failure from a single artefact is much higher than in a smaller system due to a larger chance of them occurring.

3.0 Surface Adsorption of Polyethylene Glycol to Suppress Dendrite Formation on Zinc Anodes in Rechargeable Aqueous Batteries

3.1 Section Introduction

Polyethylene glycol (PEG) is a polymerized form of ethylene oxide and features a repeating ether linkage between successive monomers. It differs from polyethylene oxide (PEO) by having lesser molecular weight (less than 20000 $g{\cdot}mol^{-1}$) which is achieved via a lower degree of polymerization during the synthesis process. PEG can be found in different geometries such as branched (a primary structure from which secondary chains are grown), brush-like (PEG chains grown from a polymer backbone), and linear, which will be the type used in this project. The polymer has been used as a water-soluble stabilizer and has a wide range of applications including in cosmetic products, drug delivery, organ and blood donations, and electrodeposition.[96–98]

In the field of electrochemical deposition of metals, PEG is used as a brightener since it is attracted to regions with higher electrochemical potential (areas on the electrode with higher elevation), hence forcing ions to be reduced in other regions.[99] This has the effect of ‘levelling’ the surface as it ensures crevices are filled up and the electrode can achieve a flatter morphology. This process has great importance as it improves the quality of electroplating by ensuring a uniform crystalline grain structure.[100] In the case of batteries, PEG is particularly useful as it can help control the reduction and deposition of metallic ions from solution onto the anode during the charging process. In this manner, PEG can help to prevent cell failure from excessive and non-uniform dendrite growth.

This project investigates the application of PEG as an electrolyte additive to mitigate the formation of dendrites on zinc electrodes in the ReHAB system. The scope of the project is narrowed to the energy storage field, and in particular storing power generated from sustainable and renewable sources of energy. It is in this market that such batteries are aiming to become competitive alternatives. Specifically, the goal of this project is to lengthen the functional lifespan of ReHABs by inhibiting premature failure from dendrite short-circuiting. This is done to make more efficient use of lithium as an active electrode material thus improving the overall cost-efficiency of the ReHAB. Several electrochemical and material characterization techniques will the employed in order to evaluate the performance improvements derived by the inclusion of PEG in this specific battery chemistry.

3.2 Results and Discussion

3.2.1 Electrochemical Characterization

Corrosion

In a mildly acidic electrolyte the zinc electrode experiences considerable corrosion which has undesired consequences on the performance and safety of the system. Firstly, the reduction of hydrogen ions is a complementary process of corrosion.[101] After reduction of H^+ ions, hydrogen gas is formed and released from the surface of the electrode. This has severe implications on the safety of the battery since it is a closed system. A build-up of gas could pose an explosion risk as it exerts extreme pressures on the cell architecture. Secondly, evolution of hydrogen gas decreases the concentration of hydrogen ions in the electrolyte solution, thereby leading to increase in pH. While not dangerous, this increase will change the electrochemical environment inside the cell and may lead to other unwanted side reactions.

Corrosion was measured using linear polarization (see Section 2.1) and the results of these experiments are presented in Figure 21 and summarized in Table 1. It is generally seen that the addition of PEG to the electrolyte leads to an increase in the corrosion potential and a decrease in the corrosion current density. This trend is commonly noted in literature where an increase in inhibitor concentration corresponds to the corrosion potential becoming more positive.[102,103] Increasing the concentration of PEG200 from 0.1 vol.% to 1 vol.% increases the corrosion potential (from -1.012 V to -0.992 V) and decreases the corrosion current density (from 0.62 $mA \cdot cm^{-2}$ to 0.29 $mA \cdot cm^{-2}$). Increasing the concentration further was actually seen to have a detrimental effect on corrosion inhibition. Using larger molecular weights of PEG polymer also resulted in similar decrease in corrosion inhibition. Increasing the molecular weight from 200 g·mol^{-1} to 400 g·mol^{-1} decreased the corrosion potential (from -0.992 V to -0.996 V) and increased the current density by 0.8 mA·cm^{-2} (from 0.29 mA·cm^{-2} to 1.09 mA·cm^{-2}).

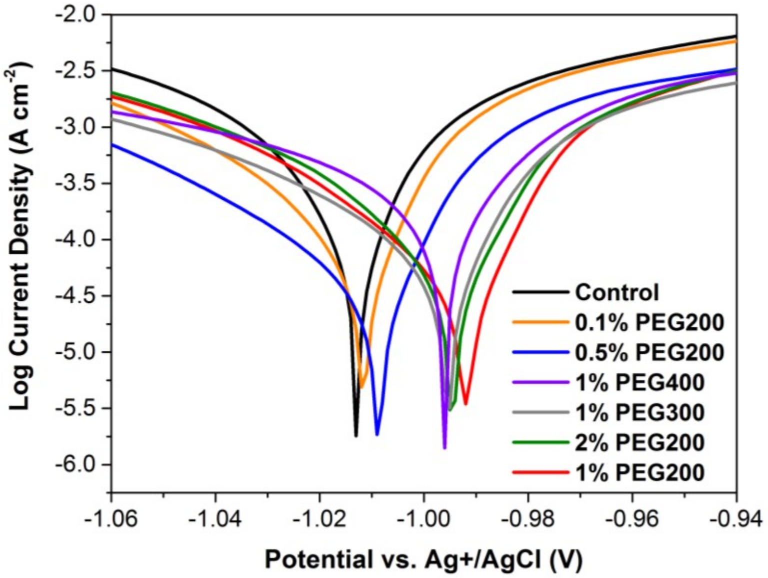

Figure 21: Linear polarization experiments to measure corrosion of zinc foil in various electrolytes containing PEG additive

Table 1: Summary of corrosion potentials and currents from linear polarization experiments

Condition	Corrosion Potential [V] vs. Ag$^+$/AgCl	Corrosion Current Density [mA·cm^{-2}]
Control	-1.013	1.05
0.1 vol.% PEG200	-1.012	0.62
0.5 vol.% PEG200	-1.009	0.31
1 vol.% PEG200	-0.992	0.29
2 vol.% PEG200	-0.994	0.43
1 vol.% PEG300	-0.995	0.46
1 vol.% PEG400	-0.996	1.09

The role of PEG here is to occupy preferential nucleation sites on the surface of the zinc electrode and are hence able to impede the adsorption of H$^+$ ions from the electrolyte which is an important mechanism in the hydrogen evolution reaction.[104] By selecting the optimal concentration and molecular weight of PEG, corrosion can be significantly suppressed and this should allow for a much longer cycling life of the battery.[105] By increasing the corrosion potential and decreasing the corrosion current density, the electrochemical window of the cell is moved further away from the hydrogen evolution zone, and the rate of the corrosion reaction is decreased. For this reasoning, 1 vol.% PEG200 was selected as the optimal inhibitor condition as it increases potential by 20 mV and decreases current density approximately 72%.

Chronoamperometry (CA)

Application of a negative potential at the zinc anode (i.e. during the cell charging process) creates several overpotentials at the surface.[106] This attracts Zn^{2+} ions from solution and allows them to reduce and deposit on the electrode surface. In specific conditions, the reduction process is localized to certain areas leading to irregular surface morphology. Higher points on the surface will have a higher localized overpotential leading to more accelerated growth. Overall, sharp features will begin to form at these locations and grow in a perpendicular direction to the surface, commonly referred to as dendrites.[106] Dendrite growth on the zinc electrode is another failure mechanism that limits how well aqueous batteries can perform.[107,108] Since they have a high aspect ratio, dendrites can penetrate through the separator and form a short-circuit between the anode and cathode. This then causes the premature failure of the cell.[109] The dendrite growth process was quantified using chronoamperometry measurements (see Section 2.2).

The process of nucleation of dendrites and the surface (2D) diffusion of Zn^{2+} ions occurs at very early timescales (~ 15 s). These are shown in the inset graph in Figure 22. The nucleation and 2D diffusion current is significantly reduced for 1 vol.% PEG200 sample, evident in the lower absolute spike current (3.99 $mAcm^{-2}$ vs. 8.64 $mAcm^{-2}$). This stems from PEG polymers occupying preferred nucleation sites on the electrode and blocking surface diffusion of adsorbed ions. The 1 vol.% PEG200 sample also displays much steadier and lower absolute 3D diffusion current (2 s < t < 15 s) than the control sample.

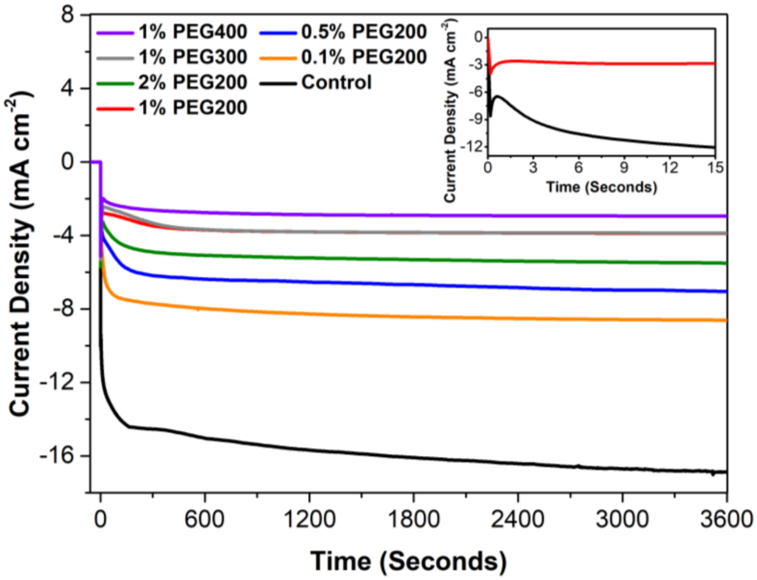

Figure 22: 1 h chronoamperograms of zinc foil in various PEG-based electrolytes at -135 mV overpotential vs. OCV. Inset: early chronoamperograms

The main graph in Figure 22 shows the long-term chronoamperograms of zinc foil in the different PEG electrolytes. All the PEG-based electrolytes are able to decrease the absolute current density of the zinc deposition process signifying the effectiveness of PEG as an inhibitor to the reduction Zn^{2+} ions. Examining the effect of concentration, 1 vol.% PEG200 is able to show the lowest long-term absolute deposition current density of just 3.89 $mAcm^{-2}$ (t > 500 s). Increasing the molecular weight of PEG from 200 $gmol^{-1}$ to 400 $gmol^{-1}$ also has a similar effect as the long-term 3D diffusion current decreases further to 2.94 $mAcm^{-2}$. This is likely due to a higher blocking effect on the deposition sites by the longer chains of the higher molecular weight PEG polymers.[98] In the intermediary period (15 s < t < 500 s), an increase in the absolute deposition current density of the PEG samples was noted. This is correlated to the transition between primary and secondary types of dendrites on the electrode surface, and is further expanded on in the SEM analysis.

Once the PEG samples reach the long-term 3D diffusion current ($t > 500$ s), they barely experience any variation in the deposition current density. This section of the profile is proportional to the surface area exposed to the electrolyte.[85] A graph with a negative slope (absolute current increasing with time) would refer to a scenario where the surface area is increasing – a situation only possible when the aspect ratio of surface features grows i.e. conversion of the planar structure of zinc foil to the rough structure created by dendrites. Hence it can be concluded by chronoamperometry testing that the main role of PEG polymers is to control the adsorption of Zn^{2+} ions and force a more uniform deposition across the surface.

3.2.2 Battery Performance

Cycling Performance of Small Cells

The results of cycling performance of different PEG additive concentrations and molecular weights are shown in Figure 23. As the concentration of PEG200 is increased from 0.1 vol.% to 1 vol.% both the specific discharge capacity and retention of cells increase significantly. A further increase to 2 vol.% yields no improvement. Further, increasing the molecular weight of PEG from 200 $g \cdot mol^{-1}$ to 400 $g \cdot mol^{-1}$ leads to substantial decrease in performance, with 1 vol.% PEG300 only being able to achieve 60.53 $mAhg^{-1}$ at 300 cycles. It is evident that the optimal additive condition for cycling at 1 C is 1 vol.% PEG200.

Improvement in capacity retention in long-term cycling with the addition of 1 vol.% PEG200 to the electrolyte is due to PEG's ability to minimize parasitic corrosive reactions of the zinc anode. This is accomplished by maintaining a higher degree surface uniformity and increasing the hydrogen evolution overpotential than the control electrolyte. This allows for more zinc to deposit/dissolve from the anode during cycling, and facilitates a larger amount of lithium to intercalate/deintercalate from the cathode. Overall, this process decreases capacity fading in the battery.

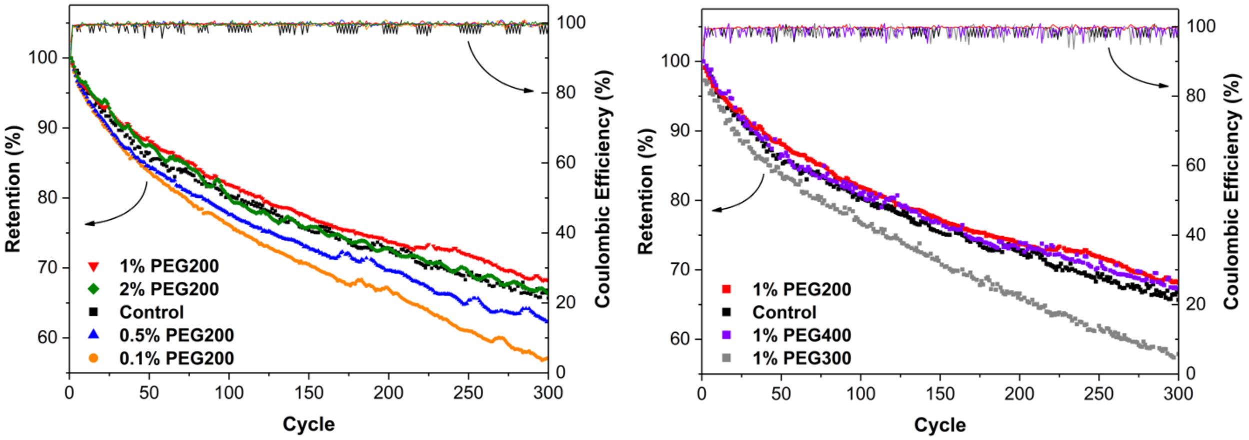

Figure 23: Specific discharge capacities and coulombic efficiencies of small cells at 1 C rate made with different concentrations (left), and different molecular weights (right), of PEG additive in the electrolyte

While the 1 C cycling performance showed an improvement in discharge capacity and retention with the addition of PEG in the electrolyte the changes were only incremental. To further stress the system the cycling was repeated at 4 C for 1000 cycles using the same CC-CV protocol as before. These results are shown as the red and black graphs in Figure 24 representing the 1 vol.% PEG200 and control samples, respectively. In this case there is a marginal improvement in cycling performance with the addition of 1 vol.% PEG200 (91.8 $mAhg^{-1}$ vs. 80.6 $mAhg^{-1}$ initial capacity and 44.3 $mAhg^{-1}$ vs. 41.5 $mAhg^{-1}$ end-of-test capacity) over the control sample. An important observation was that even with the added stress of higher cycling current and more cycles, cell failure from dendrites was still not observable in the range of the test.

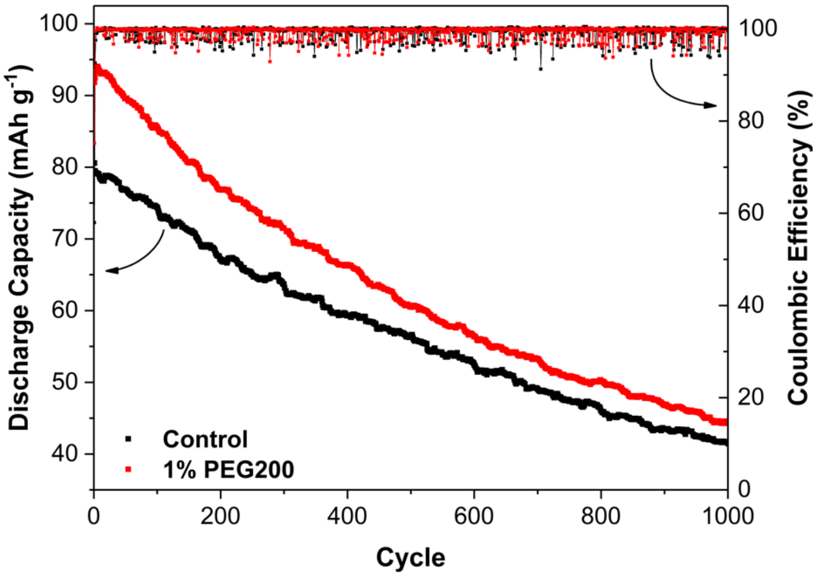

Figure 24: Cycling performance of small cells at 4 C

Accelerated Failure

In order to quicken failure from dendrites, the anodes from the cells were first exposed to chronoamperometry for 3 hours at -135 mV overpotential vs. OCV in the two electrolytes to grow dendrites on the surface. The electrodes were then used to assemble small cells and cycled at 4 C as earlier, and the results are presented in Figure 25. The initial capacities of the after-chronoamperometry samples are much higher than their before-chronoamperometry counterparts due to the increased electrochemical surface area exposed through a rougher surface from dendrite formation. The added surface area promotes higher rates of reduction and oxidation at the electrodes hence increasing the capacity.[110] The 1 vol.% PEG200 sample after-chronoamperometry is also able to cycle to 1000 cycles with acceptable discharge capacity and retention. In contrast, the control sample after-chronoamperometry begins to fail at just 190 cycles, and by approximately 460 cycles has completely failed. At the end of the test the 1 vol.% PEG200 after-chronoamperometry sample can still achieve 41.2 mAhg^{-1} while the control after-chronoamperometry sample attains just 7.6 mAhg^{-1}. It is here that the true benefit of PEG is realized – by its ability to mitigate cell failure by suppressing runaway growth of dendrites on the anode through a surface adsorption mechanism.

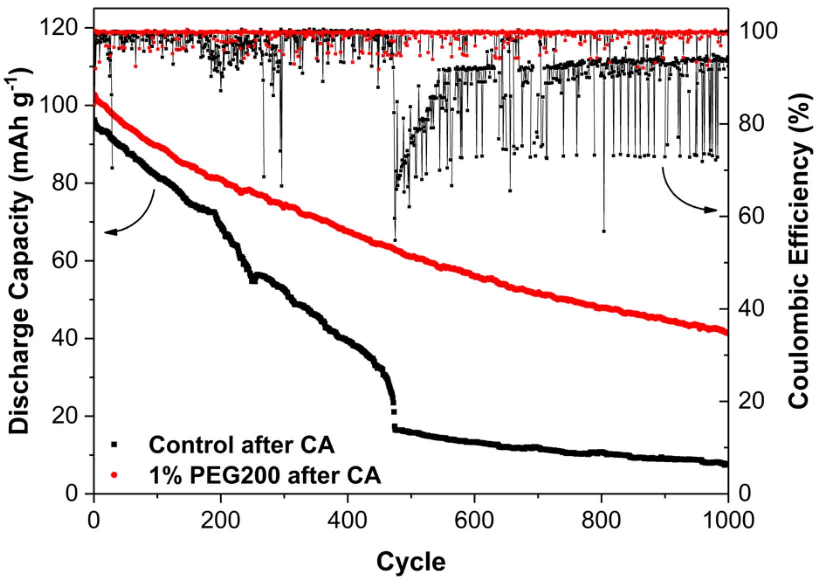

Figure 25: Cycling performance of small cells at 4 C after pre-exposure to chronoamperometry for 3 hours at -135 mV overpotential vs. OCV

The sharp fluctuations in the after-chronoamperometry samples are a result of dendrite pre-growth on the electrodes. An increase in the electrode surface area also promotes parasitic reactions such as corrosion, and is the main reason why capacity fading is more prominent in these samples compared to those before chronoamperometry. The coulombic efficiency of the control after-chronoamperometry sample fluctuates even more sharply once failure has begun (i.e. after 190 cycles). This is due to maximal surface area being exposed to undesired reactions.[110]

Cycling Performance of Large Cells

The prospective for upscaling this system was gauged by cycling on a bespoke large cell shown in Appendix 1. This test was also conducted at 1 C under the CC-CV protocol. The sample with 1 vol.% PEG200 electrolyte, as shown in Figure 26, is able to exhibit a discharge (111.72 mAhg^{-1} vs. 103.95 mAhg^{-1}) capacity than the control sample after 100 cycles. Once again, the improved capacity retention of the 1 vol.% PEG200 sample is linked to lesser parasitic reactions on the anode which allow for better efficiency of zinc plating and dissolution compared to the control electrolyte. This facilitates a larger amount of lithium intercalation into the cathode, allowing more capacity to be had. The difference in capacity retention is expected to continue to increase as the batteries continue to cycle as PEG suppresses unwanted reactions. This result shows great promise for integration in larger aqueous energy storage systems.

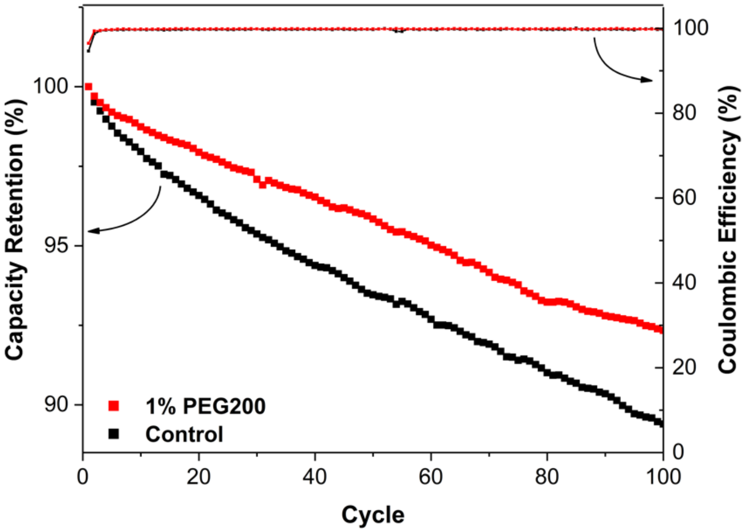

Figure 26:Cycling test of 7 mAh cells under 1 C current density

Rate Capability

Rate capability of the ReHAB system with PEG additive was tested to measure the impact of different cycling current densities on the capacity retention of cells. Between 0.1 vol.% and 1 vol.%, concentration of PEG200 has a positive effect on retention, as shown in Figure 27 (at 4 C, the retention increases from 31% to 39% with this change). A further increase to 2 vol.% has a negative impact on retention at higher rates. Increasing the molecular weight from 200 g·mol^{-1} to 400 g·mol^{-1} shows a sharp decline in retention at 4 C from 39% to just 21% (the poorest performing sample). As with prior tests, rate capability also shows 1 vol.% PEG200 to be the optimal condition.

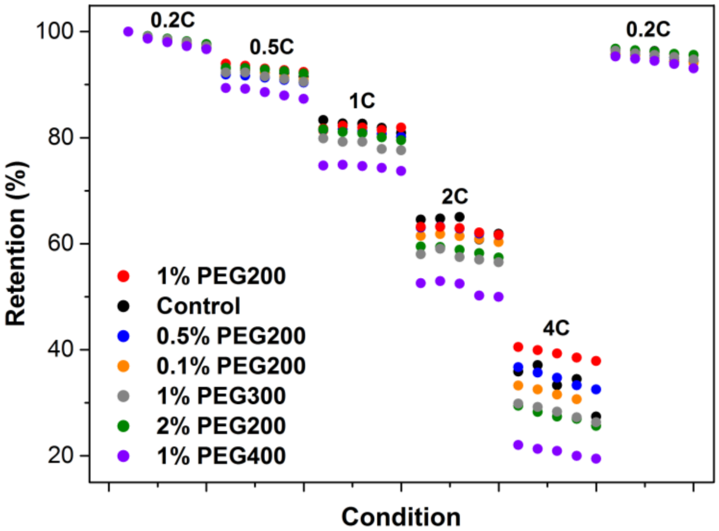

Figure 27: Rate capability of small cells containing different concentrations and molecular weights of PEG in the electrolyte

Float Capacity

Figure 28 shows the float capacity loss measured as a percentage of the original charge capacity (from the 0.2 C constant current charging step prior to floating) at 24 and 72 hours. In general, all PEG samples show poorer performance than the control except for 1 vol.% PEG200 which exhibits 0.72% lesser capacity loss over the 72-hour period. Once again it is seen that the 1 vol.% PEG200 condition shows best performance.

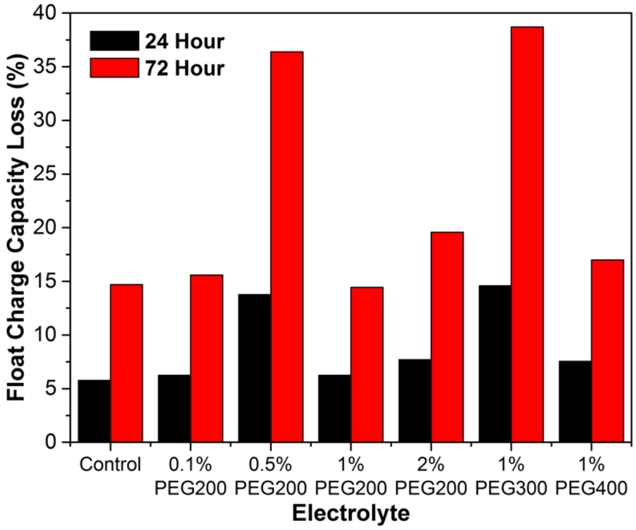

Figure 28: 24- and 72-hour float capacity loss of small cells with different concentrations and molecular weights of PEG in the electrolyte

Self-discharge

Lastly, the self-discharge of small cells was investigated. This is an important tool in gauging the shelf-life of battery systems. As presented in Figure 29, while all PEG samples show more self-discharge than the control sample after 72 hours, the 1 vol.% PEG200 is closest in performance. It only shows 0.32% poorer retention of voltage after three days, and is well within acceptable range.

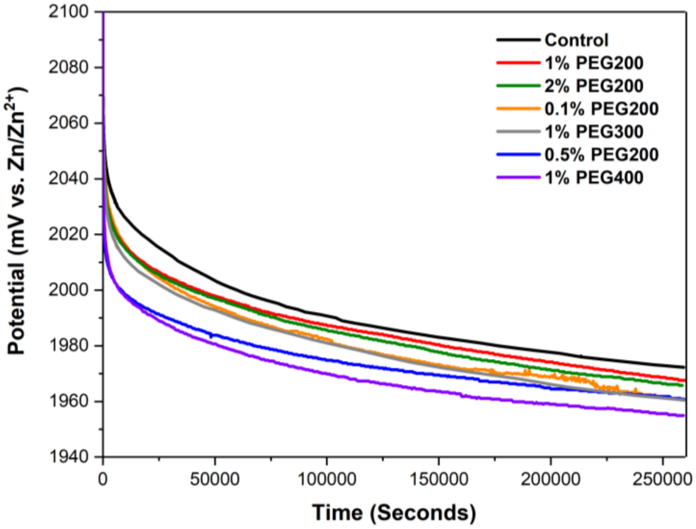

Figure 29: Self-discharge of small cells with different concentrations and molecular weights of PEG in the electrolyte

The recurring theme during battery testing is that 1 vol.% PEG200 excels in all the testing and presents the optimal concentration and molecular weight of the PEG additive for ReHABs. The conclusion of the battery testing is that 1 vol.% PEG200 can greatly improve the longevity of batteries since it is able to prevent premature failure from non-uniform dendrite growth.

3.2.3 PEG Adsorption

Electrochemical Impedance Spectroscopy (EIS)

In order to expound further on the specific manner in which PEG interacts with zinc electrodes, EIS was performed on symmetric zinc coin cells. This particular cell construction was chosen so that the working and counter electrodes were the same, thus avoiding any secondary impedances that would arise with a different electrode material. Specifically, EIS highlights frequency dependent characteristics of electrode reactions (i.e. capacitive and inductive behavior) which contribute to overall impedance. The EIS results for 1 vol.% PEG200 and control symmetric zinc small cells are presented as Nyquist plots in Figure 30 (left). It is evident that the addition of PEG200 to the electrolyte leads to quite a large increase in the impedance of the system caused by a much larger charge transfer resistance at the electrode.[102] Based on Warburg element, the diffusion coefficient of zinc ions was calculated to be 3.745E-11 $cm^2 \cdot s^{-1}$ and 5.635E-11 $cm^2 \cdot s^{-1}$ in the 1 vol.% PEG200 and the control samples, respectively.[45] The lower diffusion coefficient suggests that PEG polymers on the surface act as barriers to inhibit to charge transfer. These results are in agreement with chronoamperometry results where increasing the concentration of PEG200 in the electrolyte resulted in lower absolute 3D diffusion current (i.e. lower rates of ion reduction).

EIS was performed again on samples after 50 cycles of charge-discharge to ascertain whether the effect of PEG was lessened by cycling. In order to carry out the measurements, small cells were first cycled using the CC-CV protocol used earlier, then disassembled, and the anodes were then used to construct symmetric cells. The results of this study are shown in Figure 30 (right). A notably higher impedance in the 1 vol.% PEG200 sample is indicative of retained PEG activity even after cycling. It also shows that PEG adsorbs and desorbs during cycling and is still able to have an effect even after a large number of cycles (if this were not the case all the PEG would adsorb in the first cycle and the effect would immediately diminish in successive cycles). It is through this adsorption-desorption mechanism that the cycle life of PEG cells is vastly improved over the control.

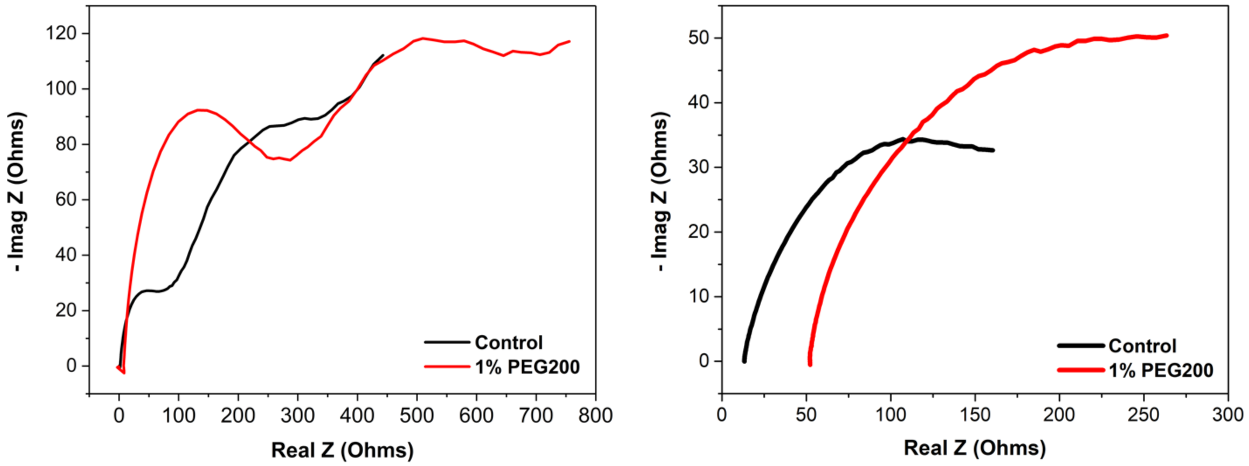

Figure 30: Nyquist plots of EIS measurements conducted on 1 vol.% PEG200 and control symmetric zinc small cells before cycling (left) and after 50 charge-discharge cycles (right)

Fourier Transformed Infra-Red Spectroscopy (FTIR)

It is clear from the battery testing and EIS results that PEG polymers in the modified electrolytes interact with the zinc anode to enhance the cycling performance of the ReHAB system. FTIR was employed to further probe this interaction. Since this technique is sensitive to covalent bonds in samples, zinc electrodes can be prepared in different conditions and tested to shed light on the specific behavior of PEG.[111] In general, several signature stretching vibrations unique to the PEG polymer were observed during testing: (1) between 3600 cm^{-1} and 3200 cm^{-1} denoting hydroxyl stretching, (2) ~ 1400 cm^{-1} denoting C-H bending and scissoring, (3) ~ 1160 cm^{-1} denoting symmetric C-O-C stretching, (4) ~ 1100 cm^{-1} denoting C-O stretching, (5) ~ 1060 cm^{-1} denoting CO-C axial deformation, and (6) ~ 966 cm^{-1} denoting C-C stretching.[112,113] Zinc anodes were exposed to four different electrochemical tests to investigate the role of PEG.

Firstly, charge and discharge processes were simulated using cyclic voltammetry. This was specifically chosen since it offers a high degree of control over the potential experienced at the electrode, and was tuned to a low scan-rate such that PEG polymers had sufficient time in which to interact. In the charging step, the sample was scanned using DC voltage from the open circuit potential (-0.960 V vs. $Ag^+/AgCl$) to -1.500 V vs. $Ag^+/AgCl$. In the discharge step, the potential was first swept negatively from -0.960 V to -1.500 V and then positively to -0.450 V, all potentials vs. $Ag^+/AgCl$. Both charging and discharging scans were conducted at a sweep rate of 1 $mV \cdot s^{-1}$. The electrode samples were analyzed by FTIR and the results are shown in Figure 31 (left). The peaks from the transmittance spectra can be matched perfectly to the PEG polymer. A key observation is that the transmittance of the charge spectra is much lower than the discharge signifying that there is a higher amount of PEG present on the electrode after the charge step (compared to the discharge).[114] Since the sample was rinsed after the CV and prior to FTIR testing, the presence of PEG in the spectra points towards a more permanent adhesion between the polymers and the electrode (i.e. adsorption).

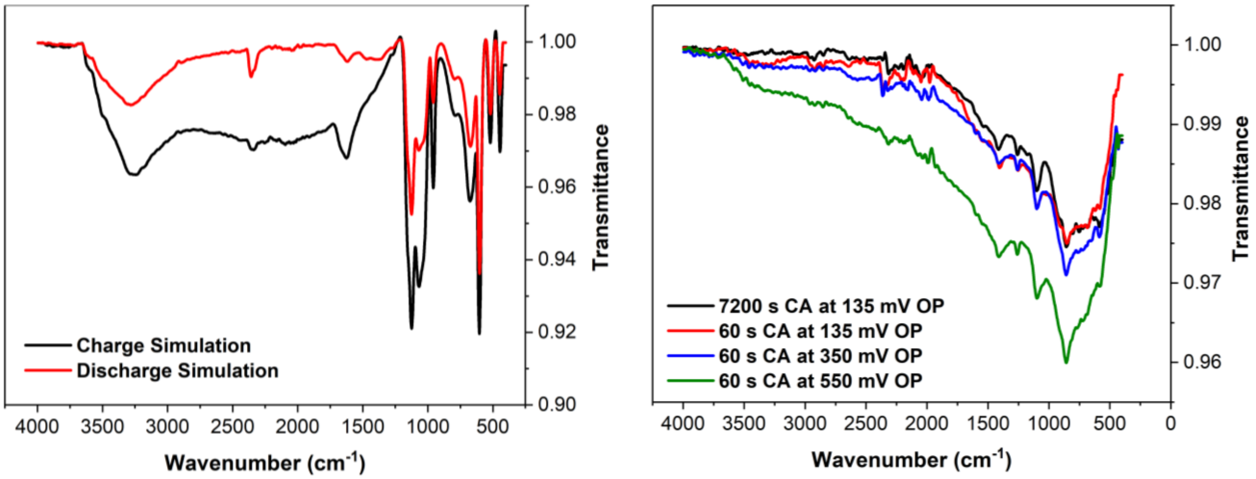

Figure 31: FTIR of zinc electrodes after exposure to charge-discharge simulation using CV (left), and chronoamperometry at different overpotentials (right) 1 vol.% PEG200 electrolyte

Secondly, FTIR was conducted on zinc electrodes which had been exposed to chronoamperometry at -135 mV, -350 mV, and -550 mV (all potentials vs. open circuit potential) to examine if there exists a correlation between applied potential and the amount of adsorption of PEG. As seen in Figure 31 (right), increasing the overpotential from -135 mV to -350 mV to -550 mV led to a sharp decrease in the transmittance demonstrating that the adsorption of PEG during chronoamperometry is an activation-controlled process.[72] There is no notable difference when the chronoamperometry duration is increased from 60 s to 7200 s suggesting that the amount of PEG adsorption on the surface remains constant.

Lastly, FTIR was conducted on zinc anodes after cycles of charge and discharge in a small cell. The cells were first cycled using the CC-CV protocol with a current density equivalent to 1 C. Similar to the trend observed in the charge-discharge simulation via cyclic voltammetry, a larger decrease in transmittance intensity was observed during the charging step (from CC-CV) than in the discharge. This reaffirms prior observations where PEG was found to adsorb to the anode during charging and subsequently desorbed when the polarity of the electrode was reversed (i.e. during the discharge). After 50 cycles of CC-CV, a similar trend is observed where the charging step once again has a lower transmittance than the discharge. An important observation is that both charge and discharge spectra at 50 cycles show lower transmittance than their counterparts after the first cycle. This suggests that the PEG adsorption-desorption mechanism is not fully reversible, and eventually there will be some accumulation on the anode as the cell cycles.

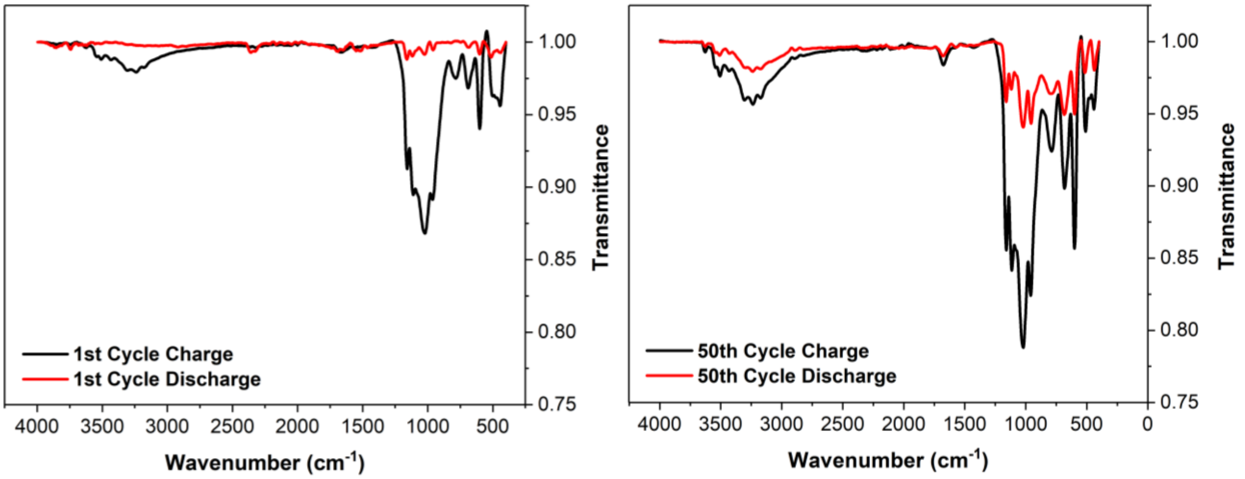

Figure 32: FTIR of zinc anodes after charge-discharge cycles: 1 cycle (left), and 50 cycles (right)

3.2.4 Surface Composition, Morphology and Crystal Structure

X-Ray Photoelectron Spectroscopy (XPS)

XPS was invoked to investigate the composition of dendrites grown on the zinc electrode in 1 vol.% PEG200 and control electrolytes. A full spectrum and high-resolution scans of the Zn 2p (3/2) peaks from both samples are shown in Figure 33. Using a Lorentz-Gauss deconvolution algorithm, the Zn 2p (3/2) peaks are composed of three different zinc types: pure zinc metal (Zn, 1020.2 eV), zinc oxide (ZnO, 1021.5 eV), and zinc hydroxide ($Zn(OH)_2$, 1022.5 eV). While the ZnO content on the two samples is relatively similar, the 1 vol.% PEG200 sample distinctly exhibits a higher content of pure zinc metal (18% vs. 7%) than the control. This result confirms more efficient deposition of Zn ions when PEG is used as an additive in the electrolyte.

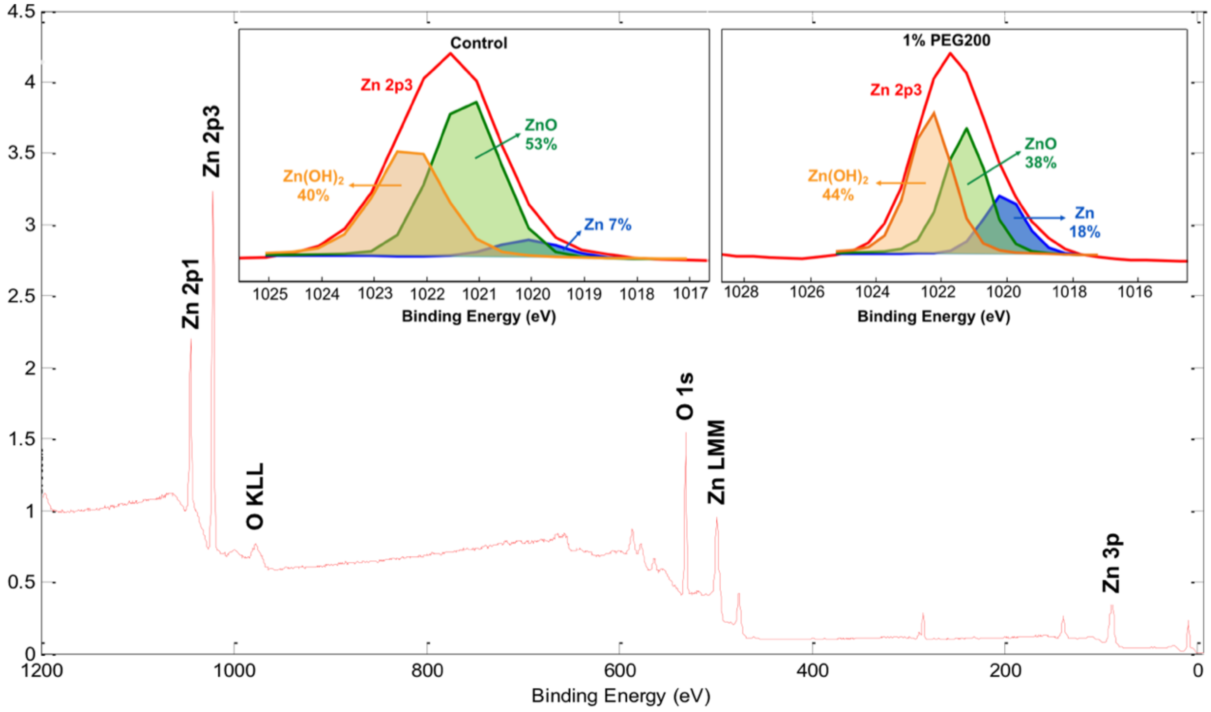

Figure 33: Full XPS on zinc electrode after CA. Insets: high resolution Zn 2p (3/2) on zinc electrode after 1 h CA in control (left) and 1 vol.% PEG200 (right) electrolytes

Electron Microscopy

Zinc electrodes were studied using Scanning Electron Microscopy (SEM) to analyze the differences in morphology that are induced PEG polymers during zinc ion reduction. Dendrites were first grown on the electrodes using chronoamperometry at -135 mV overpotential in the 1 vol.% PEG200 and control electrolytes. Figure 34 shows SEM micrographs of the electrodes at the 0.17 s, 9 s, 30 s, 100 s, 500 s, and 3600 s intervals of the chronoamperometry process.

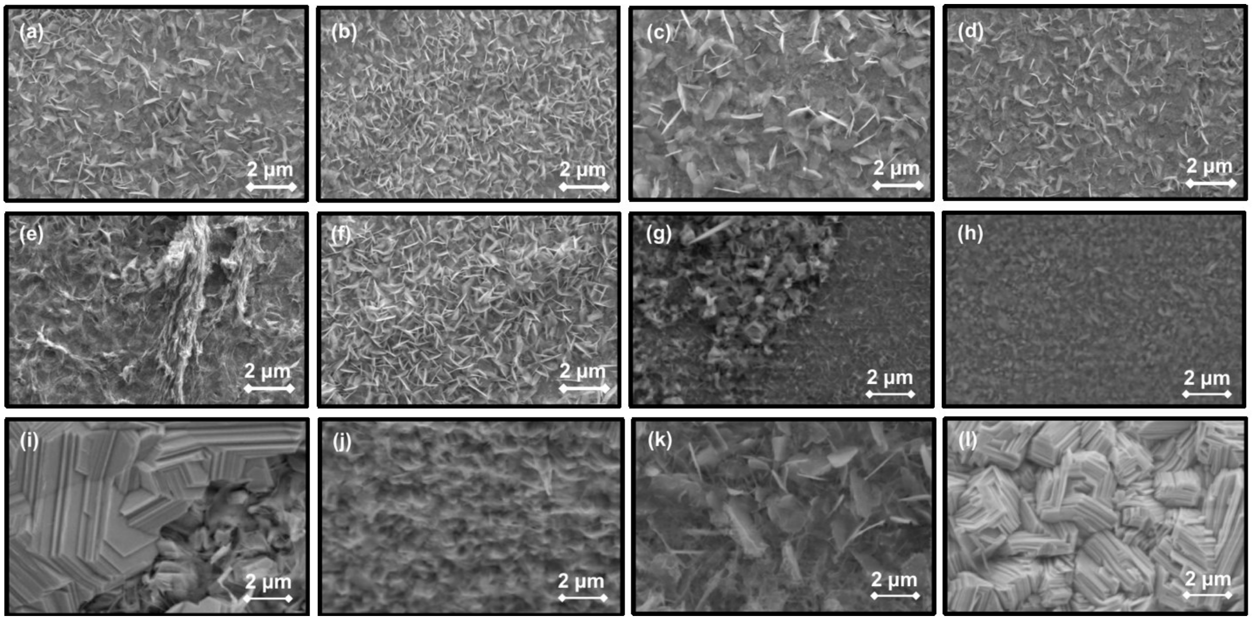

Figure 34: SEM of zinc electrodes after exposure to 1 h CA at -135 mV overpotential vs. OCV for: 0.17 s in (a) control electrolyte and (b) 1 vol.% PEG200 electrolyte, 9 s in (c) control electrolyte and (d) 1 vol.% PEG200 electrolyte, 30 s in (e) control electrolyte and (f) 1 vol.% PEG200 electrolyte, 100 s in (g) control electrolyte and (h) 1 vol.% PEG200 electrolyte, 500 s in (i) control electrolyte and (j) 1 vol.% PEG200 electrolyte, and 3600 s in (k) control electrolyte and (l) 1 vol.% PEG200 electrolyte

Initially, even after just 170 ms of exposure, primary flake-type dendrites are easily visible on the electrode surfaces, in these cases projecting perpendicular to the electrode surface (i.e. towards the observer). The key difference is that while the 1 vol.% PEG200 sample shows a higher number of small dendrites, the dendrites in the control sample are much larger and occur at greater separation distances. At the 9 s interval, this trend is more pronounced with dendrites in the control sample showing significant increase in size over the 1 vol.% PEG200 sample. At 30 s, the dendrites on the control sample begin to convert to secondary dendritic features, in this case forming 'mossy' growth with less primary flake-types dendrites present.[108] However, it is important to note the 1 vol.% PEG200 sample is still in the primary dendrite phase. At 100 s, the control sample converts to boulder-type dendrites with a large size distribution, while the 1 vol.% PEG200 sample still shows a majority of flake-type dendrites with the beginnings of secondary dendrite formation.[115]

The control sample at 500 s shows only secondary dendrite features with the surface being dominated by boulder-type dendrites. The size distribution ranges from approximately 500 nm to over 50 µm signifying very uneven nucleation and growth. The 1 vol.% PEG200 sample at this time shows uniform boulder-type dendrite growth. After 1 h of chronoamperometry, the control sample has converted yet again to a different morphology – this time flake-type dendrites again at a much larger size than observed before. In contrast, the 1 vol.% PEG200 has grown densely packed boulder-type dendrites with a very narrow size distribution (approximately 2-5 µm), indicating well-controlled nucleation and growth. This is a common observation noted when using dendrite suppressants such as CTAB.[116]

High-resolution transmission electron microscopy (HRTEM) was conducted on a dendrite particle grown in 1 vol.% PEG200 electrolyte and has been shown in Figure 35 (left). Some of the common zinc crystalline planes such as (002), (100), (101), and (102) can be observed on the sample. Elemental mapping was conducted using the scanning mode of the TEM instrument (STEM) via electron energy loss spectroscopy (EELS) on dendrite particles grown in 1 vol.% PEG200 and control electrolytes, and are shown in Figure 35 (right). In both samples, the maps of Zn and O can be overlaid over each other signifying that the oxygen atoms are bonded to zinc (i.e. a compound). The 1 vol.% PEG200 sample shows much more ZnO than the control, a finding in good agreement with other bulk characterization methods. Note that XPS results which show a higher prevalence of pure zinc in the 1 vol.% PEG200 sample are focused specifically on the top surface layer of the electrode.

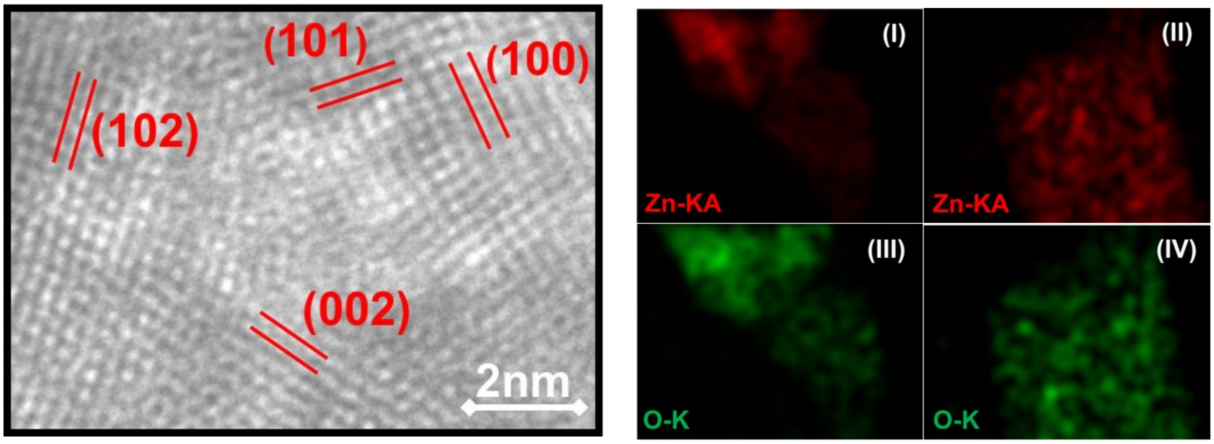

Figure 35: Left: HRTEM micrograph of zinc dendrite grown in 1 vol.% PEG200 electrolyte for 1 h. Right: STEM EELS elemental mapping of (I) Zn (red) and (II) O (green) on a dendrite grown in control electrolyte, and of (III) Zn (red) and (IV) O (green) of a dendrite grown in 1 vol.% PEG200 electrolyte

X-Ray Diffraction (XRD)

The crystal structure of different zinc deposits depends significantly on electroplating conditions.[117] Specifically, growth on the surface can occur in different crystalline planes, each with distinct surface energy and direction of growth. XRD was used in this study to analyze the crystallinity of zinc electrodes after exposure to chronoamperometry for 1 h (to ensure comprehensive dendrite growth on the surface), and the resulting profiles have been normalized versus the (101) peak and presented in Figure 36 (left). The after-chronoamperometry samples are all highly crystalline and exhibit no significant shift compared to the peaks of the pristine zinc foil sample. The main observation is the difference in peak intensity for the different crystalline planes – a result of changing surface energy when PEG is introduced into the electrolyte. Generally, the lowest energy planes experience the most growth since they are most energetically favorable.[117] In the control sample the (002) basal plane shows more growth than the (100) plane due to its lower energy and compactness.[118,119] However, with the addition of 1 vol.% PEG200 to the electrolyte, the growth of the basal plane is significantly lower than that of the (1 0 0) plane, giving evidence to the ability of PEG polymers to disrupt the electrodeposition process.

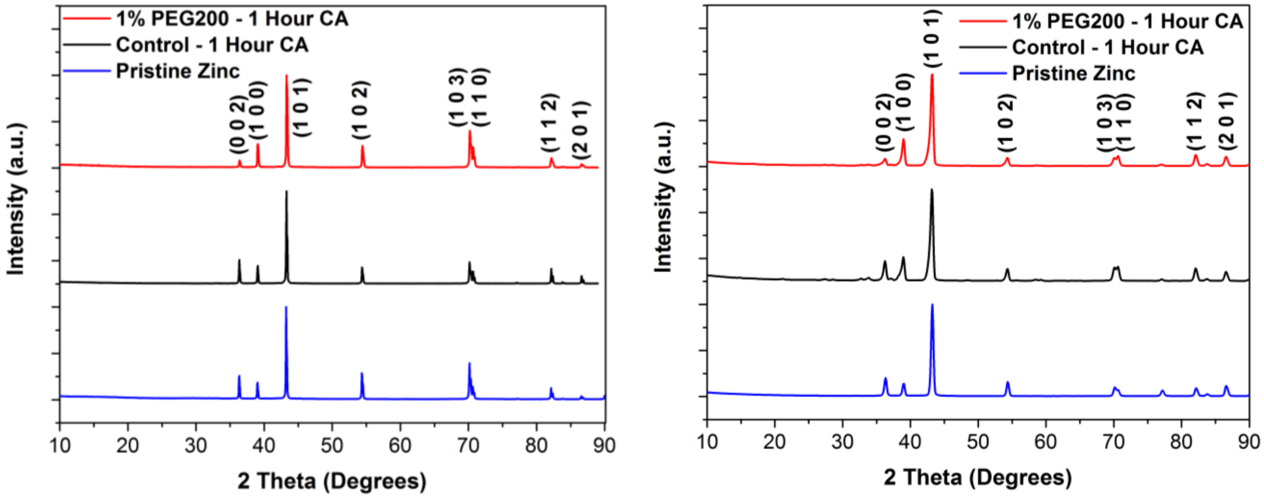

Figure 36: XRD (left) and GIXRD (right) of zinc electrodes after exposure to CA in 1 vol.% PEG200 and control electrolytes

Growth along the (110) crystalline plane is also preferred in the PEG after-CA sample (relative intensity of 22.147 a.u.) than in the control after-CA (relative intensity of 13.355 a.u.) and pristine zinc foil (relative intensity of 14.098 a.u.) samples. As before, this is attributed to the change in surface energy caused by PEG polymers leading to lesser discharge of zinc ions.[116] Overall, the change in crystallinity of the zinc electrode surface points to the ability PEG polymers to affect deposition of ions and inhibit certain nucleation and growth mechanisms.

The Scherrer formula was used to determine the average grain sizes in the XRD samples – these were calculated to be 56.40 nm, 63.31 nm, and 59.60 nm, for the 1 vol.% PEG200 after-CA, control after-CA, and pristine zinc foil samples, respectively. The decreased grain size in the PEG sample also proves the ability of PEG to interact with the zinc electrode and modify the surface morphology by influencing the ratio of nucleation to growth.[116]

XRD is known for its deep penetration into samples (approximately 1 mm), and thus Glancing Incidence X-Ray Diffraction (GIXRD) was conducted to obtain a more surface sensitive

XRD profile. The interaction volume of this method is much lower since it has a penetration depth approximately in the micrometer range. GIXRD scan results are shown in Figure 36 (right). The same trend as regular XRD is observed in which the (101) and (110) crystal planes experience more growth while growth along the (002) plane is retarded.

3.2.5 Proposed Interaction Model

A mechanism is proposed to describe the interaction between PEG polymers in the aqueous electrolyte and the zinc electrode based on the results of the electrochemical, spectroscopy and electron microscopy testing. The mechanism is defined only for the cation reduction step (i.e. zinc deposition) as this was the step in which the main effect of PEG was experienced. A graphic illustrating this process has been presented in Figure 37.

Control Electrolyte

In the control electrolyte, with the application of a negative overpotential, zinc ions are attracted from the electrolyte to the electrode surface, as seen in the chronoamperometry testing where an adsorption current of 8.638 $mA \cdot cm^{-2}$ was observed when potential was applied. This attraction and adsorption represent Step 1 in the mechanism, shown in the upper part of Figure 37.[85] Once the ions adsorb, they are able to diffuse unencumbered laterally (designated in the figure by large red arrows parallel to the electrode surface) along the electrode surface to find optimal sites for charge transfer.[120] This diffusion is seen in the higher 2D diffusion current during short chronoamperometry as well as a larger diffusion coefficient of 5.635E-11 $cm^2 \cdot s^{-1}$ from EIS measurement. In this system, there is no barrier to diffusion and thus the newly adsorbed ions are very likely to migrate toward each other and deposit in very close vicinity in order to minimize the overall surface area exposed to the electrolyte, as per nucleation and growth theory. This represents Step 2 of the mechanism. The key characteristic of this system is formation of few, widely spaced, and large nucleation sites.

In the third step, a new wave of ions adsorbs to the electrode surface (since the electrode is continuously being biased with a potential). The ions behave in exactly the same manner as those from the previous batch in Step 1, and will diffuse along the surface toward the previously formed nucleation sites at which they will accept electrons and deposit. This is represented as Step 4, and it describes the beginnings of dendrite formation. We note these dendrites even at the earliest time of the chronoamperometry testing – as early as 0.17 s, as seen in the SEM micrographs. Overall, this manner of ion reduction and deposition on the electrode leads to the formation of larger dendrites but at a lower numerical density.

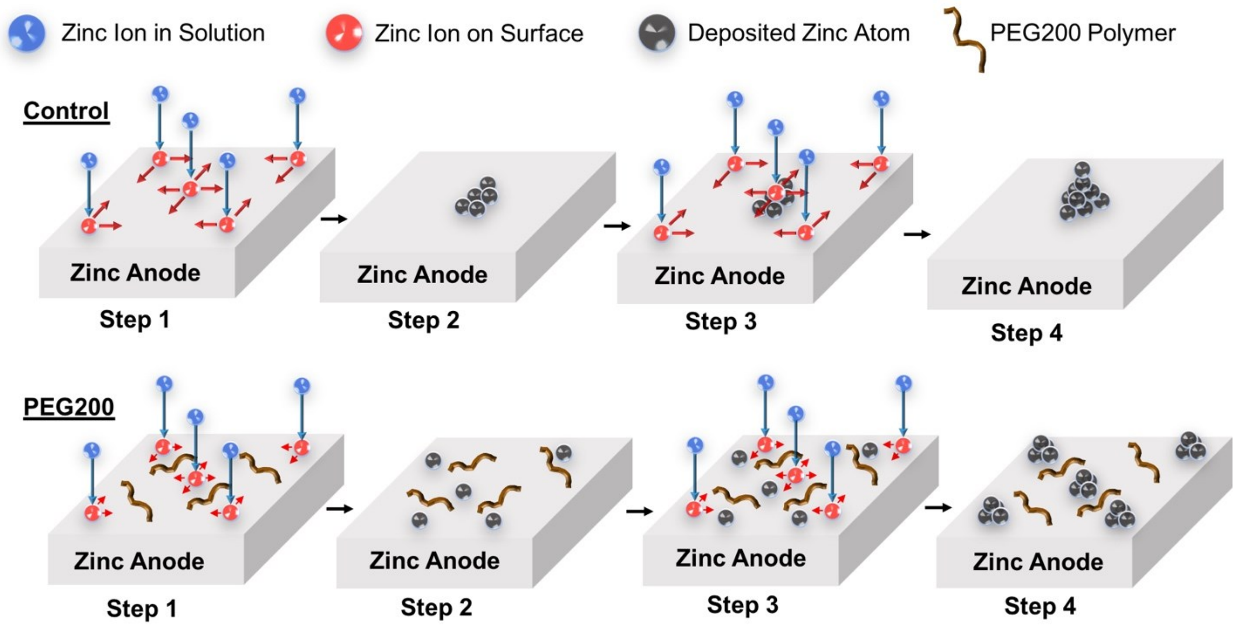

Figure 37: Schematics of step-by-step zinc ion reduction on the surface of the anode in the control (upper), and 1 vol.% PEG200 (lower) electrolytes

1 vol.% PEG200 Electrolyte

The addition of PEG polymers to the electrolyte causes slight changes in the mechanism. During Step 1, as the overpotential is applied, PEG polymers are also attracted from the electrolyte to the electrode surface together with zinc ions. The physical adsorption of the polymers occurs at preferential nucleation sites on the surface.[121,122] The adsorption is confirmed through FTIR of zinc electrodes first exposed to chronoamperometry which exhibit vibration bands at 1400 cm^{-1}, 1160 cm^{-1}, 1100 cm^{-1}, 1060 cm^{-1}, and 966 cm^{-1}, matching PEG. By occupying nucleation sites, PEG decrease the amount of zinc ion adsorption in the first wave, as seen in the lower chronoamperometry current of just 3.985 mA·cm^{-2}.[123] Secondly, the PEG polymers act as physical barriers to impede lateral diffusion of the adsorbed ions on the surface (as indicated in the figure by smaller red arrows). Lower diffusion is a consequence of both: (1) physical PEG adsorption on the surface, as well as (2) PEG-Zn complexes formed in the electrolyte which significantly decrease the mobility of zinc ions.[124–126] This is corroborated by lower 2D diffusion current from the short chronoamperometry as well as a reduced diffusion coefficient of 3.745E-11 cm^2·s^{-1} from EIS. The adsorbed ions are hence forced to deposit in a very close vicinity to where the original adsorption site, forming more numerous but smaller nucleation sites in Step 2.

In Step 3, the next chronological batch of zinc ions is attracted to the surface. Their surface diffusion is hindered by the PEG polymers, and in order to minimize overall surface energy they deposit at the nucleation sites formed in Step 1. This represents Step 4 in the mechanism, and it features a large number of small dendrites. This is evident in the SEM micrographs of after-CA 1 vol.% PEG200 samples from 0.17 s to 30 s which all display a higher density of dendrites that are more closely spaced together and of smaller size than the control sample.

While performing FTIR on zinc anodes after 50 charge-discharge cycles a residual amount of PEG was observed on the surface even after the discharge step (when the PEG is expected to fully desorb). This implies the adsorption-desorption mechanism is not fully reversible, and an accumulation of PEG on the anode surface is expected in the long term.

3.3 Section Conclusions

The goal of this project was successfully met as the electrochemical performance of ReHABs was significantly improved, particularly in terms of improved cycling life, corrosion resistance, and dendrite suppression. When applied in the bespoke large 7 mAh cell, the 1 vol.% PEG200 sample was able to achieve a discharge capacity of 111.72 $mAh \cdot g^{-1}$, 3% higher than the control sample. Similarly, while accelerating cell failure (by prior exposure of the zinc anodes to chronoamperometry) the 1 vol.% PEG200 samples were able to easily reach 1000 charge-discharge cycles with very comparable discharge capacities and retention to before-CA samples, while control after-CA samples began failing at just 190 cycles. In this manner, the PEG additive was able to improve the utility of lithium at least five times, an important consideration in modern battery systems with the rapidly inflating cost of lithium. Other notable results were four-fold improvements to the corrosion and dendrite resistance of these batteries. These results show significant potential for ReHABs to be applied to large energy storage systems.

Through an in-depth study of the role played by PEG in performance improvement using a variety of electrochemical, spectroscopy and microscopy techniques, a highly specific interaction model was proposed to explain the interaction mechanism between PEG polymers and the zinc anode during the charging step of the cell. It was hypothesized that by adsorbing to preferential nucleation sites on the surface PEG polymers force zinc ions to deposit in recessed positions on the anode leading to an overall flatter morphology of the electrode. This, coupled with restricted 2D diffusion, leads to the formation of many small dendrites in close proximity to each other. Smaller and more uniform dendrites are far less likely to be able to cause internal short-circuits and consequently battery longevity is greatly improved. The adsorption-desorption mechanism allows the PEG polymers to be recycled during regular battery cycling and therefore do not diminish in effect very quickly. This is also an important consideration as it allows the battery to remain a closed system without need for replenishment of the additive.

Overall, the remarkable amelioration of battery performance, reliability, and functional lifespan is highly important at this time since a global shortage of lithium compels products to have more efficient utilization of resources in order to be economically competitive. This project has highlighted substantial merits of using PEG200 as an electrolyte additive for large aqueous metal ion batteries, and as a result, how they can be made into more suitable contenders for energy capture and storage from renewable energy sources.

4.0 Polyethylene Glycol Additive in Thixotropic Gel Electrolyte for the ReHAB System

4.1 Section Introduction

A gel is a colloidal system in which fine solid particles are dissolved in a liquid.[127] The dispersed particles are often designed to form an interlinked network such that the structure of the liquid is made more rigid. The gelator material can range from supramolecules to polymers, and the network they form binds water molecules to give the gel a more rigid physical structure.[128] The ratio of the liquid to the colloidal dispersant can be tuned to obtain different properties in the gel.[129] Thixotropy is a property used to describe the 3D structure of a gel. A gel with a high concentration of hydroxyl ions is more thixotropic since it will have more hydrogen bonding with water and thus will experience a shorter time before the 3D network begins to form.[130]

While gels have a wide range of uses, they are of particular interest in electrochemical systems such as batteries due to benefits they can offer over both liquid and solid electrolytes. They are able to reduce corrosion, electrolyte leakage, and packaging problems posed by liquid electrolytes, and have much higher ionic conductivities (1E-3 $S{\cdot}cm^{-1}$ vs 1E-8 $S{\cdot}cm^{-1}$) than solid-state electrolytes.[131] The ionic conductivity is lower than for liquid electrolytes and allows ion flow at the electrode-electrolyte to be more controllable. Fumed silica gel electrolytes in particular can expand the operating range of aqueous battery systems since they can retard freezing and boiling of water in the electrolyte.[132] Fumed silica has also been used as a dopant in gel electrolytes to achieve a more amorphous structure, increase porosity of the gel membrane and improve the pore distribution and interconnectedness.[133,134]

In this project a novel gel electrolyte is designed for the ReHAB system. The gel electrolyte is a derivation of the control electrolyte from the previous chapter (1M Li_2SO_4 and 2M $ZnSO_4$, and adjusted to pH 4). Fumed silica is inserted as the thixotropic gelling agent and is used to control structure and viscosity. Polyethylene glycol (MW = 300 $g \cdot mol^{-1}$) is added as a corrosion inhibitor and dendrite suppressant. This was based on the successful use of PEG200 as an additive to the liquid electrolyte in the previous project (See Chapter 3). The fumed silica gel electrolyte has the added benefit of being able to maintain a high zinc ion concentration in a smaller volume and can thus improve the overall energy density of the battery.

4.2 Results and Discussion

4.2.1 Electrochemical Characterization

Corrosion

Corrosion of the zinc anode was measured in different formulations of the gel electrolyte using the Tafel extrapolation method (see Section 2.1), and the results are presented in Figure 38 and Table 2. The corrosion measurement was improved from the previous project and was performed over a longer duration at a scan rate of 0.01 mV·s^{-1}. It can be noted that 5% FS alone in fact had poorer corrosion performance (0.0073 V and 2.571 µA·cm^{-2} lesser corrosion potential and higher current density, respectively) than the control electrolyte. This trend has previously been noted in literature.[135] The problem is immediately alleviated with the addition of PEG300 additive to the electrolyte. A positive correlation is noted between the concentration of PEG300 in the gel electrolyte and the corrosion performance. In this respect, the 4% FS + 1% PEG300 and 3% FS + 2% PEG300 both exhibit a corrosion potential of approximately 1.0021 V corresponding to 0.0045 V and 0.0118 V improvements on the control and 5% FS electrolytes, respectively.

Additionally, the corrosion rate is considerably lessened with PEG300, with concentrations of 1% and 2% having corrosion current densities of 5.980 µA·cm^{-2} (45% lower than 5% FS electrolyte) and 4.952 µA·cm^{-2} (54% lower than 5% FS electrolyte), respectively. In this manner, PEG300 offers a much more environmentally friendly method to suppress corrosion compared to traditional means such as lead (Pb^{2+}) ions which tend to be toxic.[136] As identified previously, decreased corrosion will improve the shelf-life of the battery (through lesser parasitic reactions) and decrease hydrogen gas evolution.[135]

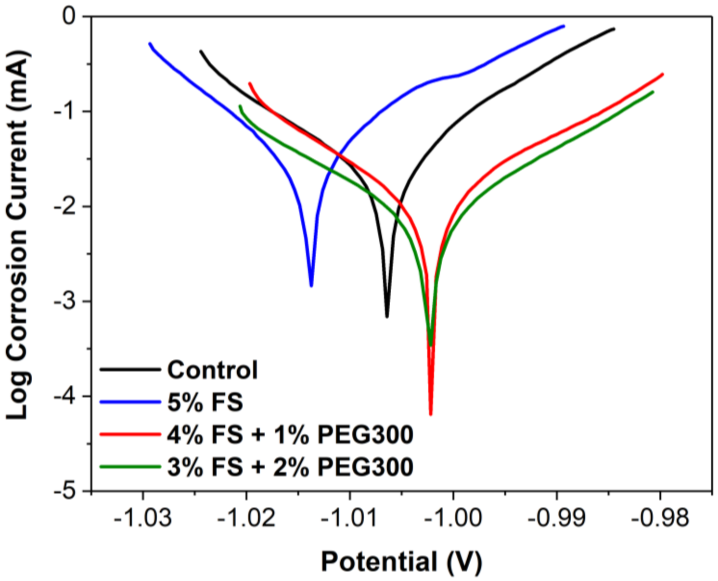

Figure 38: Linear polarization of zinc electrodes in the different electrolytes

Table 2: Corrosion performance of zinc anodes in different electrolyte formulations

Electrolyte	Corrosion Potential [V] vs. SCE	Corrosion Current Density [μAcm^{-2}]
Control	-1.0066	8.237
5% FS	-1.0139	10.808
4% FS + 1% PEG300	-1.0020	5.980
3% FS + 2% PEG300	-1.0021	4.952

Zinc anodes of large batteries were also imaged after 1000 charge-discharge cycles to examine the long-term impact of corrosion on the zinc anode. Figure 39 shows SEM micrographs of zinc anodes from large batteries post cycling in (a) control, and (b) 4% FS + 1% PEG300 electrolytes. In the control electrolyte sample, a large hole is clearly visible in the electrode (approximately 600 μm across). In contrast, the electrode from the PEG gel electrolyte is fully intact at this scale with no visible corrosion damage. The digital images of the same samples shown in Figure 39 (c) and (d), respectively, show the same trend. A large hole is visible in the sample from the control electrolyte approximately 1.5 cm across where zinc was entirely consumed. The

PEG gel sample is completely solid with no holes and only shows coverage from glass fibers from the AGM separator. Physically this sample was also more structurally robust than the control electrolyte anode which felt weak and fragile.

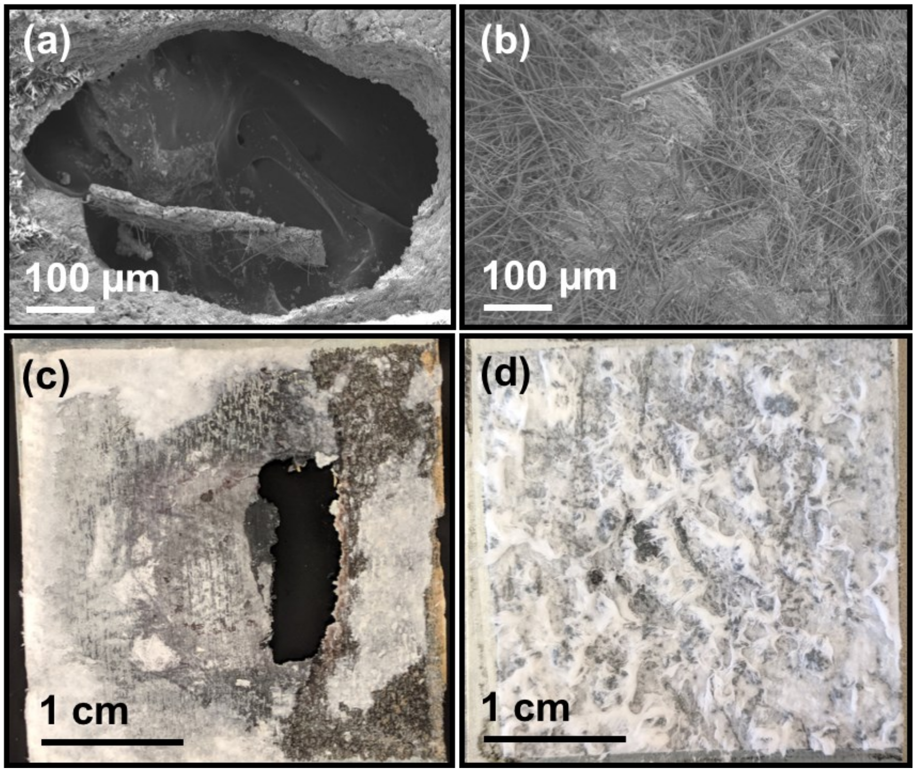

Figure 39: SEM micrographs and digital images of zinc anodes from large batteries post cycling in (a, c) Control, and (b, d) 4% FS + 1% PEG300 electrolytes

Chronoamperometry

Resistance to dendrite formation was measured using the chronoamperometry technique applied for one-hour deposition sessions at -120 mV overpotential vs. OCP (see Section 2.2). The results of this testing are summarized in Figure 40. It is immediately evident that in the control electrolyte there is an uncontrolled growth of zinc dendrites, evident in the constantly increasing value of absolute current density. This trend is due to increasing surface area on the zinc electrode caused by growth of high aspect-ratio features (i.e. dendrites). The 5% FS electrolyte shows great improvement in the trend of the current density over the course of the measurement, and while it experiences a high absolute current density in the medium-term, the absolute current density in the long-term shrinks significantly (6.35 mA·cm^{-2} after 1 hour) indicating decrease in electrode surface area. This result points to a much flatter surface than in the control electrolyte.[137]

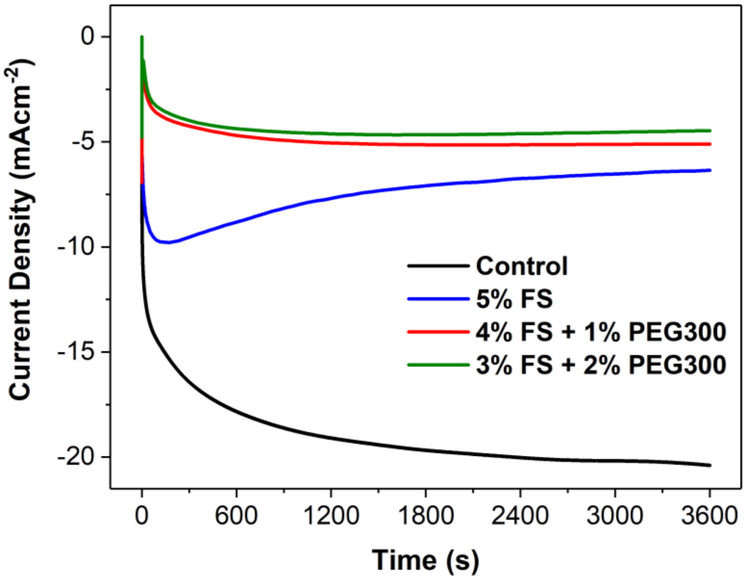

Figure 40: 1-hour chronoamperometry of zinc electrodes in the different electrolytes

When PEG300 is added to the electrolyte, the nucleation, 2D and 3D diffusion currents are significantly decreased than before, as seen in Figure 40. This indicates inhibition of the reduction, surface diffusion, and deposition processes on the zinc electrode, caused by the PEG additive. This is similar to the previously-noted results obtained with PEG200 additive (see Section 3.2.1). The growth profile of the dendrites is quite well-controlled and no runaway growth is observed over the duration of the test (as noted by the flat 3D diffusion current profile in the long-term). Increasing the concentration of PEG300 from 1% to 2% in the electrolyte has the effect of reducing the absolute current density associated with the deposition process (5.10 mA·cm^{-2} vs. 4.47 mA·cm^{-2}). This corresponds to greater inhibition of the nucleation and growth processes and results in more uniformity in surface morphology.

Figure 41 shows SEM micrographs of zinc electrodes after the chronoamperometry test in the different electrolyte formulations. In the absence of fumed silica, very large and jagged boulder-type dendritic features are noted on the surface of the electrode, reaching hundreds of micrometers in size. In contrast, when 5% fumed silica is added to the electrolyte, the surface of the electrode becomes more uniform and condensed. There are also much fewer jagged protrusions which confirms the chronoamperometry result in which long-term 3D diffusion current showed a decrease in absolute value. The addition of PEG300 to the gel electrolyte results in a completely different surface morphology, flake-type dendrites are observed instead of boulder-type dendrites. Overall, the size of surface features is greatly reduced than before, with dendrites in the sub-micrometer range. Increasing the concentration of the PEG additive from 1% to 2% results in a decrease in the size of the dendrites and an increase in their numerical density. This is perfectly in line with the current density trend, and is similar to the observations from the PEG200 study. On the basis of these observations, it can be concluded that zinc ions in the gelled electrolytes with PEG300 additive follow the same surface adsorption and deposition mechanism derived in the previous study (see Section 3.2.5).

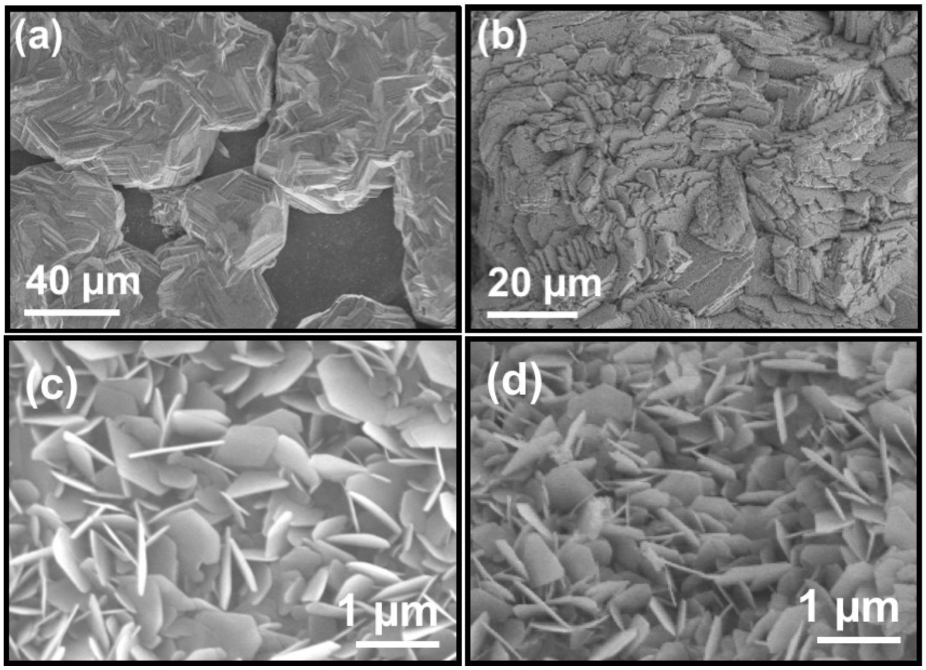

Figure 41: SEM images of zinc electrodes after chronoamperometry in (a) Control, (b) 5% FS, (c) 4% FS + 1% PEG300, and (d) 3% FS + 2% PEG300 electrolytes

4.2.2 Battery Performance

Cycle life testing was performed on the different gelled electrolytes to measure their impact on battery performance. The cyclability test was conducted using the CC-CV protocol between 1.4 and 2.1 V at 1 C equivalent current with 0.1 C current cut-off. Figure 42 summarizes the cycling test results from Swagelok cells. The control system is able to perform relatively well and achieves an end-of-test capacity retention of 59%. In comparison, the 5% FS, 4% FS + 1% PEG300, and 3% FS + 2% PEG300 systems can achieve capacity retentions of 69%, 72%, and 69%, respectively. Not only are the gelled electrolytes able to improve performance, their cycling trends are also much more uniform and do not experience the large capacity fluctuations noted in the control system, likely caused by excessive side reactions.

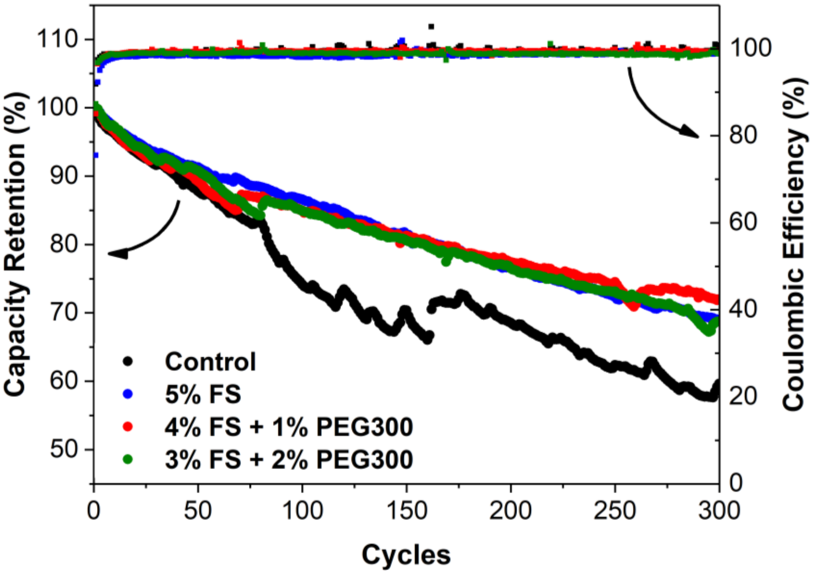

Figure 42: Cycling performance of ReHAB Swagelok cells containing different electrolytes

In the large battery system, the control electrolyte was compared to the best-performing gel from the Swagelok system – the 4% FS + 1% PEG300 electrolyte. These results are presented in Figure 43. At the initial cycle, the control electrolyte achieves a discharge capacity of 114.00 mAh·g^{-1} while the gel attains 141.00 mAh·g^{-1}. After 1000 cycles, the control system can only retain 15% of initial capacity, a 39% decrease compared to the gel system. Also of note is the rapid decline in discharge capacity observed in the control system after 730 cycles. The coulombic efficiency is also seen to rapidly fluctuate during this period indicating a high degree of parasitic losses. Based on previous experience as well as observations made in Figure 39, this decline is attributed to excessive corrosion. As this process consumes zinc from the anode, there is less active material available to facilitate complete intercalation and deintercalation of lithium ions at the cathode, resulting in capacity loss over successive cycles.

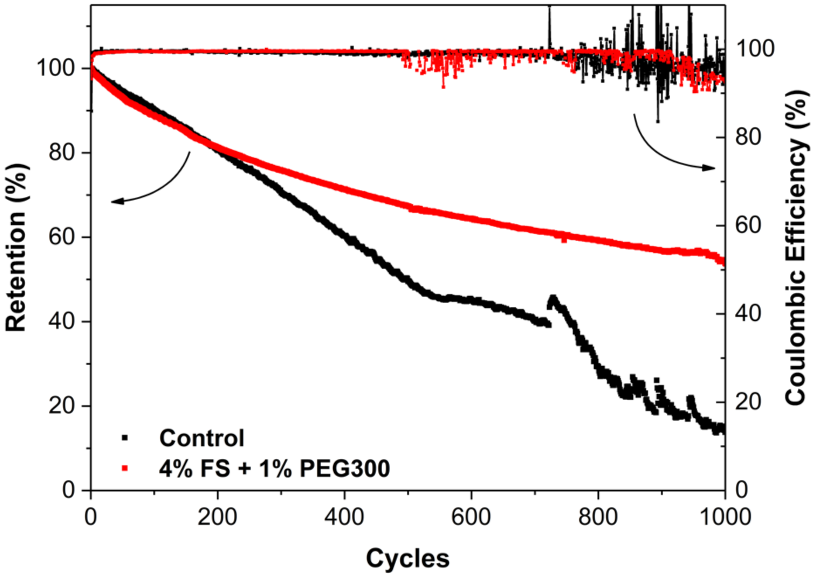

Figure 43: Cycling performance of ReHAB large battery system

Charge-discharge profiles of the 1st, 500th, and 1000th cycles for large battery systems are graphed in Figure 44. There exist two plateaus (at approximately 1.850 V and 1.725 V, both vs. Zn/Zn^{2+}) which correspond to the two-step Li^+ intercalation and deintercalation mechanisms in spinel $LiMn_2O_4$.[138–140] The similarity in the locations of these plateaus between the two electrolytes indicates that the gel does not interfere with the insertion and deinsertion processes of lithium at the cathode. The major difference of note is the significant capacity retention of the gel system between the 500th and the 1000th cycles (approximately 90%) while the control electrolyte system can only retain 42% capacity in the same period. This demonstrates that the added benefit of the gel is more manifest during extended cycling.

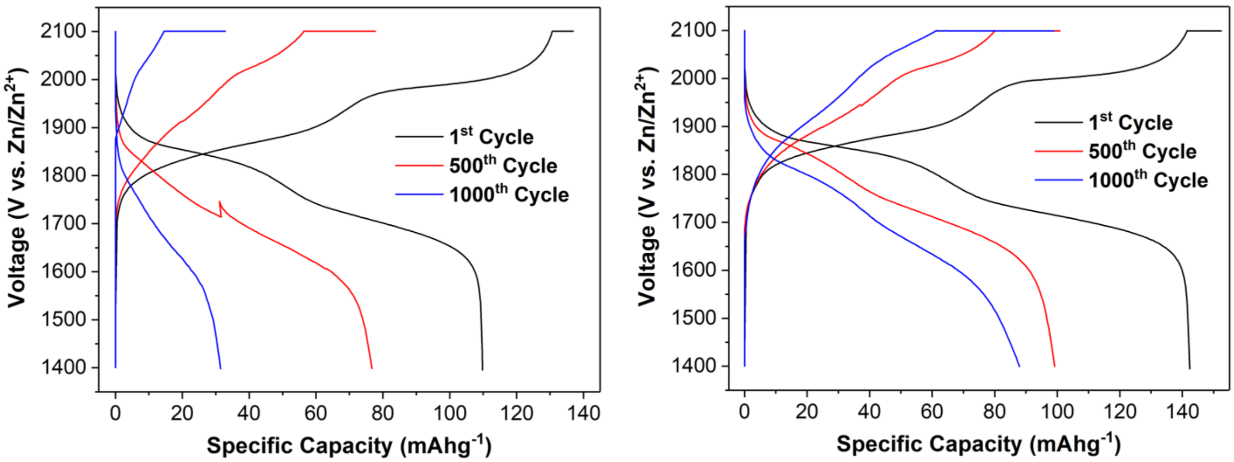

Figure 44: Charge-discharge curves of ReHAB large batteries containing control (left) and 4% FS + 1% PEG300 (right) electrolytes

Additional characterization of large battery electrodes from both electrolytes was carried out at the end of the cycling test, shown in Figure 45. Both the anodes show layered type zinc deposition, however, on the anode from the control electrolyte, growth features are much larger (approximately 8-10 µm vs. 2-3 µm in the gel), and are prevalent much more perpendicularly to the electrode plane (as shown inside the red circles). The larger deposit sizes and angles of protrusion from the surface significantly increase surface area available on the electrode. This increases the rate of surface sensitive reactions such as corrosion, and can thus be linked to the rapidly declining discharge capacity of the control battery system.

The SEM micrographs of the cathodes (Figure 45 c and d) show LMO particles connected by graphitic sheets. There is no significant variation in the morphology of the two cathodes indicating that neither the fumed silica gel nor the PEG300 additive have any interaction with cathode processes. Instead their contributions to various characteristics of the battery are focused solely on the zinc anode.

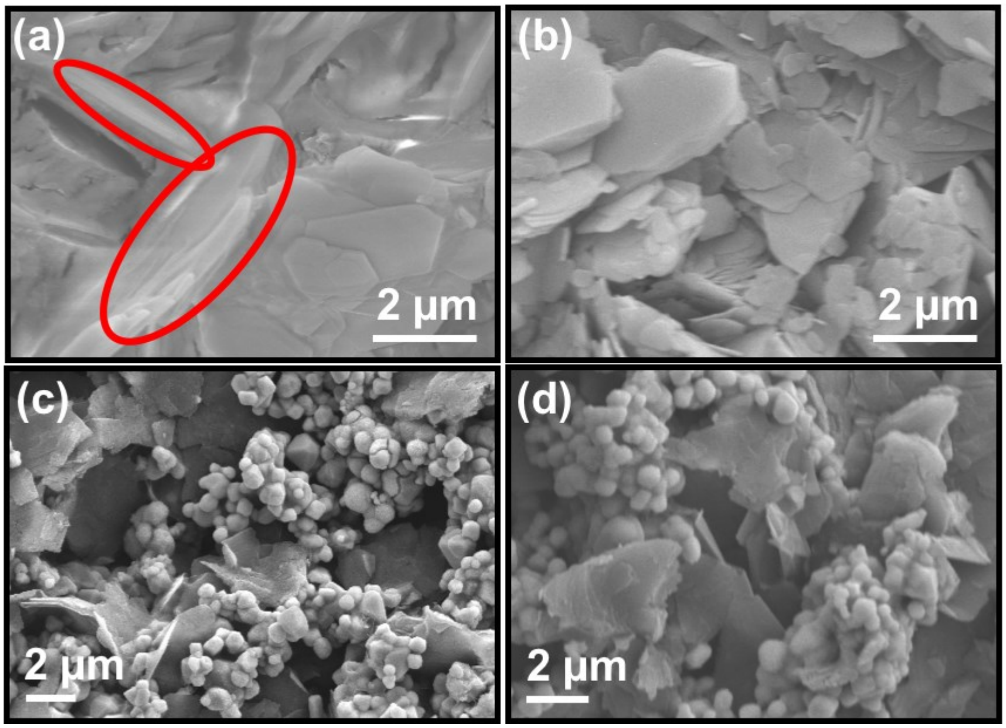

Figure 45: SEM micrographs of large battery anodes from (a) Control, and (b) 4% FS + 1% PEG300 electrolytes, and cathodes from (c) Control, and (d) 4% FS + 1% PEG300 electrolytes

4.3 Section Conclusions

The primary focus of this research project of developing a suitable gel electrolyte for the ReHAB system was successfully accomplished. A novel fumed-silica based gel electrolyte was prepared in which fumed silica was the primary gelling agent. A PEG additive was also integrated into the gel electrolyte to improve gelation and dendrite resistance as well as suppress excessive corrosion commonly noted in similar electrolytes. Chronoamperometry and SEM studies corroborate inhibition of dendrite formation on the zinc anode. PEG300 is also able to decrease the corrosion rate of the zinc anode by 27-40% compared to the control electrolyte. Further, it was found that in the absence of the PEG additive in the large battery, the zinc anode was severely consumed by corrosion processes. Hence the PEG-FS gel electrolyte can greatly improve the useful life of the ReHAB system.

Additionally, cycling performance of the ReHAB is also improved with gel electrolyte and PEG300 additive. 12% and 39% improvements in capacity retention at 300 and 1000 cycles, respectively, were observed in Swagelok and large batteries using 4% FS + 1% PEG300 electrolyte. The charge-discharge curves of the large batteries showed that the largest contribution of the PEG-FS gel electrolyte was observed in the latter 500 cycles during which the battery was able to retain 90% of its capacity while the control battery could only retain 42%. The vastly lower capacity fading in the gel electrolyte makes it a viable alternative to liquid electrolyte for large scale applications of the ReHAB system since it will have a much longer cycling life as well as be able to offer higher reliability in the long term.

The ability of PEG300 to markedly improve the performance of both the fumed silica gel electrolyte and the ReHAB as a whole reinforces the argument for using polyethylene glycol in aqueous batteries. It has been observed to not only help improve discharge capacity in cells but to also retard the degradation of the zinc anode from excessive corrosion and dendrite growth. Owing to its low cost, resistance to breakdown in different conditions, and facile integration into aqueous electrolytes, it is an additive that must be considered for large-scale and long-term closed energy storage systems.

5.0 Summary and Conclusions

Polyethylene glycol was investigated as an electrolyte additive for aqueous metal ion batteries, specifically using the ReHAB system as a pilot project to fully understand the mechanisms involved during battery operation. When applied in the liquid-based aqueous electrolyte, 1 vol.% PEG200 was able to improve discharge capacity of bespoke large (7 mAh) cells by approximately 3% during a 100-cycle test at 1 C, with the trend indicating that the difference in capacity retention between the two electrolytes will continue to increase. It made further improvements to corrosion and dendrite suppression in this system resulting in a far more efficient utilization of lithium material in the cathode.

A novel gel electrolyte was also developed for the ReHAB system with the aim of improving long term reliability as well as simplifying manufacturing and packaging of the cells. An amorphous fumed silica dispersed network forms the base structure of the gel and supports aqueous ions. PEG300 was also added to the system to mitigate the increased corrosion noted in the primary gel. Overall, with the new gel electrolyte the corrosion of the ReHAB system was reduced up to 40%, dendrite growth was retarded 78%, and discharge capacity of batteries was improved by 40% after a 1000-cycle test. An added benefit of the gel electrolyte was its ability to protect the zinc anode from being consumed by the acidic electrolyte.

Advanced characterization methods were used to study the interaction between PEG and the ReHAB system. SEM micrographs showed that PEG affected the size and numerical density of dendrites formed on the zinc surface. As secondary boulder type dendrites are formed, those in the PEG electrolyte have a much more uniform size distribution and a higher packing density than in the control electrolyte. It was found via FTIR analysis that PEG polymers adsorb to the zinc anode surface during the charging step, occupy preferential nucleation sites, and form surface barriers to lateral 2D diffusion of adsorbed ions. They also form PEG-Zn complexes in the electrolyte which significantly limits the mobility of zinc ions. In combination, these processes force zinc ions to deposit in less preferred sites (i.e. valleys and crevices on the surface) thus resulting in a more uniform surface overall. Blockage of nucleation sites on the surface also hinders hydrogen evolution and corrosion reactions. The adsorption mechanism is reversed during the discharge state and this allows PEG to be recycled during regular operation. This is quite significant because a small quantity of PEG can be effective over the entire operating life of the battery.

6.0 Recommendations for Future Work

Based on the experiences and findings of this project, there are several recommendations for future work in this field:

Firstly, a more expanded investigation could be made into the size and structure of PEG polymers. PEG with high degrees of polymerization (i.e. high molecular weight) were omitted from the current project due to their poor solubility in aqueous acidic electrolyte. However, higher molecular weight PEGs could likely be incorporated if further steps are taken to improve solubility, for example by using surfactants or by grafting hydrophilic side groups to the main polymer. This could lead to further improvements in aqueous metal ion battery performance by using techniques such as block copolymerization and branching.

Secondly, the zinc anode could be ameliorated by using a powdered zinc material instead of the planar foil. The powdered structure would increase the electrochemical surface area available for reaction and improve the energy density of the battery. Powdered zinc would also facilitate slurry electrode fabrication which allows corrosion and dendrite inhibitors to be integrated directly into the anode. This may prove to be more effective than electrolytic additives. Slurry fabrication would also open possibilities to use surface coatings to further improve anode performance.

Lastly, gas evolution is one of the most significant processes in aqueous metal ion batteries that is yet to be fully understood. A more in-depth characterization of the types and quantities of gases as well as the specific conditions favorable to their evolution would shed light on the steps required to preserve the electrochemical environment in the cell for longer durations. Decreasing gas evolution would also have the add-on benefit of improving battery safety as it would inhibit excessive pressure buildup in the cell interior and lower the risk of explosion and fire.

References

(1) Arndt, D. S.; Baringer, M. O.; Johnson, M. R. State of the Climate in 2009. *Bull. Am. Meteorol. Soc.* **2010**, *91* (7), s1–s222.

(2) NASA. NASA, NOAA Data Show 2016 Warmest Year on Record Globally https://www.giss.nasa.gov/research/news/20170118/ (accessed Jun 17, 2018).

(3) Levitus, S.; Antonov, J. I.; Boyer, T. P.; Locarnini, R. A.; Garcia, H. E.; Mishonov, A. V. Global Ocean Heat Content 1955-2008 in Light of Recently Revealed Instrumentation Problems. *Geophys. Res. Lett.* **2009**, *36* (7), n/a-n/a.

(4) NSIDC. SOTC: Mountain Glaciers | National Snow and Ice Data Center http://nsidc.org/cryosphere/sotc/glacier_balance.html (accessed Jun 17, 2018).

(5) Kunkel, K. E.; Karl, T. R.; Easterling, D. R.; Redmond, K.; Young, J.; Yin, X.; Hennon, P. Probable Maximum Precipitation and Climate Change. *Geophys. Res. Lett.* **2013**, *40* (7), 1402–1408.

(6) Church, J. A.; White, N. J. A 20th Century Acceleration in Global Sea-level Rise. *Geophys. Res. Lett.* **2006**, *33* (1).

(7) NASA. *Climate Change: How Do We Know?*; 2018.

(8) *Climate Change 2014: Synthesis Report*; 2014.

(9) Natural Resources Canada. About Renewable Energy https://www.nrcan.gc.ca/energy/renewable-electricity/7295 (accessed Jun 17, 2018).

(10) Rüth, C. Sustainable Power Generation https://www.siemens.com/innovation/en/home/pictures-of-the-future/energy-and-efficiency/sustainable-power-generation-neural-networks.html (accessed Jun 18, 2018).

(11) Pancaldi, G. Electricity and Life. Volta's Path to the Battery. *Hist. Stud. Phys. Biol. Sci.* **1990**, *21* (1), 123–160.

(12) Liu, X.; Park, M.; Kim, M. G.; Gupta, S.; Wang, X.; Wu, G.; Cho, J. High-Performance Non-Spinel Cobalt-Manganese Mixed Oxide-Based Bifunctional Electrocatalysts for Rechargeable Zinc-Air Batteries. *Nano Energy* **2015**.

(13) Chan, C.; Peng, H.; Liu, G.; McIlwrath, K.; Zhang, X.; Huggins, R.; Cui, Y. High-Performance Lithium Battery Anodes Using Silicon Nanowires. *Nat. Nanotechnol.* **2007**, *3*, 31.

(14) Qian, J.; Henderson, W. A.; Xu, W.; Bhattacharya, P.; Engelhard, M.; Borodin, O.; Zhang, J.-G. High Rate and Stable Cycling of Lithium Metal Anode. *Nat. Commun.* **2015**, *6* (1), 6362.

(15) Isaacson, M. J.; Daman, M. E.; Hollandsworth, R. P. Li-Ion Batteries for Space Applications. In *IECEC-97 Proceedings of the Thirty-Second Intersociety Energy Conversion Engineering Conference (Cat. No.97CH6203)*; IEEE; Vol. 1, pp 31–34.

(16) Manthiram, A. An Outlook on Lithium Ion Battery Technology. *ACS Cent. Sci.* **2017**, *3*, 1063–1069.

(17) Liu, J.; Hu, J.; Deng, Q.; Mo, J.; Xie, H.; Liu, Z.; Xiong, Y.; Wu, X.; Wu, Y. Aqueous Rechargeable Batteries for Large-Scale Energy Storage. *Isr. J. Chem.* **2015**, *55* (5), 521–536.

(18) Beck, F.; Rüetschi, P. Rechargeable Batteries with Aqueous Electrolytes. *Electrochim. Acta* **2000**, *45* (15–16), 2467–2482.

(19) Wang, Q.; Ping, P.; Zhao, X.; Chu, G.; Sun, J.; Chen, C. Thermal Runaway Caused Fire and Explosion of Lithium Ion Battery. *J. Power Sources* **2012**, *208*, 210–224.

(20) Hu, W.; Zhong, C.; Deng, Y.; Qiao, J.; Zhang, L.; Zhang, J. A Review of Electrolyte Materials and Compositions for Electrochemical Supercapacitors A Review of Electrolyte Materials and Compositions for Electrochemical Supercapacitors. *Chem. Soc. Rev* **2015**, *44*, 7484.

(21) Vincent, C. A.; Scrosati, B. *Modern Batteries : An Introduction to Electrochemical Power Sources*, 2nd ed.; Butterworth Heinemann: Burlington, 1997.

(22) Hu, P.; Zhu, T.; Wang, X.; Wei, X.; Yan, M.; Li, J.; Luo, W.; Yang, W.; Zhang, W.; Zhou, L.; et al. Highly Durable $Na_2V_6O_{16}\cdot 1.63H_2O$ Nanowire Cathode for Aqueous Zinc-Ion Battery. *Nano Lett.* **2018**, *18* (3), 1758–1763.

(23) Hu, P.; Yan, M.; Zhu, T.; Wang, X.; Wei, X.; Li, J.; Zhou, L.; Li, Z.; Chen, L.; Mai, L. Zn/V_2O_5 Aqueous Hybrid-Ion Battery with High Voltage Platform and Long Cycle Life. *ACS Appl. Mater. Interfaces* **2017**, *9* (49), 42717–42722.

(24) Yan, J.; Wang, J.; Liu, H.; Bakenov, Z.; Gosselink, D.; Chen, P. Rechargeable Hybrid Aqueous Batteries. *J. Power Sources* **2012**, *216*, 222–226.

(25) Meng, F.; Zhong, H.; Bao, D.; Yan, J.; Zhang, X. In Situ Coupling of Strung Co_4N and Intertwined N–C Fibers toward Free-Standing Bifunctional Cathode for Robust, Efficient, and Flexible Zn–Air Batteries. *J. Am. Chem. Soc.* **2016**, *138* (32), 10226–10231.

(26) Laszczynski, S.; Michalowski, T. Von. Storage Battery. US714301A, February 23, 1901.

(27) Himy, A. *Silver-Zinc Battery : Phenomena and Design Principles*, 1st ed.; Vantage Press: New York, 1986.

(28) McBreen, J. *Power Sources for Electric Vehicles*; McNicol, B. D., Rand, D. A. J., Eds.; Elsevier: Amsterdam, 1984.

(29) McBreen, J. Rechargeable Zinc Batteries. *J. Electroanal. Chem. Interfacial Electrochem.* **1984**, *168* (1–2), 415–432.

(30) McLarnon, F. R.; Cairns, E. J. The Secondary Alkaline Zinc Electrode. *J. Electrochem. Soc.* **1991**, *138* (2), 645.

(31) McBreen, J. Nickel/Zinc Batteries. *J. Power Sources* **1994**, *51* (1–2), 37–44.

(32) Hietbrink, E. H.; Boak, R. W.; Atkins, L. P. Electric Vehicle Road Tests of Ni-Zn Batteries. *SAE Tech. Pap. Ser.* **1983**.

(33) Cairns, E. J.; McLarnon, F. R. Proceedings of the Symposium on Batteries and Fuel Cells for Stationary and ... - Google Books. In *Proceedings of the Symposium on Batteries and Fuel Cells for Stationary and Electric Vehicle Applications*; Landgrebe, A. R., Takehara, Z., Eds.; The Electrochemical Society: Honolulu, 1993; pp 1–11.

(34) Pei, P.; Wang, K.; Ma, Z. Technologies for Extending Zinc–Air Battery's Cyclelife: A Review. *Appl. Energy* **2014**, *128*, 315–324.

(35) Goldstein, J.; Brown, I.; Koretz, B. New Developments in the Electric Fuel Ltd. Zinc/Air System. *J. Power Sources* **1999**, *80* (1–2), 171–179.

(36) Hadjipaschalis, I.; Poullikkas, A.; Efthimiou, V. Overview of Current and Future Energy Storage Technologies for Electric Power Applications. *Renew. Sustain. Energy Rev.* **2009**, *13* (6–7), 1513–1522.

(37) Linden, D.; Reddy, T. B. *Handbook of Batteries*; McGraw-Hill, 2002.

(38) Lee, C. W.; Eom, S. W.; Sathiyanarayanan, K.; Yun, M. S. Preliminary Comparative Studies of Zinc and Zinc Oxide Electrodes on Corrosion Reaction and Reversible Reaction for Zinc/Air Fuel Cells. *Electrochim. Acta* **2006**, *52* (4), 1588–1591.

(39) Ross Jr, P. N. Zinc Electrode and Rechargeable Zinc-Air Battery. US4842963A, June 21, 1988.

(40) Müller, S.; Holzer, F.; Haas, O. Optimized Zinc Electrode for the Rechargeable Zinc–Air Battery. *J. Appl. Electrochem.* **1998**, *28* (9), 895–898.

(41) Baugh, L. M.; Higginson, A. Passivation of Zinc in Concentrated Alkaline Solution—I. Characteristics of Active Dissolution Prior to Passivation. *Electrochim. Acta* **1985**, *30* (9), 1163–1172.

(42) Baugh, L. M.; Baikie, A. R. Passivation of Zinc in Concentrated Alkaline Solution—II. Role of Various Experimental Factors and the Distinction between the Solid-State and Dissolution—Precipitation Mechanisms. *Electrochim. Acta* **1985**, *30* (9), 1173–1183.

(43) Lee, C. W.; Sathiyanarayanan, K.; Eom, S. W.; Yun, M. S. Novel Alloys to Improve the Electrochemical Behavior of Zinc Anodes for Zinc/Air Battery. *J. Power Sources* **2006**, *160* (2), 1436–1441.

(44) Hoang, T. K. A.; Doan, T. N. L.; Sun, K. E. K.; Chen, P. Corrosion Chemistry and Protection of Zinc & Zinc Alloys by Polymer-Containing Materials for Potential Use in Rechargeable Aqueous Batteries. *RSC Adv.* **2015**, *5*, 41677.

(45) Zhi, J.; Yazdi, A. Z.; Valappil, G.; Haime, J.; Chen, P. Artificial Solid Electrolyte Interphase for Aqueous Lithium Energy Storage Systems. *Sci. Adv.* **2017**, *3* (9), e1701010.

(46) Yuan, G.; Bai, J.; Doan, T. N. L.; Chen, P. Synthesis and Electrochemical Investigation of Nanosized LiMn2O4 as Cathode Material for Rechargeable Hybrid Aqueous Batteries. *Mater. Lett.* **2014**, *137*, 311–314.

(47) Garcia, G.; Ventosa, E.; Schuhmann, W. Complete Prevention of Dendrite Formation in Zn Metal Anodes by Means of Pulsed Charging Protocols. *ACS Appl. Mater. Interfaces* **2017**, *9* (22), 18691–18698.

(48) Li, Y.; Dai, H. Recent Advances in Zinc–Air Batteries. *Chem. Soc. Rev.* **2014**, *43* (15), 5257–5275.

(49) Hoang, T. K. A.; Doan, T. N. L.; Sun, K. E. K.; Chen, P. Corrosion Chemistry and Protection of Zinc & Zinc Alloys by Polymer-Containing Materials for Potential Use in Rechargeable Aqueous Batteries. *RSC Adv.* **2015**, *5* (52), 41677–41691.

(50) Brenner, A. *Electrodeposition of Alloys. Volume II, Practical and Specific Information : Principles and Practice*; Elsevier, 2013.

(51) Bicelli, L. P.; Bozzini, B.; Mele, C.; D ’urzo, L. A Review of Nanostructural Aspects of Metal Electrodeposition. *Int. J. Electrochem. Sci* **2008**, *3*, 356–408.

(52) Boto, K. Organic Additives in Zinc Electroplating. *Electrodepos. Surf. Treat.* **1975**, *3* (2), 77–95.

(53) Snowdon, R. C. Electrolytic Precipitation of Zinc. *J. Phys. Chem.* **1906**, *11* (5), 369–381.

(54) Kumar, S.; Pande, S.; Verma, P. Factor Effecting Electro-Deposition Process. *Int. J. Curr. Eng. Technol.* **2015**, *55* (22), 2277–4106.

(55) Wu, W.; Eliaz, N.; Gileadi, E. The Effects of PH and Temperature on Electrodeposition of Re-Ir-Ni Coatings from Aqueous Solutions. *J. Electrochem. Soc.* **2014**, *162* (1), D20–D26.

(56) Güler, E. S. Effects of Electroplating Characteristics on the Coating Properties. In *Electrodeposition of Composite Materials*; InTech, 2016.

(57) Nikolić, N. D.; Pavlović 1#, L. J.; Pavlović, M. G.; Popov, K. I. Effect of Temperature on the Electrodeposition of Disperse Copper Deposits. *J. Serb. Chem. Soc* **2007**, *72* (12), 1369–1381.

(58) Vogt, H.; Balzer, R. J. The Bubble Coverage of Gas-Evolving Electrodes in Stagnant Electrolytes. *Electrochim. Acta* **2005**, *50* (10), 2073–2079.

(59) Popov, K. I.; Maksimović, M. D.; Trnjančev, J. D.; Pavlović, M. G. Dendritic Electrocrystallization and the Mechanism of Powder Formation in the Potentiostatic Electrodeposition of Metals. *J. Appl. Electrochem.* **1981**, *11* (2), 239–246.

(60) Guo, C.; Zuo, Y.; Zhao, X.; Zhao, J.; Xiong, J. The Effects of Electrodeposition Current Density on Properties of Ni–CNTs Composite Coatings. *Surf. Coatings Technol.* **2008**, *202* (14), 3246–3250.

(61) Fazli, S.; Bahrololoom, M. E. Effect of Plating Time on Electrodeposition of Thick Nanocrystalline Permalloy Foils. *Trans. IMF* **2016**, *94* (2), 92–98.

(62) Oloruntoba, Daniel, T.; Eghwubare, O.; Oluwole, L. Effect of Some Process Variables on Nickel Electroplating of Low Carbon Steel. *Leonardo Electron. J. Pract. Technol.* **2011**, *10* (18), 79–94.

(63) Sheu, F. C.; Chen, K. S. The Effect of Temperature, Agitation and Content of Gold on the Thickness of Electroplated Gold at Various Current Densities. *J. Chinese Chem. Soc.* **1978**, *25* (1), 9–16.

(64) Engelmaier, W.; Kessler, T. Investigation of Agitation Effects on Electroplated Copper in Multilayer Board Plated-Through Holes in a Forced-Flow Plating Cell. *J. Electrochem. Soc.* **1978**, *125* (1), 36.

(65) MacInnes, D. A.; Adler, L. HYDROGEN OVERVOLTAGE. *J. Am. Chem. Soc.* **1919**, *41* (2), 194–207.

(66) Mesters, J. R. *Nucleation and Crystal Growth*; Hamburg, 2007.

(67) Hohenberg, P. C.; Halperin, B. I. Theory of Dynamic Critical Phenomena. *Rev. Mod. Phys.* **1977**, *49* (3), 435–479.

(68) Chaikin, P. M.; Lubensky, T. C. *Principles of Condensed Matter Physics*, 1st ed.; Cambridge University Press, 1995.

(69) De Yoreo, J. J.; Vekilov, P. G. Principles of Crystal Nucleation and Growth. *Rev. Mineral. Geochemistry* **2003**, *54* (1), 57–93.

(70) Paunovic, M.; Schlesinger, M.; John Wiley & Sons. *Fundamentals of Electrochemical Deposition*, 2nd ed.; Wiley, 2006.

(71) Despic, A.; Popov, K. *Modern Aspects of Electrochemistry*; White, R. E., Bockris, J. O. (John O. ., Conway, B. E., Eds.; Plenum Press, 1995.

(72) Diggle, J. W.; Despic, A. R.; Bockris, J. O. The Mechanism of the Dendritic Electrocrystallization of Zinc. *J. Electrochem. Soc.* **1969**, *116* (11), 1503.

(73) Popov, K. I.; Živković, P. M.; Nikolić, N. D. Electrochemical Aspects of Formation of Dendrites. *Zast. Mater.* **2016**, *57* (1), 55–62.

(74) Banik, S. J. SUPPRESSING DENDRITIC GROWTH DURING ZINC ELECTRODEPOSITION USING POLYETHYLENIMINE AS AN ELECTROLYTE ADDITIVE FOR RECHARGEABLE ZINC BATTERIES, Case Western University, 2016.

(75) Monroe, C.; Newman, J. Dendrite Growth in Lithium/Polymer Systems. *J. Electrochem. Soc.* **2003**, *150* (10), A1377.

(76) Aaboubi, O.; Douglade, J.; Abenaqui, X.; Boumedmed, R.; VonHoff, J. Influence of Tartaric Acid on Zinc Electrodeposition from Sulphate Bath. *Electrochim. Acta* **2011**, *56* (23), 7885–7889.

(77) Zhao, Y. P.; Yin, R. H.; Cao, W. M.; Yuan, A. B. Electropolymerization of Aniline on Zinc-Electroplated Steel from Neutral Aqueous Medium by Single-Step Process. *Acta Metall. Sin.* **2004**, *17* (6), 849–855.

(78) Hirsch, M. Surface Active Agents (Surfactants): Types and Applications https://knowledge.ulprospector.com/3106/pc-surface-active-agents-surfactants/ (accessed Jun 20, 2018).

(79) Yang, H.; Cao, Y.; Ai, X.; Xiao, L. Improved Discharge Capacity and Suppressed Surface Passivation of Zinc Anode in Dilute Alkaline Solution Using Surfactant Additives. *J. Power Sources* **2004**, *128* (1), 97–101.

(80) Kan, J.; Xue, H.; Mu, S. Effect of Inhibitors on Zn-Dendrite Formation for Zinc-Polyaniline Secondary Battery. *J. Power Sources* **1998**, *74*, 113.

(81) Natter, H.; Hempelmann, R. Nanocrystalline Copper by Pulsed Electrodeposition: The Effects of Organic Additives, Bath Temperature, and PH. *J. Phys. Chem.* **1996**, *100*, 19525–19532.

(82) Lee, J.-Y.; Kim, J.-W.; Lee, M.-K.; Shin, H.-J.; Kim, H.-T.; Park, S.-M. Effects of Organic Additives on Initial Stages of Zinc Electroplating on Iron. *J. Electrochem. Soc.* **2004**, *151* (1), C25.

(83) Akiyama, T.; Kobayashi, S.; Ki, J.; Ohgai, T.; Fukushima, H. Role of Polyethylene Glycol in Electrodeposition of Zinc–Chromium Alloys. *J. Appl. Electrochem.* **2000**, *30* (7), 817–822.

(84) Roberge, G. Online Corrosion Course https://corrosion-doctors.org/Principles/Course.htm (accessed Jun 3, 2018).

(85) Grujicic, D.; Pesic, B. Electrodeposition of Copper: The Nucleation Mechanisms. *Electrochim. Acta* **2002**, *47* (18), 2901–2912.

(86) Macdonald, D. D. Reflections on the History of Electrochemical Impedance Spectroscopy. *Electrochim. Acta* **2006**, *51* (8–9), 1376–1388.

(87) Randviir, E. P.; Banks, C. E. Electrochemical Impedance Spectroscopy: An Overview of Bioanalytical Applications. *Anal. Methods* **2013**, *5* (5), 1098.

(88) Rigaku. X-ray Diffraction.

(89) Kumar Petla, R.; Vivekanandhan, S.; Misra, M.; Kumar Mohanty, A.; Satyanarayana, N. Soybean (&Lt;I&Gt;Glycine Max&Lt;/I&Gt;) Leaf Extract Based Green Synthesis of Palladium Nanoparticles. *J. Biomater. Nanobiotechnol.* **2012**, *03* (01), 14–19.

(90) Langford, J. I.; Wilson, A. J. C.; IUCr. Scherrer after Sixty Years: A Survey and Some New Results in the Determination of Crystallite Size. *J. Appl. Crystallogr.* **1978**, *11* (2), 102–113.

(91) Birkner, N.; wang, Q. How an FTIR Spectrometer Operates - Chemistry LibreTexts https://chem.libretexts.org/Core/Physical_and_Theoretical_Chemistry/Spectroscopy/Vibrational_Spectroscopy/Infrared_Spectroscopy/How_an_FTIR_Spectrometer_Operates (accessed Jun 17, 2018).

(92) Clayborne, A.; Vernon, M. Fourier Transform Infrared Spectroscopy (FTIR) - Chemistry LibreTexts https://chem.libretexts.org/LibreTexts/Howard_University/Howard%3A_Physical_Chemistry_Laboratory/14._Fourier_Transform_Infrared_Spectroscopy_(FTIR) (accessed Jun 17, 2018).

(93) Chen, Z.; Wang, W.; Zhang, Z.; Fang, X. High-Efficiency Visible-Light-Driven Ag_3PO_4 /AgI Photocatalysts: Z-Scheme Photocatalytic Mechanism for Their Enhanced Photocatalytic Activity. *J. Phys. Chem. C* **2013**, *117* (38), 19346–19352.

(94) Australian Microscopy & Microanalysis Research Facility. Scanning Electron Microscopy in Practice http://www.ammrf.org.au/myscope/sem/practice/principles/layout.php#detail (accessed Jun 17, 2018).

(95) Atomic World. Atomic World - Transmission electron microscope (TEM) - Principle of TEM http://www.hk-phy.org/atomic_world/tem/tem02_e.html (accessed Jun 17, 2018).

(96) Jokerst, J. V; Lobovkina, T.; Zare, R. N.; Gambhir, S. S. Nanoparticle PEGylation for Imaging and Therapy. *Nanomedicine (Lond).* **2011**, *6* (4), 715–728.

(97) Strickley, R. G. Solubilizing Excipients in Oral and Injectable Formulations. *Pharm. Res.* **2004**, *21* (2), 201–230.

(98) Ballesteros, J. C.; Díaz-Arista, P.; Meas, Y.; Ortega, R.; Trejo, G. Zinc Electrodeposition in the Presence of Polyethylene Glycol 20000. *Electrochim. Acta* **2007**, *52* (11), 3686–3696.

(99) Jones, W. *Electrolytic Copper Plating Additives and Contaminants*.

(100) Koperliovich, D. Nickel electroplating http://www.substech.com/dokuwiki/doku.php?id=nickel_electroplating (accessed Jun 17, 2018).

(101) Lee, J.-S.; Tai Kim, S.; Cao, R.; Choi, N.-S.; Liu, M.; Lee, K. T.; Cho, J. Metal-Air Batteries with High Energy Density: Li-Air versus Zn-Air. *Adv. Energy Mater.* **2011**, *1* (1), 34–50.

(102) Özcan, M.; Dehri, İ.; Erbil, M. Organic Sulphur-Containing Compounds as Corrosion Inhibitors for Mild Steel in Acidic Media: Correlation between Inhibition Efficiency and Chemical Structure. *Appl. Surf. Sci.* **2004**, *236* (1–4), 155–164.

(103) Ehteshamzadeh, M.; Jafari, A. H.; Naderi, E.; Hosseini, M. G. Effect of Carbon Steel Microstructures and Molecular Structure of Two New Schiff Base Compounds on Inhibition Performance in 1 M HCl Solution by EIS. *Mater. Chem. Phys.* **2009**, *113* (2–3), 986–993.

(104) Baik, D. S.; Fray, D. J. Electrodeposition of Zinc from High Acid Zinc Chloride Solutions. *J. Appl. Electrochem.* **2001**, *31* (10), 1141–1147.

(105) Hultquist, G. Hydrogen Evolution in Corrosion of Copper in Pure Water. *Corros. Sci.* **1986**, *26* (2), 173–177.

(106) Diggle, J. W.; Despic, A. R.; Bockris, M. The Mechanism of the Dendritic Electrocrystallization of Zinc. *J. Org. Chem. N. Kharasch* **1966**, *116* (20), 1526–162.

(107) Braga, M. H.; Grundish, N. S.; Murchison, A. J.; Goodenough, J. B. Alternative Strategy for a Safe Rechargeable Battery. *Energy Environ. Sci.* **2017**, *10* (1), 331–336.

(108) Desai, D.; Wei, X.; Steingart, D. A.; Banerjee, S. Electrodeposition of Preferentially Oriented Zinc for Flow-Assisted Alkaline Batteries. *J. Power Sources* **2014**, *256*, 145–152.

(109) Grier, D.; Ben-Jacob, E.; Clarke, R.; Sander, L. M. Morphology and Microstructure in Electrochemical Deposition of Zinc. *Phys. Rev. Lett.* **1986**, *56* (12), 1264–1267.

(110) Sun, K. E. K.; Hoang, T. K. A.; Doan, T. N. L.; Yu, Y.; Zhu, X.; Tian, Y.; Chen, P. Suppression of Dendrite Formation and Corrosion on Zinc Anode of Secondary Aqueous Batteries. *ACS Appl. Mater. Interfaces* **2017**, *9* (11), 9681–9687.

(111) Stuart, B. *Infrared Spectroscopy: Fundamentals and Applications*; John Wiley & Sons, 2004.

(112) Pramanik, S.; Ataollahi, F.; Pingguan-Murphy, B.; Oshkour, A. A.; Osman, N. A. A. In Vitro Study of Surface Modified Poly(Ethylene Glycol)-Impregnated Sintered Bovine Bone Scaffolds on Human Fibroblast Cells. *Sci. Rep.* **2015**, *5* (1), 9806.

(113) Stein, S. E. *Infrared Spectra*; Linstrom, P. J., Mallard, W. G., Eds.; National Institute of Standards and Technology: Gaithersburg, 2018.

(114) Grdadolnik, J. Saturation Effects in FTIR Spectroscopy: Intensity of Amide I and Amide II Bands in Protein Spectra. *Acta Chim. Slov.* **2003**, *50* (4), 777–788.

(115) Naybour, R. D. Morphologies of Zinc Electrodeposited from Zinc-Saturated Aqueous Alkaline Solution. *Electrochim. Acta* **1968**, *13* (4), 763–769.

(116) Gomes, A.; da Silva Pereira, M. I. Pulsed Electrodeposition of Zn in the Presence of Surfactants. *Electrochim. Acta* **2006**, *51* (7), 1342–1350.

(117) Li, D. Y.; Szpunar, J. A. A Monte Carlo Simulation Approach to the Texture Formation during Electrodeposition—II. Simulation and Experiment. *Electrochim. Acta* **1997**, *42* (1), 47–60.

(118) *Powder Diffraction File Alphabetical Index, File 4-831*; International Center for Diffraction Data: Swartmore, PA, 1988.

(119) Matysina, Z. A.; Chuprina, L. M.; Zaginaichenko, S. Y. Surface Structure, Roughness, Energy and Texture of Crystals. *J. Phys. Chem. Solids* **1992**, *53* (1), 167–174.

(120) Ichino, R.; Cachet, C.; Wiart, R. Mechanism of Zinc Electrodeposition in Acidic Sulfate Electrolytes Containing Pb2+ Ions. *Electrochim. Acta* **1996**, *41* (7–8), 1031–1039.

(121) Banik, S. J. Suppressing Dendritic Growth during Zinc Electrodeposition Using Polyethylimine as an Electrolyte Additice for Rechargeable Zinc Batteries, Case Western Reserve University, 2016.

(122) Venkatakrishnan, A.; Kuppa, V. K. Polymer Adsorption on Rough Surfaces. *Curr. Opin. Chem. Eng.* **2018**, *19*, 170–177.

(123) Trejo, G.; Ruiz, H.; Borges, R. O.; Meas, Y. Influence of Polyethoxylated Additives on Zinc Electrodeposition from Acidic Solutions. *J. Appl. Electrochem.* **2001**, *31* (6), 685–692.

(124) Stoychev, D.; Tsvetanov, C. Behaviour of Poly(Ethylene Glycol) Duringelectrodeposition of Bright Copper Coatings in Sulfuric Acid Electrolytes. *J. Appl. Electrochem.* **1996**, *26*, 741–749.

(125) Manu, R.; Jayakrishnan, S. *Influence of Polymer Additive Molecular Weight on Surface and Microstructural Characteristics of Electrodeposited Copper*; 2011; Vol. 34.

(126) Nakano, H.; Oue, S.; Hamaguchi, Y.; Kobayashi, S.; Fukushima, H. Effect of Preadsorption of Polyethylene Glycol on the Appearance and Morphology of Electrogalvanized Steel Sheets. *ISIJ Int.* **2009**, *49* (11), 1769–1775.

(127) Gel | physics and chemistry | https://www.britannica.com/science/gel (accessed Jun 28, 2018).

(128) Sangeetha, N. M.; Maitra, U. Supramolecular Gels: Functions and Uses.

(129) Senthilkumar, S. T.; Selvan, R. K.; Ponpandian, N.; Melo, J. S. Redox Additive Aqueous Polymer Gel Electrolyte for an Electric Double Layer Capacitor. *RSC Adv.* **2012**, *2* (24), 8937.

(130) Sun, X.; Zhao, J. Reformation of Fumed Silica Gel After Being Broken. *Silicon* **2017**, *9*, 879–884.

(131) Choudhury, N. A.; Sampath, S.; Shukla, A. K. Hydrogel-Polymer Electrolytes for Electrochemical Capacitors: An Overview. *Energy Environ. Sci.* **2009**, *2*, 55–67.

(132) AEROSIL fumed silica for battery gels http://www.aerosil.com/product/aerosil/en/industries/batteries/battery-gels/ (accessed Jun 28, 2018).

(133) Liao, Y.; Rao, M.; Li, W.; Tan, C.; Yi, J.; Chen, L. Improvement in Ionic Conductivity of Self-Supported P(MMA-AN-VAc) Gel Electrolyte by Fumed Silica for Lithium Ion Batteries. *Electrochim. Acta* **2009**, *54*, 6396–6402.

(134) Sharma, J. P.; Sekhon, S. S. Nanodispersed Polymer Gel Electrolytes: Conductivity Modification with the Addition of PMMA and Fumed Silica. *Solid State Ionics* **2007**, *178*, 439–445.

(135) Hoang, T. K. A.; Doan, T. N. L.; Cho, J. H.; Su, J. Y. J.; Lee, C.; Lu, C.; Chen, P. Sustainable Gel Electrolyte Containing Pyrazole as Corrosion Inhibitor and Dendrite Suppressor for Aqueous Zn/$LiMn_2O_4$ Battery. *ChemSusChem* **2017**, *10* (13), 2816–2822.

(136) Zgoła-Grześkowiak, A.; Grześkowiak, T.; Zembrzuska, J.; Łukaszewski, Z. Comparison of Biodegradation of Poly(Ethylene Glycol)s and Poly(Propylene Glycol)S. *Chemosphere* **2006**, *64* (5), 803–809.

(137) Inoue, H.; Kurosaki, M.; Nohara, S. Deposition of Zinc in Polymer Hydrogel Electrolyte. In *214th ECS Meeting*; The Electrochemical Society, 2008.

(138) Bakenov, Z.; Taniguchi, I. Electrochemical Performance of Nanostructured LiMxMn2−xO4 (M = Co and Al) Powders at High Charge–Discharge Operations. *Solid State Ionics* **2005**, *176* (11–12), 1027–1034.

(139) Thackeray, M. M.; Johnson, P. J.; de Picciotto, L. A.; Bruce, P. G.; Goodenough, J. B. Electrochemical Extraction of Lithium from LiMn2O4. *Mater. Res. Bull.* **1984**, *19* (2), 179–187.

(140) Benedek, R.; Thackeray, M. M. Reaction Energy for $LiMn_2O_4$ Spinel Dissolution in Acid. *Electrochem. Solid-State Lett.* **2006**, *9* (6), A265.

Appendices

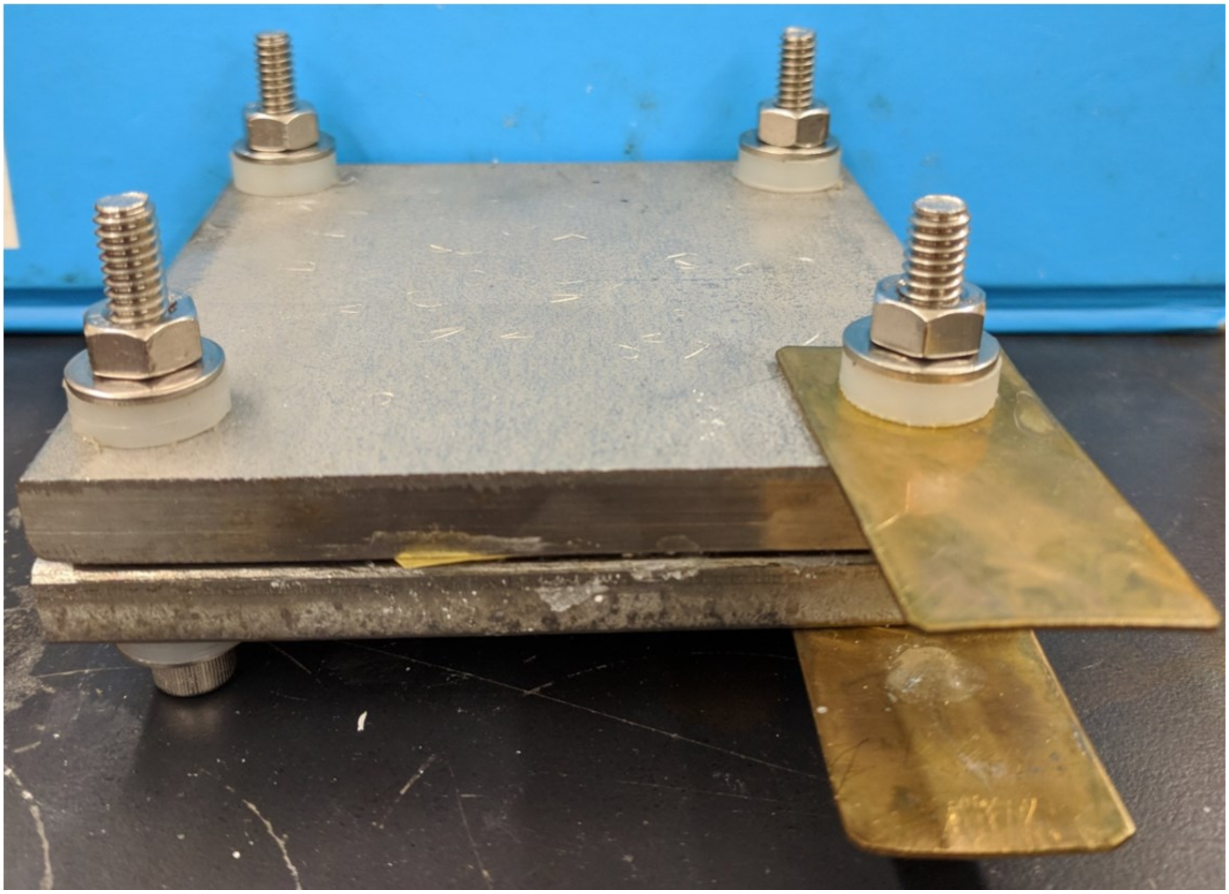

***Appendix 1**: External view of assembled large 7 mAh cell*

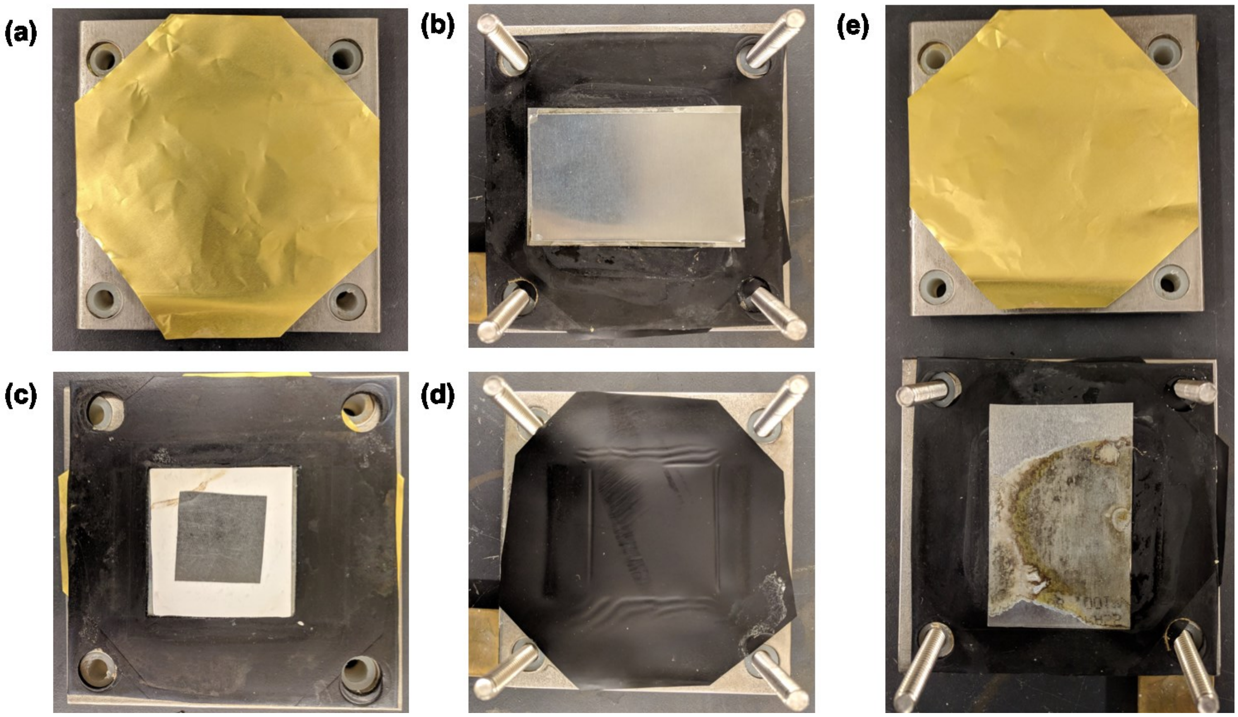

***Appendix 2**: Internal view of large cell. (a) Cell base and brass anodic current collector. Zinc anode (b) and LMO cathode (c) shown as part of assembled inner part of cell. (d) Cell top and polyethylene cathodic current collector. (e) Disassembled cell after cycle life testing.*

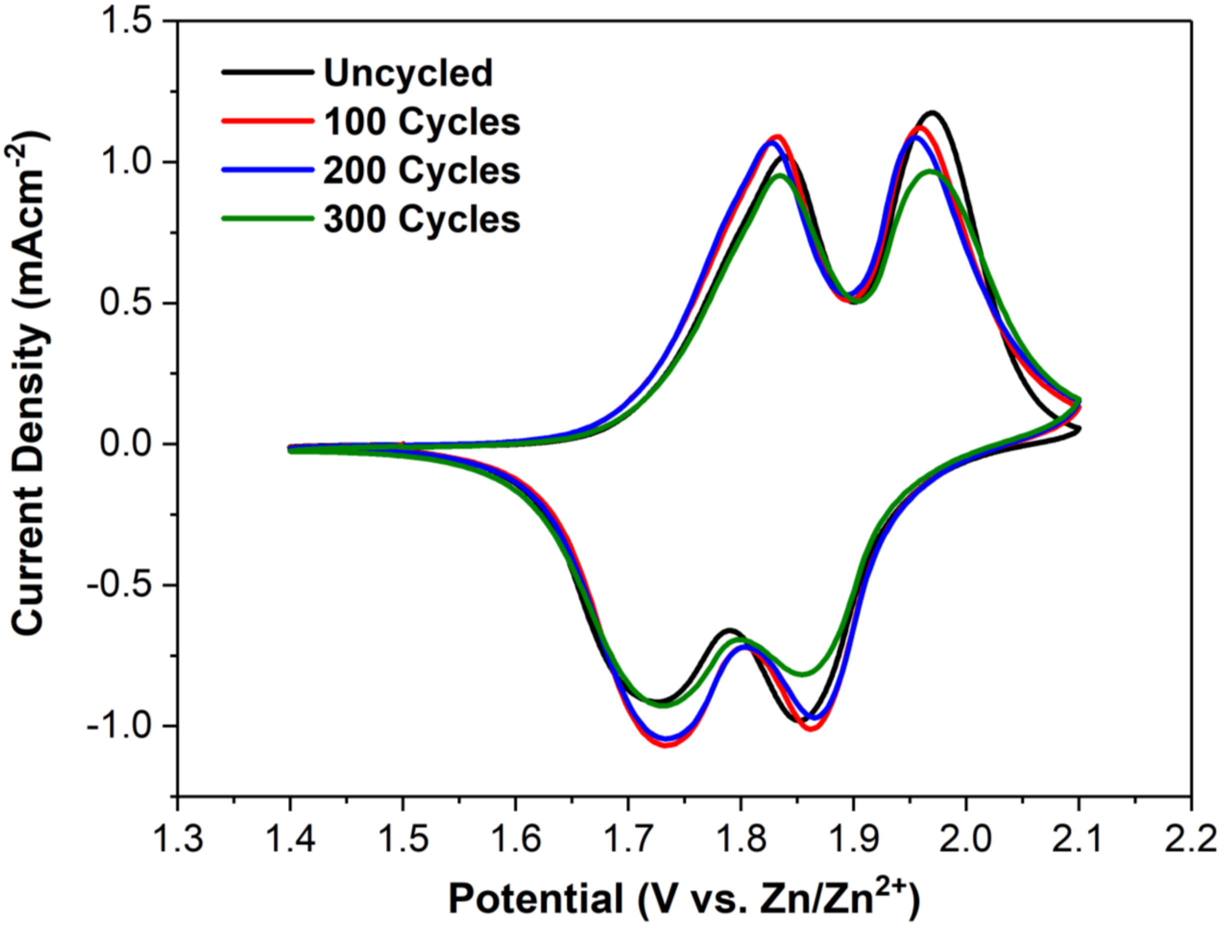

Appendix 3*: Cyclic voltammetry of small cells before cycling and after 100, 200, and 300 charge-discharge cycles at 1 C equivalent current*